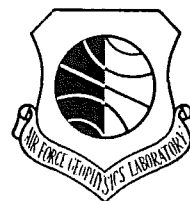


AFGL-TR-83-0002

ENVIRONMENTAL RESEARCH PAPERS, NO. 819



SCATHA Environmental Atlas

E. G. MULLEN
M. S. GUSSENHOVEN

Property of U. S. Air Force
AEDC LIBRARY
F40600-81-C-0004

3 January 1983

TECHNICAL REPORTS
FILE COPY

Approved for public release; distribution unlimited.

SPACE PHYSICS DIVISION

PROJECT 7601

AIR FORCE GEOPHYSICS LABORATORY

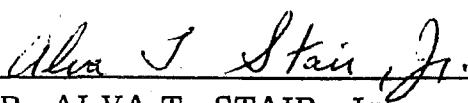
HANSCOM AFB, MASSACHUSETTS 01731

AIR FORCE SYSTEMS COMMAND, USAF



This report has been reviewed by the ESD Public Affairs Office (PA)
and is releasable to the National Technical Information Service (NTIS).

This technical report has been reviewed and
is approved for publication.


DR. ALVA T. STAIR, Jr.
Chief Scientist

Qualified requestors may obtain additional copies from the
Defense Technical Information Center. All others should apply
to the National Technical Information Service.

Unclassified

SECURITY CLASSIFICATION OF THIS PAGE (When Data Entered)

REPORT DOCUMENTATION PAGE		READ INSTRUCTIONS BEFORE COMPLETING FORM
1. REPORT NUMBER AFGL-TR-83-0002	2. GOVT ACCESSION NO.	3. RECIPIENT'S CATALOG NUMBER
4. TITLE (and Subtitle) SCATHA ENVIRONMENTAL ATLAS		5. TYPE OF REPORT & PERIOD COVERED Scientific. Final.
		6. PERFORMING ORG. REPORT NUMBER ERP No. 819
7. AUTHOR(s) E. G. Mullen M. S. Gussenhoven *		8. CONTRACT OR GRANT NUMBER(s)
9. PERFORMING ORGANIZATION NAME AND ADDRESS Air Force Geophysics Laboratory (PHG) Hanscom AFB Massachusetts 01731		10. PROGRAM ELEMENT, PROJECT, TASK AREA & WORK UNIT NUMBERS 62101F 76011205
11. CONTROLLING OFFICE NAME AND ADDRESS Air Force Geophysics Laboratory (PHG) Hanscom AFB Massachusetts 01731		12. REPORT DATE 3 January 1983
14. MONITORING AGENCY NAME & ADDRESS (if different from Controlling Office)		13. NUMBER OF PAGES 169
		15. SECURITY CLASS. (of this report) Unclassified
15a. DECLASSIFICATION/DOWNGRADING SCHEDULE		
16. DISTRIBUTION STATEMENT (of this Report) Approved for public release; distribution unlimited.		
17. DISTRIBUTION STATEMENT (of the abstract entered in Block 20, if different from Report)		
18. SUPPLEMENTARY NOTES * Physics Department, Boston College, Chestnut Hill, Massachusetts		
19. KEY WORDS (Continue on reverse side if necessary and identify by block number) Spacecraft charging Ions SCATHA Electrons Space environment Space physics Energetic particles Magnetic fields		
20. ABSTRACT (Continue on reverse side if necessary and identify by block number) A study of the plasma environment encountered by the P78-2 Spacecraft Charging At High Altitudes (SCATHA) satellite during its operation between March 1979 and June 1980 was conducted. Statistical analyses of the 100 eV to 5 MeV particle populations at near-geosynchronous altitudes were performed. The analyses ordered the electron and ion density and flux data in KP, L-shell, and local time (LT). Comparisons of measured magnetic fields with the Olson-Pfitzer magnetic field model were also made. Results of the analyses are presented in a form useful for spacecraft design engineers.		

DD FORM 1473
1 JAN 73

EDITION OF 1 NOV 65 IS OBSOLETE

Unclassified

SECURITY CLASSIFICATION OF THIS PAGE (When Data Entered)

Preface

The authors would like to thank the SCATHA experimenters: D. A. Hardy, AFGL; T. L. Aggson, NASA Goddard; B. G. Ledley, NASA Goddard; E. C. Whipple, UCSD; P. F. Mizera, Aerospace; J. F. Fennell, Aerospace; R. G. Johnson, Lockheed; J. B. Reagan, Lockheed; H. C. Koons, Aerospace, and R. C. Adamo, SRI for use of their data and the countless discussions of its interpretation. Special thanks are given to Mr. R. E. McInerney of AFGL who provided us the necessary computer resources to accomplish the task. Special thanks are also given to J. Feynman of Boston College for authoring the appendix on the 40-keV trapping region. D. E. Delorey of Boston College provided the bulk of the computer programming. J. Cronin of Boston College and D. Riehl of Regis College provided programming for special studies. J. Collins of Emmanuel College provided most of the artwork, and N. Heinemann of Boston College prepared data presentations. H. Garrett of JPL initiated the atlas and laid the foundation for the work. W. J. Burke of AFGL provided the particle trajectory code. Also, a special thanks to L. Rukin and M. Outwater of AFGL for excellent secretarial support. Special appreciation is expressed to F. A. Hanser of Panametrics, Inc. for discussions on the SC5 data; R. Nightingale of Lockheed for discussions on the SC3 data; and R. Strangeway and R. Sharp of Lockheed for discussions on the SC8 data. The work of M. S. Gussenhoven was supported by the Air Force Geophysics Laboratory under Contract F19628-82-K-0011.

Contents

1. INTRODUCTION	13
2. ATLAS DATA BASE	14
2.1 Satellite Orbit	14
2.2 Instruments	14
2.3 Data Base	15
3. THE NEAR-GEOSYNCHRONOUS PLASMA REGIME	17
3.1 The Plasmasphere	17
3.2 The Plasma Sheet	18
3.3 The Ring Current	18
3.4 The Outer Radiation Belt	19
3.5 Spectrogram Identification	19
3.6 Particle Trajectories	22
4. SC5 MIDDLE ENERGY ION AND ELECTRON RESULTS	27
4.1 Introduction	27
4.2 Instrumentation	28
4.3 Data Base	30
4.3.1 Electron and Ion Flux File	31
4.3.2 Moment Data Base	32
4.4 Data Analysis	39
4.4.1 Flux Distributions Perpendicular to the Magnetic Field	39
4.4.2 Moments	46
4.4.2.1 Number Density	48
4.4.2.2 Energy Density (ϵ)	55
4.4.2.3 Average Energy (ϵ/n)	59
4.4.2.4 Number Flux	64
4.4.3 Pitch Angle Anisotropies	69
4.5 Discussion	73

Contents

5. SC8 ION COMPOSITION RESULTS	76
5.1 Introduction	76
5.2 Instrumentation	77
5.3 Data Base	78
5.4 Data Analysis	80
5.4.1 Power Law Spectra Fitting	80
5.4.2 The $n(O^+)/n(H^+)$ ratio	84
5.4.3 Variation With KP	84
5.4.4 Variation With L-shell	87
5.4.5 Local Time Variations	90
5.4.6 Polar Plots	92
5.5 Discussion	96
6. SC11 MAGNETIC FIELD RESULTS	100
6.1 Introduction	100
6.2 Instrumentation	101
6.3 Data Base	101
6.4 Data Analysis	101
6.5 Discussion	116
7. SC3 HIGH ENERGY ELECTRON RESULTS	120
7.1 Introduction	120
7.2 Instrumentation	121
7.3 Data Base	122
7.4 Data Analysis	130
7.5 Discussion	135
8. SUMMARY	138
REFERENCES	141
APPENDIX A: SCATHA EXPERIMENTERS	145
APPENDIX B: CORRECTION OF SC5 ION DATA USING SC8 ION COMPOSITION MEASUREMENTS	147
APPENDIX C: THE 40-keV ELECTRON DURABLE TRAPPING REGION	155
APPENDIX D: HIGH-LEVEL SPACECRAFT CHARGING ENVIRONMENTS	163

Illustrations

1. Yearly Sunspot Number (R) and Yearly Magnetic Activity Index (aa) for the Period From 1870 to 1980	16
2. SC9 Spectrogram for Day 341, 1979 Illustrating a Magnetically Quiet Day When the Plasmasphere was Expanded	21

Illustrations

3. SC9 Spectrogram for Day 164, 1979 Illustrating a Day That Starts Out Magnetically Quiet and Becomes Moderately Active Postnoon in UT	22
4. SC9 Spectrogram for Day 142, 1979 Illustrating a Magnetically Disturbed Day When the Inner Edge of the Plasmasheet Moved Earthward of the Satellite Orbit	23
5. Proton Trajectories in the Equatorial Plane for a Crossed Dipolelike Magnetic Field and a Volland-Stern Convection Electric Field Characterized by $\gamma = 2$ and a Dusk Stagnation Distance of $7.2 R_E$ (KP = 3)	25
6. Electron Trajectories in the Equatorial Plane for a Crossed Dipolelike Magnetic Field and a Volland-Stern Convection Electric Field Characterized by $\gamma = 2$ and a Dusk Stagnation Distance of $7.2 R_E$ (KP = 3)	26
7. Distribution of Values of the Electron Differential Flux Measured Perpendicular to the Magnetic Field	40
8. Distribution of Values of the Ion Differential Flux Measured Perpendicular to the Magnetic Field	41
9. LT Variations of (a) Perpendicular Electron and (b) Ion Fluxes Averaged Over KP and L-shell for Selected Energy Channels	42
10. Differential Number Flux as a Function of Energy for (left) Perpendicular Electrons and (right) Ions for All KPs and L-shells for LT (x) = 0000-0100, (o) = 0600-0700, (+) = 1200-1300, and (Δ) = 1500-1600	44
11. Differential Number Flux as a Function of Energy for (left) Perpendicular Electrons and (right) Ions for All LT and L-shells for KP Ranges: (x) = 0, 1+, (o) = 2-, 3+, (+) = 4-, 5+, and (Δ) \geq 6-	45
12. SC5 Number Densities for Ions and Electrons as Determined From Spin-averaged Moments for Energy Ranges 100 eV to 400 keV and 20 to 400 keV	47
13. SC5 Number Fluxes for Ions and Electrons as Determined From Spin-averaged Moments for Energy Ranges 100 eV to 400 keV and 20 to 400 keV	48
14. SC5 Energy Densities for Ions and Electrons as Determined From Spin-averaged Moments for Energy Ranges 100 eV to 400 keV and 20 to 400 keV	49
15. SC5 Energy Fluxes for Ions and Electrons as Determined From Spin-averaged Moments for Energy Ranges 100 eV to 400 keV and 20 to 400 keV	49
16. Variations in Number Density Coded in Polar Coordinate LT and L-shell Ranges	52
17. The Average Total Electron Density vs LT From 0200 to 1600 for a KP Range From 2- to 3+ for L-shells: (x) = 6 to $7 R_E$ and + = 7 to $8 R_E$	54
18. Contours of Constant Total Energy Density (ϵ_I and ϵ_E) in Polar Coordinate L-shell and LT Plots for KP: (a) KP = 0, 1; (b) KP = 2, 3; and (c) KP = 4, 5	58

Illustrations

19. Scatter Plots of Energy Density vs Number Density for (a) High-energy Ions, (b) High-energy Electrons, (c) Low-energy Ions, and (d) Low-energy Electrons	61
20. Variations in Average Energy Coded in Polar Coordinate LT and L-shell Ranges	62
21. Scatter Plots of (a) Low-energy and (b) High-energy Electron Number Flux vs Total Electron Number Flux	67
22. Scatter Plot of Total Ion Number Flux vs Total Electron Number Flux	68
23. Anisotropy Indices Averaged Over All KP and Plotted in Polar Coordinate Representations of LT and L-shell for (a) 9-keV Electrons, (b) 96-keV Electrons, (c) 10-keV Ions, and (d) 126-keV Ions	74
24. Hourly Averages of SC8 O^+ (+) and H^+ (x) Differential Energy Fluxes for the 24 SC8 Energy Channels on Day 42, 1979	79
25. Percentage of SC8 Hourly Average Data Base Points as a Function of (a) L-shell, (b) KP, and (c) LT	82
26. SC8 Average Energy (E_{AVE}) vs the Spectral Index (α) for the SC8 Energy Range 0.1 to 32 keV	82
27. Average Energy Spectra for H^+ (x) and O^+ (+) With Their Positive Standard Deviations for SC8 Data Points for the Ranges $KP \geq 2-$ and $\leq 3+$, L-shell 6 to 7 R_E and LT 2100 to 2400	83
28. Distribution of the Oxygen to Hydrogen Density Ratios for the SC8 Data Set in Percent of Time the Density Bin Averages Fall Within 0.5 Increments	84
29. Average Oxygen to Hydrogen Number Density Ratios vs KP for L-shell Ranges (x) 5 to 6 R_E , (o) 6 to 7 R_E , (+) 7 to 8 R_E , and (Δ) 8 to 8.5 R_E	86
30. Average Oxygen (Left) and Hydrogen (Right) Number Densities vs KP for L-shell Ranges (x) 5 to 6 R_E , (o) 6 to 7 R_E , (+) 7 to 8 R_E , and (Δ) 8 to 8.5 R_E	87
31. Twenty-four Hour Average Oxygen to Hydrogen Number Density Ratio, (a); Oxygen Number Density, (b); and Hydrogen Number Density, (c) vs L-shell for KP Levels (x) 0, 1, (o) 2, 3, (+) 4, 5, and (Δ) $\geq 6-$	88
32. 2100 to 0600 LT Averaged Oxygen to Hydrogen Number Density Ratio, (a); Oxygen Number Density, (b); and Hydrogen Number Density, (c) vs L-shell for KP Levels (x) 0, 1, (o) 2, 3, (+) 4, 5, and (Δ) $\geq 6-$	89
33. Oxygen (x) and Hydrogen (+) Density Variations as a Function of LT for Four KP Ranges for the L-shell Range of 6 to 7 R_E	91
34. Oxygen (x) and Hydrogen (+) Density Variations as a Function of LT for Four KP Ranges Over the L-shell Range of 5 to 8 R_E	92
35. Average Hydrogen Differential Energy Fluxes for All 24 SC8 Channels vs LT for the KP Range $\geq 2-$ and $\leq 3+$	93

Illustrations

36. Average Hydrogen Differential Energy Fluxes for All 24 SC8 Channels vs LT for the KP Range $\geq 4-$ and $\leq 5+$	94
37. Average Oxygen Differential Energy Fluxes for All 24 SC8 Channels vs LT for the KP Range $\geq 2-$ and $\leq 3+$	95
38. Average Oxygen Differential Energy Fluxes for All 24 SC8 Channels vs LT for the KP Range $\geq 4-$ and $\leq 5+$	96
39. SC8 Hydrogen (Top), Oxygen (Middle), and O^+/H^+ (Bottom) Coded Densities in Polar Coordinate LT - L-shell Formats for KP Levels 0, 1 (Left), 2, 3 (Left Center), 4, 5 (Right Center) and $\geq 6-$ (Right)	98
40. Magnetic Field Intensities in Gammas as Measured on (Solid Line) and Modeled for (Dashed Line) the SCATHA Satellite on a Magnetically Quiet Day, Day 156, 1979	103
41. Magnetic Field Intensities in Gammas as Measured on (Solid Line) and Modeled for (Dashed Line) the SCATHA Satellite on a Magnetically Quiet Day, Day 212, 1979	104
42. Magnetic Field Intensities in Gammas as Measured on (Solid Line) and Modeled for (Dashed Line) the SCATHA Satellite on a Magnetically Quiet Day, Day 309, 1979	105
43. Magnetic Field Intensities in Gammas as Measured on (Solid Line) and Modeled for (Dashed Line) the SCATHA Satellite on a Magnetically Quiet Day, Day 36, 1980	106
44. Magnetic Field Intensities in Gammas as Measured on (Solid Line) and Modeled for (Dashed Line) the SCATHA Satellite on a Magnetically Disturbed Day, Day 115, 1979	108
45. Magnetic Field Intensities in Gammas as Measured on (Solid Line) and Modeled for (Dashed Line) the SCATHA Satellite on a Magnetically Disturbed Day, Day 241, 1979	109
46. Magnetic Field Intensities in Gammas as Measured on (Solid Line) and Modeled for (Dashed Line) the SCATHA Satellite on a Moderately Active Day, Day 172, 1979	113
47. Average Magnetic Field Energy Densities Between 0900 - 1500 LT vs L-shell for KP Ranges (x) 0 to 1+, (o) 2- to 3+, and (+) 4- to 5+	114
48. Average Magnetic Field Energy Densities Between 2100 - 0300 LT vs L-shell for KP Ranges (x) 0 to 1+, (o) 2- to 3+, and (+) 4- to 5+	115
49. Average Plasma β vs LT for KP Ranges (x) 0 to 1+, (o) 2- to 3+, and (+) 4- to 5+	117
50. Average Plasma β vs L-shell for KP Ranges (x) 0 to 1+, (o) 2- to 3+, (+) 4- to 5+ in the (a) Noon and (b) Midnight Sectors	118
51. Scatter Plot of β vs L-shell for Periods KP was $\geq 4-$ and $\leq 5+$ Between 1800 to 0600 LT	120
52. High-energy Electron Fluxes vs UT for Day 94, 1979 (an Example of a Day With Low Flux Levels)	124
53. High-energy Electron Fluxes vs UT for Day 149, 1979; an Example of a Day With High Flux Levels	125

Illustrations

54. Scatter Plot of the Log of the 634 to 1026 keV Flux Values vs L-shell for the SC3 Data Set	130
55. Scatter Plot of the Log of the 1026 to 1419 keV Flux Values vs L-shell for the SC3 Data Set	131
56. Scatter Plot of the Log of the 1419 to 2603 keV Flux Values vs L-shell for the SC3 Data Set	132
57. Scatter Plot of the Log of the 2603 to 4970 keV Flux Values vs L-shell for the SC3 Data Set	134
58. Power Law Fits of Average SC3 Electron Fluxes at L-shells From 5.75 to 7.75 R_E	134
59. SC3 High-energy Electron Flux Cumulative Distributions for 0.5 L-shell Ranges for Energies 634 to 1026 keV	135
60. SC3 High-energy Electron Flux Cumulative Distributions for 0.5 L-shell Ranges for Energies 1026 to 1419 keV	136
61. SC3 High-energy Electron Flux Cumulative Distributions for 0.5 L-shell Ranges for Energies 1419 to 2603 keV	137
B1. Three-hour LT Averages of the Corrected SC5 Low-energy (0.05 - 20 keV) Ion Density vs the Sum of the SC8 O^+ Plus H^+ Densities	153
B2. Polar Plots of Ion Number Densities in LT and L-shell for KP Levels ≥ 2 - and $\leq 3+$: (a) SC5 Ion Densities Assuming 100 Percent H^+ , (b) SC5 Ion Densities Corrected by SC8 O^+/H^+ Density Ratios, and (c) SC8 Total Ion Density	154
C1. Examples of Dropouts in the SC5 Electron and Ion Particle Counts	157
C2. Positions of Dropouts of 40-keV Electron Fluxes in Radial Distance, R_E (Top Plot), Solar Magnetic Latitude (Middle Plot), and Geocentric Solar Magnetospheric Latitude (Bottom Plot) vs LT for Periods Between Day 75, 1979 and Day 74, 1980 When the KP Level was $\leq 4+$	158
C3. Positions of Dropouts of 40-keV Electron Fluxes in Radial Distance, R_E (Top Plot), Solar Magnetic Latitude (Middle Plot), and Geocentric Solar Magnetospheric Latitude (Bottom Plot) vs LT for Periods Between Day 75, 1979 and Day 74, 1980 When the KP Level was $\geq 5-$	159
C4. The Top Plot Shows the LT of Dropouts in Composite Coordinate Latitude During Magnetic Storm Periods When KP $\geq 6-$. The bottom plot shows the same dropouts as a function of radial distance and composite coordinate latitude	160
D1a. Distribution Functions of Ions and Electrons Measured Perpendicular to the Magnetic Field Prior to Charging (Dashed Line) and During the Peak Charging Levels (Solid Lines) on Day 114, 1979	165
D1b. Distribution Functions of Ions and Electrons Measured Perpendicular to the Magnetic Field Prior to Charging (Dashed Line) and During the Peak Charging Levels (Solid Lines) on Day 241, 1979	166

Illustrations

D1c. Distribution Functions of Ions and Electrons Measured
Perpendicular to the Magnetic Field Prior to Charging
(Dashed Line) and During the Peak Charging Levels (Solid
Lines) on Day 363, 1979

167

Tables

1. Moment Input Velocities and Energies	29
2. SC5 Data Base Days	30
3. Parallel Detector Factors	31
4. Perpendicular Detector Factors	32
5. SC5 Moment Data Set	35
6. 100 eV to 400 keV Electron Densities (cm^{-3}) for KP Levels 2, 3 (4, 5)	55
7. 100 eV to 400 keV Uncorrected Ion Densities (cm^{-3}) for KP Levels 2, 3 (4, 5)	55
8. Percentage Energy Density for KP Levels 2, 3 (4, 5)	56
9. Percentage High-energy Ion Energy Density for KP Levels 2, 3 (4, 5)	56
10. Total Energy Density ($\epsilon_I + \epsilon_E$) keV/cm^3 , for KP Levels 2, 3 (4, 5)	57
11. Electron High-energy Average Energy (keV) for KP Levels 2, 3 (4, 5)	63
12. Ion High-energy Average Energy (keV) for KP Levels 2, 3 (4, 5)	63
13. Electron Low-energy Average Energy (keV) for KP Levels 2, 3 (4, 5)	64
14. Ion Low-energy Average Energy (keV) for KP Levels 2, 3 (4, 5)	64
15. Total Electron Number Flux ($\times 10^9$) ($\text{cm}^2 \text{sec}^{-1}$) for KP Levels 2, 3 (4, 5)	65
16. Percentage High-energy Electron Number Flux of Total Electron Number Flux for KP Levels 2, 3 (4, 5)	65
17. Percentage High-energy Ion Number Flux of Total Electron Number Flux for KP Levels 2, 3 (4, 5)	66
18. Percentage Low-energy Ion Number Flux of Total Electron Number Flux for KP Levels 2, 3 (4, 5)	66
19. Electron Anisotropy Indices (All KP)	70
20. Ion Anisotropy Indices (All KP)	71

Tables

21. Electron Anisotropy Indices ($L = 6 - 8$)	72
22. Ion Anisotropy Indices ($L = 6 - 8$)	73
23. Population Percentages of Total Electron Number Flux for Three High-level Charging Days	76
24. SC8 Ion Detector Characteristics	78
25. Days From 1979 in SC8 Data Base	80
26. Average $n(O^+)/n(H^+)$ Ratios and (Number of Points)	85
27. SC11 Data Base Days	102
28. Magnetic Field Model - Measured B_x Averages	110
29. Magnetic Field Model - Measured B_y Averages	111
30. Magnetic Field Model - Measured B_z Averages	112
31. SC3 ELEC2 Mode Characteristics	122
32. SC3 Data Base Days	123
33. SC3 634 to 1026 keV Data Set	126
34. SC3 1026 to 1419 keV Data Set	127
35. SC3 1419 to 2603 keV Data Set	128
36. SC3 2603 to 4970 keV Data Set	129
37. Average High-energy Electron Fluxes	131
38. SC3 Average Energy Spectra Coefficients	133
B1. Unsmoothed Correction Factors (δ)	151
B2. Modified Correction Factors (δ)	152
D1. SCATHA Time and Position for "Worst Case" Charging Events	164

SCATHA Environmental Atlas

1. INTRODUCTION

The P78-2 Spacecraft Charging AT High Altitudes (SCATHA) satellite was launched into a near-geosynchronous, equatorial orbit in January 1979. The purpose of the satellite was to provide a comprehensive means to study the effects of spacecraft charging on satellite systems. As a result, SCATHA was instrumented with a number of engineering and geophysical sensors to study both the environment and its interaction with space systems (see Stevens and Vampola).¹ One of the products of the SCATHA satellite was to be an atlas of the near-geosynchronous plasma environment that could be used as a reference document in defining test standards for future DOD geosynchronous space vehicles. This is that document. It contains the results of ongoing data analysis studies since launch in 1979 that provide the environmental information necessary to properly design and test space systems, and provide the scientific community with experimental data in a format in which it can be used to test scientific theories critical to future space missions.

This atlas does not contain copies of all the data used in arriving at the results, since the amount of data itself would fill several volumes. Instead, only

(Received for publication 27 December 1982)

1. Stevens, J.R., and Vampola, A.L., Eds. (1978) Description of the Space Test Program P78-2 Spacecraft and Payloads, SAMSO TR-78-24, 59 pp.

representative samples of the various data sets will be presented to make specific points. Lists of the days used for particular data sets in the atlas will be presented in each individual section. If data for a specific instrument are required, the requester should contact the individual principal investigator listed in Appendix A. Thus, any constraints on the data can be discussed directly with the person most knowledgeable. The results in the atlas are mostly statistical. Some case studies will be discussed, but the reader is referred to individual reports in the reference list for further information.

The atlas will be divided into three basic parts. The first part will review the satellite orbit parameters, identify the instruments used for the data base, outline the overall data base, discuss its selection criteria, and tell how it relates to average long-term variations in solar and magnetic parameters. A general discussion on the near-geosynchronous plasma regime will also be given. The second part will contain sections on results of statistical studies from each individual instrument. Each section will contain introduction, instrumentation, data base, analysis, and discussion subsections. The last part will present a short summary of results felt to be most significant. Several appendices are attached which, among other things, give results of studies relating to spacecraft charging.

2. ATLAS DATA BASE

2.1 Satellite Orbit

The P78-2 SCATHA satellite was launched on 30 January 1979 from Cape Canaveral Air Force Station, Florida. Seventy-two hours after launch the satellite was inserted into a $5.3 R_E \times 7.8 R_E$ ($R_E = 1$ Earth radius), low inclination (7.9°) orbit with an eastwardly drift rate of about 5° per day. The satellite is spin stabilized at approximately 1 rpm with the spin axis of the satellite located in the orbital plane of the satellite and normal to the Earth-sun line. Because of the drift and eccentricity of the orbit, the satellite passes through each altitude at varying LTs and varying magnetic latitudes. This presents some problems in unfolding time, magnetic activity, and spatial statistical dependencies for a limited data set, which will be discussed in the next section.

2.2 Instruments

The instruments used for statistical analyses in the atlas (exclusive of the appendices) were SC5 for 100-eV to 400-keV ions and electrons, SC3 for 600-keV to 5-MeV electrons, SC8 for 100 eV to 32-keV H^+ and O^+ ions and SC11 for the

magnetic field. In addition, SC2 and SC9 spectrograms are used to display and gain insight to various phenomena, such as plasma sheet crossings, injection events, etc., which are discussed throughout the atlas. The spectrogram is a well-documented technique² for observing spacecraft charging and related particle phenomena. The remaining instruments discussed in the atlas relate directly to measurements of charging effects and are confined to the appendices. Of the two instruments placed on SCATHA specifically to measure the low-energy plasma environment, one failed during checkout and the other failed approximately two weeks after turn on. As a result, no studies on the low-energy ($<100\text{eV}$) plasma are included here. No SC10 measurements of large-scale convection electric fields will be included because of the authors' inability to distinguish changes in the data due to the electric field from changes caused by photoelectron sheath effects.

2.3 Data Base

For numerous reasons the final atlas data base consists of an experiment — dependent varying numbers of days of data and actual data points. First, the data base for each instrument depends on operational conditions. Every instrument has times when it is turned off for reasons such as active beam experiments, to retard sensor degradation, prior to boom deployment, etc. Most instruments can operate in several modes not all of which are conducive to statistical studies. Second, the data base for each instrument depends on data rate. Some instruments sample very fast and provide large data sets. Other instruments sample very slowly to get meaningful integrated values above background noise levels. Different instruments were, of necessity, assigned different telemetry data rates to stay within the capacity of the satellite. Third, some data could be reduced (put into engineering units) at AFGL and other data had to be reduced at contractor facilities within available resources. All these constraints led to somewhat diverse data sets for the various experiments. Therefore, in addition to an overall discussion here, each data set will be fully identified and discussed in its own section.

The original plan was to have 75 complete days of data from each instrument over the first year of operation. The days were selected to cover "key event" days (periods or intervals of special interest), to provide even distribution throughout the year (to get LT distribution with altitude), to get a full range of magnetic activity conditions (KP and Dst) for each altitude regime and LT interval, and to get a large number of eclipse days to observe the plasma in the absence of

2. DeForest, S. E. (1972) Spacecraft charging at synchronous orbit, J. Geophys. Res. 77:651.

satellite photoelectrons. In the end, for some instruments data were used for periods available more than for periods desired.

The final data base includes data from day 42, 1979 through day 166, 1980. This period is compared to other periods over the last few solar cycles. Figure 1 shows the yearly mean sunspot number (R) in the upper panel and the yearly mean geomagnetic activity index (aa) in the lower panel, over the period from 1870 to 1980. The sunspot numbers in 1979 and 1980 are at the peak of a solar cycle, which itself is very high. However, the geomagnetic activity level is low for the same period; in fact, it has the lowest level during the last solar cycle. In conclusion, the data base was gathered over a period near the maximum of a high solar cycle, for a low average magnetic activity level, in the absence of any super magnetic storms.

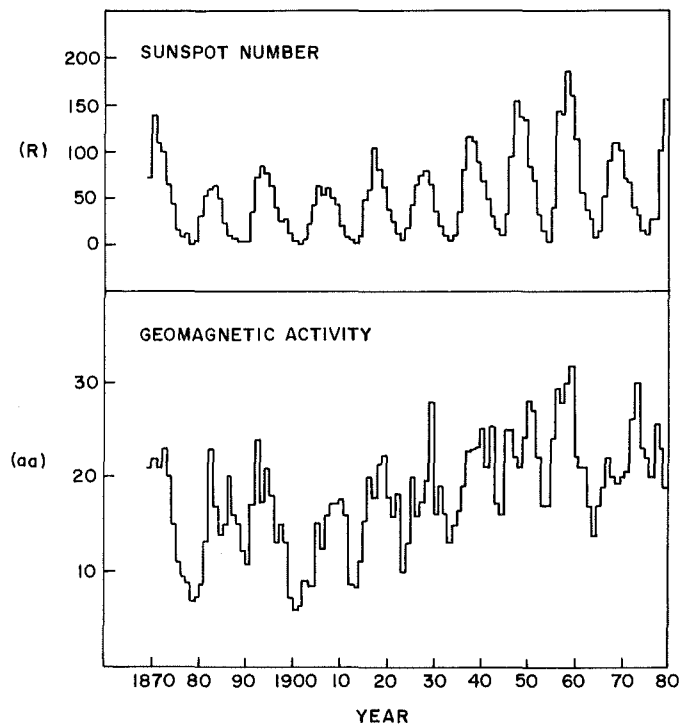


Figure 1. Yearly Sunspot Number (R) and Yearly Magnetic Activity Index (aa) for the Period From 1870 to 1980

3. THE NEAR-GEOSYNCHRONOUS PLASMA REGIME

The magnetosphere at altitudes between 27500 and 43200 km (SCATHA perigee and apogee) in the equatorial plane is extremely complex. Between these altitudes a satellite can encounter plasmasphere, plasma sheet, plasma trough, tail lobe, outer radiation belt, ring current and even, on occasion, solar wind particle populations. Some of the regions are well-defined and have distinguishable boundaries. Others have particle populations that overlap, making identification difficult. Further complicating the picture are the dynamic properties of this area of space. Particle source and loss mechanisms and regions are not completely understood, although much has been learned over the last ten years from satellite measurements. Event phenomena such as injection events (rapid earthward movements of plasma-sheet particles in the midnight sector during increased levels of geomagnetic activity) cause many of the regions to change size, shape, and composition. Here we will give an overview of the major near-geosynchronous plasma populations we expect to see in the SCATHA data.

3.1 The Plasmasphere

The plasmasphere is a region of cold ($\sim 1\text{-}30$ eV), dense ($> 10\text{ cm}^{-3}$) plasma surrounding the earth at mid and low latitudes. This volume of plasma has an asymmetric toroidal shape with the bulge generally in the evening sector. The plasmasphere can extend out to distances ranging beyond geosynchronous altitude, but only for periods of very low geomagnetic activity and then primarily in the bulge region, postnoon, and premidnight. This region of space is populated by particles that move upward from the ionosphere. During periods of high magnetic activity the plasmasphere recedes inward well within the geosynchronous altitude. The outer edge of the plasmasphere, called the plasmopause, is characterized by a steep gradient in low energy plasma density. Here the plasma density can drop by over three orders of magnitude within ~ 1000 km in the equatorial plane. The plasmopause is limited by the last closed equipotential surface of the magnetospheric convection electric field, beyond which cold plasma from the ionosphere can escape the magnetosphere. Since the SCATHA instruments to measure the cold plasma characteristic of this region of space malfunctioned shortly after turn on, no analysis of this plasma population ≤ 50 eV was performed. A review of the plasmaspheric measurements can be found in Chappell³ and ATS 6 measurements of the low energy plasma at synchronous orbit in Lennartsson and Reasoner.⁴

3. Chappell, C.R. (1972) Recent satellite measurements of the morphology and dynamics of the plasmasphere, Rev. Geophys. Space Phys. 10:951.
4. Lennartsson, W., and Reasoner, D.L. (1978) Low-energy plasma observations at synchronous orbit, J. Geophys. Res. 83:2145.

3.2 The Plasma Sheet

The plasma sheet lies beyond the plasmapause and is most clearly identifiable on the nightside, where it extends down tail to several tens of R_E . The plasma sheet is a region in which particle densities are typically 1 to 2 cm^{-3} . Except in sporadic events the cold (0 to 100 eV) particle density in this region is low and often much less than 1 cm^{-3} . The average energy of the > 100 eV ions and electrons is of the order of a few keV. Thus, although the density in the plasma sheet is low, the energy density and ambient currents are not. Ions found in the plasma sheet suggest the composition is both solar wind and ionospheric in origin, although the source mechanisms are not yet fully explainable. The plasma sheet expands and contracts with solar and magnetic activity. During high activity periods the Earthward edge of the plasma sheet in the equatorial plane can extend inward to less than 5.5 R_E , while during prolonged magnetically quiet periods (periods of low KP) the inward edge can lie beyond 10 R_E . Observationally, the inner edge of the plasma sheet is determined by a decrease in electron flux between 100 eV and a few keV. At geosynchronous altitudes the plasma sheet is most often seen near local midnight, but it can be seen from ~ 12 h around local midnight to not at all, depending on magnetic conditions. The inner edge of the plasma sheet maps to the equatorward boundary of the auroral oval at low altitudes. Within the plasma sheet rapid Earthward movements of energetic particles, called injection events, are observed. Particle injections first appear in the midnight sector in conjunction with geomagnetic substorms and relate directly to intense high-latitude auroral activity. Because the inner boundary of the plasma sheet is so dynamic, there are times when the outer boundary of the plasmasphere and the inner boundary of the plasma sheet are identical in certain local time sectors. At other times they are widely separated in the evening to midnight sector by a region called the plasma trough. Much of the understanding of the physics of the near-Earth plasma sheet is the result of numerous case studies. An extensive bibliography of work in this region has recently been prepared by Schulz.⁵

3.3 The Ring Current

The ring current is composed primarily of hot trapped ions with energies ~ 10 to 100 keV and lies mostly earthward of the inner edge of the plasma sheet. Schulz⁶ suggests that the outer boundary does not have a unique location but is a function of particle energy, charge, equatorial pitch angle, and LT. Although a

5. Schulz, M. (1980) Energetic particle populations and cosmic-ray entry, J. Geomag. Geoelec. 32:507.

6. Schulz, M. (1982) Earth's radiation belts, Rev. Geophys. Space Phys. 20:613.

significant portion of the ions that compose the ring current population up to ~ 30 keV/charge can be ionospheric in origin, the composition of particles above ~ 30 keV/charge, which provide a major contribution to the ring current, has not yet been measured. Although ions are the major source of the ring current, electrons can contribute significantly to the total current. Frank⁷ puts the near-Earth termination of the proton ring current ~ 0.5 to $1 R_E$ inside the plasmapause.

The ring current flows in a westward direction. A partial ring current can also exist in the midnight region near geosynchronous altitudes. It is diverted into the ionosphere in the premidnight sector, and return current is provided from the ionosphere in the postmidnight sector to complete the circuit. Although ring current ions are important in understanding the dynamics of the near-geosynchronous region, another trapped population, namely the high-energy electron population in the outer radiation belt, is of greater concern to satellite design engineers.

3.4 The Outer Radiation Belt

The outer radiation belt consists of high-energy particles trapped on magnetic field lines and mirroring between conjugate points north and south of the magnetic equator. Radiation belt particles are normally considered to have energies greater than 100 keV. The particles drift in a complicated manner encircling the earth in periods of tens of minutes. The radiation belt particles typically do not extend beyond $7 R_E$ due to the distortion of the magnetic field beyond that altitude. Beyond $7 R_E$ there is a quasitrapping zone where particles can complete only part of a drift orbit before escaping out the dayside magnetopause.

The trapped particle population peaks in density within an L-shell of 5, and therefore only the negative gradient of the distribution is measured at near-geosynchronous altitudes. The behavior of radiation belt particles is dynamic. Their density can vary by orders of magnitude about the mean value for a given energy, species, and altitude. Although empirical models of the outer radiation belt do exist, they are average models and do not take into consideration the dynamic behavior of the belt, especially near the equator.

3.5 Spectrogram Identification

Particle spectrograms that show counts (flux) of particles as a grey scale level on a coordinate plot of energy vs time can be used to identify particle populations and boundary crossings near geosynchronous altitude. In addition,

7. Frank, L. A. (1971) Relationship of the plasma sheet, ring current, trapping boundary, and plasma pause near the magnetic equator and local midnight, J. Geophys. Res. 76:2265.

spectrograms can be used to identify large dynamic events, such as injection events, and satellite interactions with the environment, such as spacecraft charging. Examples of some of the regions identifiable on spectrograms are given here.

Figure 2 shows an SC9 spectrogram for day 341, 1979. The y-axis of the spectrogram gives electron energy (top) and ion energy (bottom) in units of eV. The scale is logarithmic with the electron energy increasing with y and the ion energy decreasing with y. The x-axis of the spectrogram is in universal time running from 0000 to 2400 UT. Also listed below the UT values are the distance from the center of the Earth in R_E (Earth radius), LT, and magnetic latitude of the satellite. Day 341 is a magnetically quiet day with the 3-h KP levels at 1+, 1, 1-, 1, 1-, 1-, 2-, and 1+ for the 24-h period starting at 0000 UT. Between ~0200 and ~0830 UT the satellite is in the plasmasphere. Because of a lack of low energy (< 10 eV) particle measurements, it is not really evident in the spectrogram exactly where the satellite enters and leaves the plasmasphere. However, near 0830 UT, while moving out beyond $5.7 R_E$, the satellite leaves the plasmasphere and enters into the dayside plasma trough region that can be seen as a gradual increase in warm (< 1 keV) electrons. The satellite stays within this region until shortly after 2300 UT, at which time it reenters the plasmasphere. The inner plasma-sheet boundary is beyond the satellite orbit for this day.

Figure 3 shows an SC9 spectrogram for day 164, 1979, which starts as a magnetically quiet day and then becomes moderately active. The 3-h KP indices for the day are 1+, 1, 0+, 1+, 3-, 3, 2+, and 3-. Here again the satellite is in the plasmasphere between ~0100 and 0600 UT and then moves into the plasma trough region. However, at ~1400 UT when magnetic activity increases, the satellite enters the plasma sheet either due to the outward motion of the satellite, or the inward motion of the plasma sheet accompanying the injection of hotter (> 1 keV) electrons. This region, which is characterized by higher densities of > 1-keV electrons, continues through the end of the day. An injection of > 10-keV electrons near 2200 UT produces approximately 50 V of spacecraft frame charging as can be seen by the ion charging peak at this time. (See DeForest² for an explanation of charging phenomena and its appearance on spectrograms.)

Day 142, 1979 in Figure 4 is representative of magnetically active conditions. For this day the 3-h KP levels are 4+, 4-, 4, 5-, 3+, 5, 5+, and 5. Because of the high level of activity the plasma sheet has moved way in to less than $6 R_E$, and the only time the satellite is not in the plasma sheet is between approximately 1100 and 1615 UT. From ~1100 to ~1430 UT the satellite appears to be in a plasma trough region and between ~1430 and ~1615 UT the satellite is most

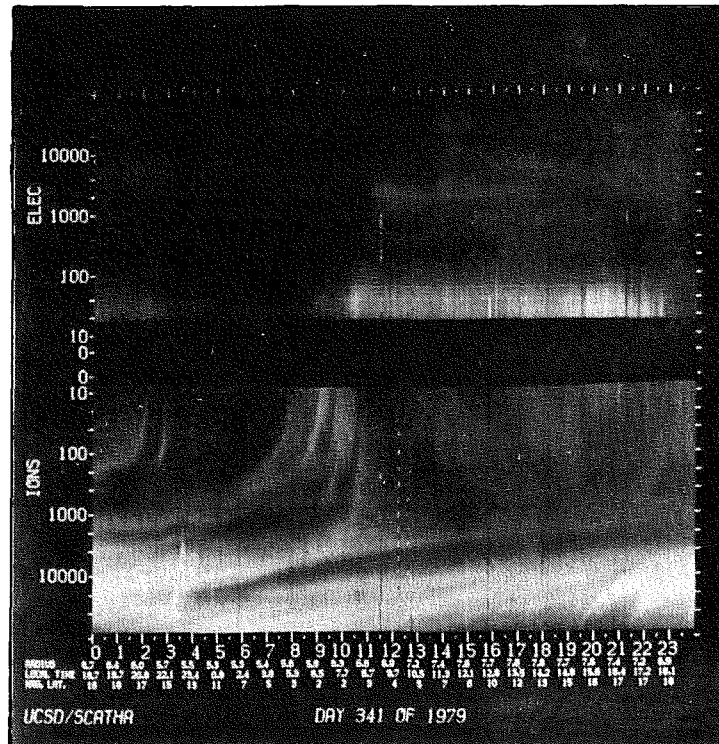


Figure 2. SC9 Spectrogram for Day 341, 1979 Illustrating a Magnetically Quiet Day When the Plasmasphere was Expanded

likely in the plasmasphere. The plasmopause and the inner plasma sheet boundary appear to be nearly coincidental at ~ 1615 UT. The activity level is so high that no plasma trough region exists in the night sector.

Another important feature in Figure 4 is the intense fluxes of warm (~ 10 to 500 eV) ions trapped near and having peak intensities at the magnetic equator. These ions were first reported by Olsen⁸ using SCATHA SC9 spectrograms. The particles are accompanied by electric field noise in the frequency range from 2 to 200 Hz (Aggson).⁹ Electric field rms filter data from the SC10 experiment were used to identify the noise. The more intense trapped ion fluxes produce noise below 20 Hz while less intense trapped ion fluxes only produce noise between 20 and 200 Hz. Aggson suggests that a ring of trapped ions (and noise) are always present near the magnetic equator but often inside the SCATHA orbit. Quinn and

8. Olsen, R.C. (1981) Equatorially trapped plasma populations, J. Geophys. Res. 86:11235.

9. Aggson, T. (1980) Private communication.

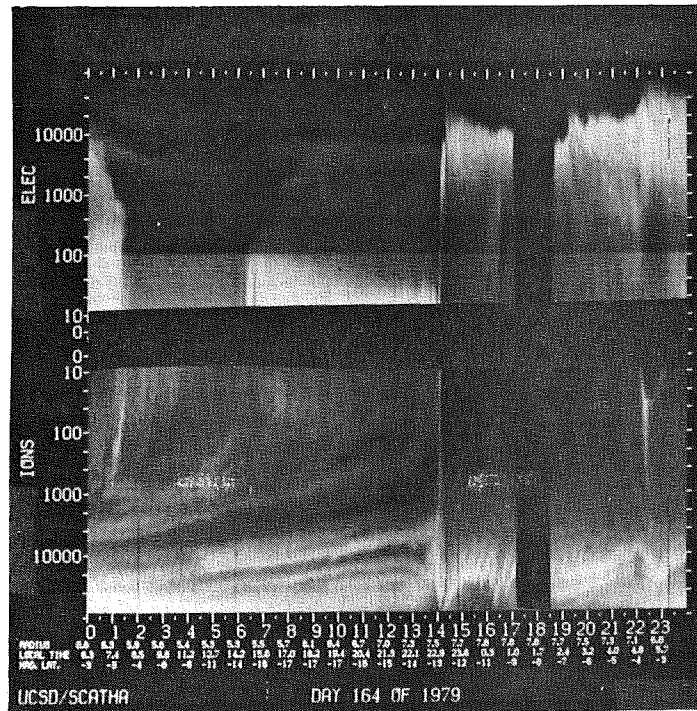


Figure 3. SC9 Spectrogram for Day 164, 1979 Illustrating a Day That Starts Out Magnetically Quiet and Becomes Moderately Active Postnoon in UT

Johnson¹⁰ studied this population above 100 eV using the SCATHA SC7 ion composition data and concluded that the dominant ion of this trapped population was H^+ .

3.6 Particle Trajectories

Much of the understanding of particle regimes in the magnetosphere results from the knowledge of individual particle motions in mutually perpendicular electric and magnetic fields. (See, for instance, Ejiri¹¹ and references therein.) Here we present sample trajectories of particles that pass through the midnight SCATHA regime to be used as a baseline from which to interpret certain atlas

10. Quinn, J. M., and Johnson, R. G. (1982) Composition measurements of warm equatorially trapped ions near geosynchronous orbit, Geophys. Res. Lett. 9:777-780.

11. Ejiri, M. (1978) Trajectory traces of charged particles in the magnetosphere, J. Geophys. Res. 83:4798.

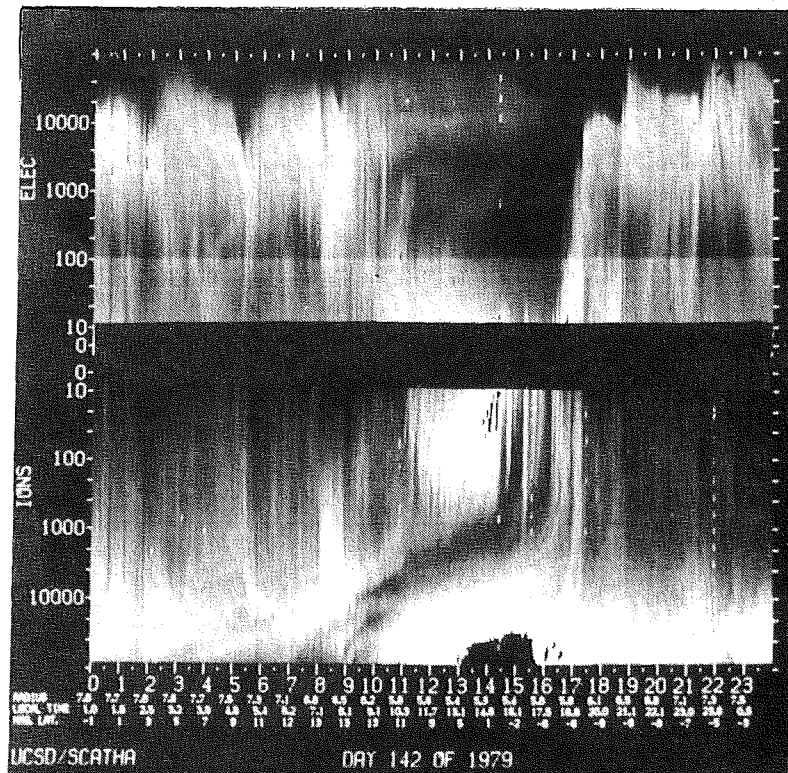


Figure 4. SC9 Spectrogram for Day 142, 1979 Illustrating a Magnetically Disturbed Day When the Inner Edge of the Plasmasheet Moved Earthward of the Satellite Orbit

results. For the magnetic field we use the simple analytic model of McIlwain,¹² which is a distorted dipole compressed near noon and inflated near midnight. The convection electric field model developed independently by Volland¹³ and Stern¹⁴ is used. It consists of two parts, a corotation field that falls off with distance as $1/R^2$, and a cross-tail field that is positive from dawn to dusk and increases with R as $R^{\gamma-1}$, where γ is generally taken to be between 1 and 3. For the calculations presented here γ is set equal to 2. To specify the electric field the stagnation distance is required. This is the distance on the dusk axis where the corotation

12. McIlwain, C. E. (1972) Plasma convection in the vicinity of the geosynchronous orbit, in Earth's Magnetospheric Processes, B.M. McCormac, Ed., D. Reidel, Hingham, Mass., p. 268.
13. Volland, H. A. (1973) A semiempirical model of large-scale magnetospheric electric fields, J. Geophys. Res. 78:171.
14. Stern, D. P. (1975) The motion of a proton in the equatorial magnetosphere, J. Geophys. Res. 80:595.

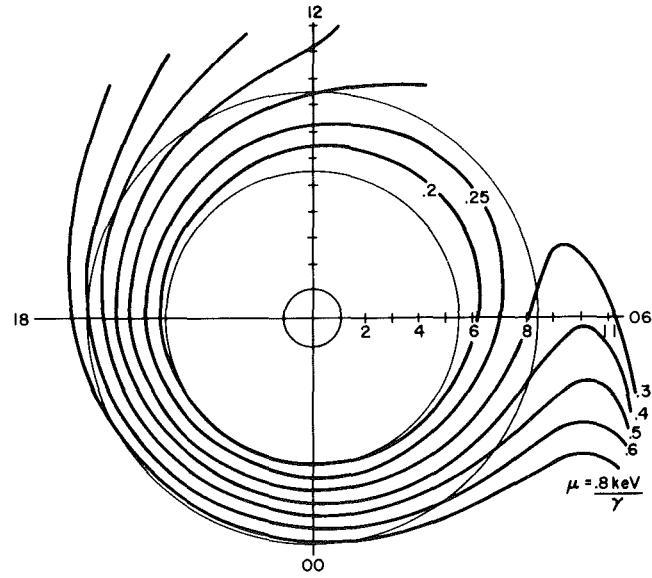
field is equal and opposite to the cross-tail field. We use a stagnation distance of $7.2 R_E$, which corresponds to moderately active conditions, that is, $KP = 3$.

In considering the motion of energetic particles we limit ourselves to particles mirroring at the equator, that is, with 90° magnetic pitch angles. In the particle motion both the total energy and the magnetic moment are conserved. Since the kinetic energy of the particle changes throughout the orbit, we label orbits by the particle's magnetic moment. We are interested in how particles move from the distant tail through the SCATHA (near-geosynchronous) regime and out of the magnetosphere when they are not subject to loss. For this purpose the particle trajectories are started at midnight within the annulus from 5.5 to $8.5 R_E$, which represents the SCATHA sampling region. They are traced backward and forward in time. We follow ions (Figure 5) and electrons (Figure 6) that have energies of 3 keV (low energy) and 30 keV (high energy) at midnight.

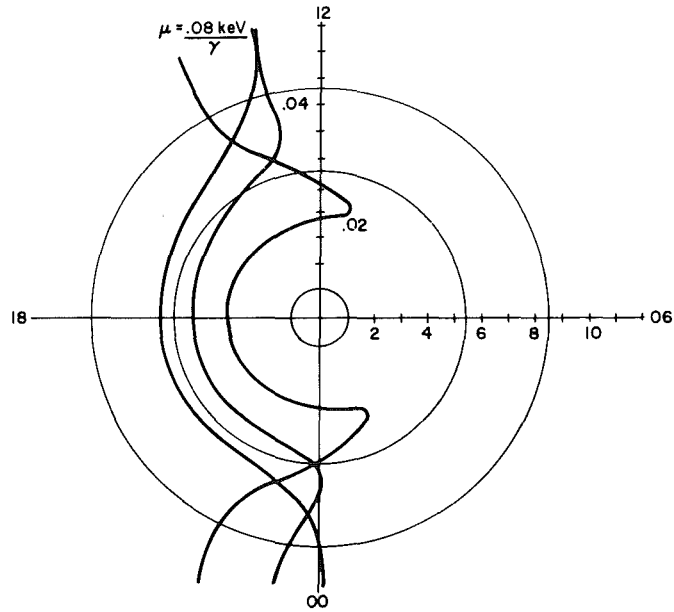
Figures 5(a) and 6(a) show the high-energy ions and electrons. The inner orbits are trapped orbits, and particles found here must come from outside by a means other than a stationary electromagnetic configuration, such as diffusion, time dependent processes, etc. In the outer annulus at midnight the particles have open orbits by which ions (electrons) from the dawn (dusk) flank of the magnetosphere have direct access to the geosynchronous region.

Figures 5(b) and 6(b) show the low-energy ions and electrons (3 keV at midnight). All orbits that pass through midnight are open. There is, however, a major distinction between the orbits of the two species. The electrons that flow into the annulus from the tail region stay on circular- (or tear-drop-) shaped orbits that keep them within (or close to) the annulus for most of the orbit. Thus, they are subject to detection by SCATHA at nearly all LT. (There is also a region of limited access in the dusk sector). Ions that pass through the midnight region with 3-keV energy, for the most part, move out of the annulus toward Earth. As they approach dayside they pass through the SCATHA regime again, this time in the noon sector. Thus, there will be a large LT region of limited access in the sampling annulus for these particles.

The particle trajectories shown here, if taken to represent the geosynchronous particle population, are extremely oversimplified. Continuous loss processes, continuous and sporadic injection processes, time-dependent electric and magnetic fields, and large-scale collective effects are integral to a realistic model. However, the trajectories form a skeleton for understanding some of the statistical results that follow.

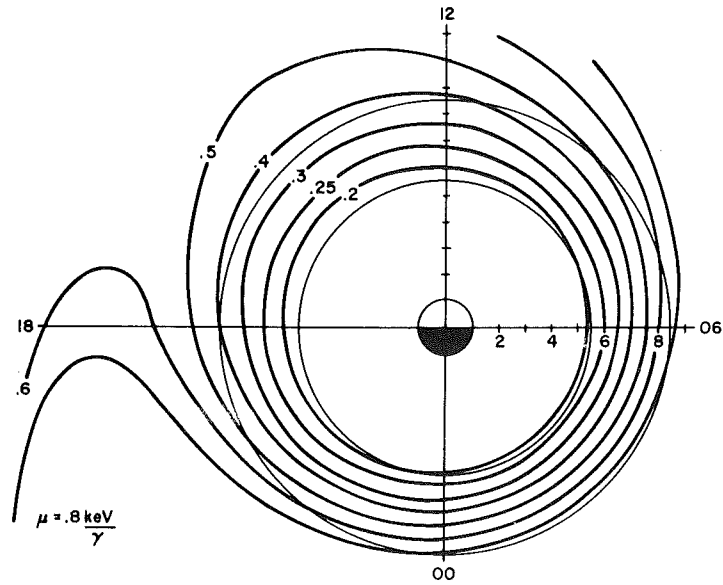


a. 30 keV PROTONS ($K_p=3$, $\gamma=2$)

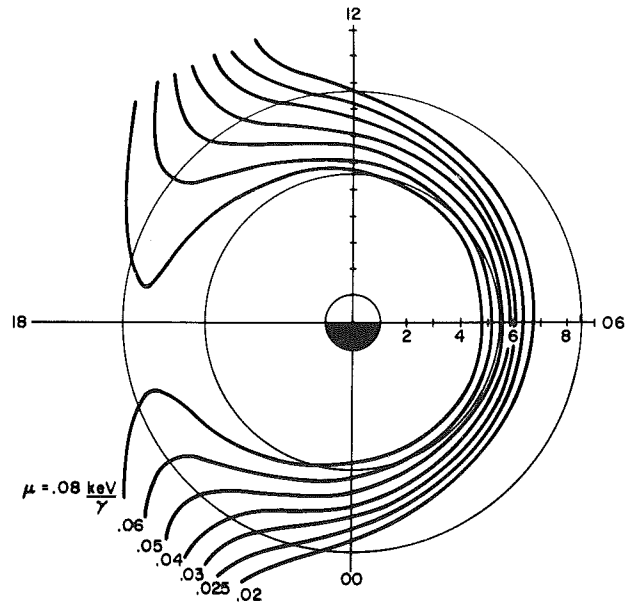


b. 3 keV PROTONS ($K_p=3$, $\gamma=2$)

Figure 5. Proton Trajectories in the Equatorial Plane for a Crossed Dipolelike Magnetic Field and a Volland-Stern Convection Electric Field Characterized by $\gamma = 2$ and a Dusk Stagnation Distance of $7.2 R_E$ ($K_p = 3$). In (a) 30-keV protons are started in the SCATHA sampling regime (5.5 to $8.5 R_E$) at midnight and traced backwards and forwards in time. In (b) 3-keV protons are started in the same regime at midnight. The trajectories are labeled by the particle magnetic moment



a. 30 keV ELECTRONS ($K_p=3$, $\gamma=2$)



b. 3 keV ELECTRONS ($K_p=3$, $\gamma=2$)

Figure 6. Electron Trajectories in the Equatorial Plane for a Crossed Dipolelike Magnetic Field and a Volland-Stern Convection Electric Field Characterized by $\gamma = 2$ and a Dusk Stagnation Distance of $7.2 R_E$ ($K_p = 3$). In (a) 30-keV electrons are started in the SCATHA sampling regime (5.5 to $8.5 R_E$) at midnight and traced backwards and forwards in time. In (b) 3-keV electrons are started in the same regime at midnight. The trajectories are labeled by the particle magnetic moment

4. SC5 MIDDLE ENERGY ION AND ELECTRON RESULTS

The middle-energy particle detectors known as SC5 on the SCATHA satellite were built and operated under the direction of Dr. D. A. Hardy of AFGL. The electron and ion measurements between 100 eV and 400 keV will be discussed in this section.

4.1 Introduction

Spacecraft charging is the mechanism by which current balance to a spacecraft is achieved. A spacecraft both intercepts current from the ambient environment and emits current from its surface materials. For spacecraft in the near-geosynchronous environment, the middle-energy particle populations contribute a significant portion of the current that is responsible for high-level surface charging. In satellite eclipse the middle-energy electrons can create vehicle charging in excess of 10 keV. Because the middle-energy particles play a major role in spacecraft surface charging (the mission study objective of the SCATHA satellite program) a major portion of the atlas will be used to discuss the SC5 results.

It should be noted however that the middle-energy particle populations do not constitute the entire plasma population in the plasma sheet, or even the entire population of interest to spacecraft charging studies. Below the middle-energy range there are cold and warm populations with energies of a few eV and tens of eV, respectively. At geosynchronous altitudes these cold and warm populations can have significantly high densities, which when accelerated by a charged spacecraft, can contribute large currents to the vehicle. Above the middle-energy range are the relativistic particles. The densities for these particles are typically far less than those in the middle-energy range. However, their high energies allow them to penetrate the satellite surface and interact with components and systems within the vehicle, thus affecting performance and satellite lifetime. The high-energy electrons will be discussed later in Section 7.

An extensive study of the SC5 particle data has been undertaken, results of which are given in the following subsection. The study is primarily statistical but attempts to give sufficient samples of critical plasma parameters to be useful to both engineers and scientists for design, modeling, and theory verification. In addition to the results, details of the instrument, data base, and analysis techniques will be discussed.

4.2 Instrumentation

The SC5 Rapid Scan Particle Detector measures the fluxes of electrons and ions in the energy ranges from 50 eV to ~ 1 MeV and from 50 eV to ~ 7 MeV, respectively. The instrument consists of two sets of detectors. One set is mounted with the look direction oriented parallel to the spin axis, and the other set perpendicular to the spin axis. Each set of detectors consists of two cylindrical plate electrostatic analyzers (ESAs) with SPIRALTRON electron multipliers (SEMs) and two silicon surface barrier solid-state detector telescopes.

The two low- (high-) energy ESAs measure the electron and ion fluxes in four contiguous channels that range from 50 eV to 1.7 keV (1.7 to 60 keV). Both sets of ESAs also measure a background channel with 0 V on the deflection plate. The low-energy ESAs have geometric factors of $\sim 1 \times 10^{-4} \text{ cm}^2 \text{ sr}$ for both ions and electrons. The high-energy ESAs have geometric factors of $3 \times 10^{-5} \text{ cm}^2 \text{ sr}$ for electrons and $3 \times 10^{-4} \text{ cm}^2 \text{ sr}$ for ions. The central energies and energy widths for the ESAs are given in Table 1. The low- and high-energy electron ESAs have full width at half maximum (FWHM) opening angles of 7° by 5° and 3° by 4° , respectively. The 5° and 4° dimensions are in the spin plane for the detectors perpendicular to the spin axis. For both the high- and low-energy ion ESAs the FWHM opening angles are 3° by 12° . The 12° dimension is in the spin plane for the detectors perpendicular to the spin axis.

The solid-state spectrometers (SSSs) make both anticoincident and coincident measurements. Here we use only the anticoincidence channels that measure particles between ~ 70 and 500 keV. The electron SSSs use a 0.1-mil aluminum foil to absorb light and protons below ~ 250 keV, and have a $300\text{-}\mu$ thick front detector. The proton SSSs use a sweeping magnet to eliminate electrons below about 200 keV and have an $\sim 6\text{-}\mu$ thick front detector with 120 mg/cm^2 of aluminum for a light shield. The front detectors in anticoincidence with the rear detectors measure the particle fluxes over the energies to be studied. The FWHM opening angle for the SSSs is approximately 20° square. The large opening angle is necessary to get significant count rates for the highest energy channels. The solid-state detectors have geometric factors of $3.6 \times 10^{-3} \text{ cm}^2 \text{ sr}$ for electrons and ions, respectively. The energy widths for the SSSs are given in Table 1.

Data from both the SSSs and the ESAs are taken simultaneously in one channel of each detector with a dwell time of 200 msec. Since each measurement takes 0.2 sec and each individual detector makes a total of five measurements, a complete energy spectrum is measured for both ions and electrons in a 1-sec interval. Since the detectors return a complete spectrum once per second and the SCATHA rotation rate is ~ 1 rpm, there is about 6° of rotation per spectrum. Thus, for ESA electron measurements there is no overlap in pitch angle in successive

Table 1. Moment Input Velocities and Energies

Ions					Electrons				
Channel	v (km/sec)	Δv (km/sec)	E (keV)	ΔE (keV)	Channel	v (km/sec)	Δv (km/sec)	E (keV)	ΔE (keV)
LE ESA 1	170	60	0.148	0.102	LE ESA 1	6250	2400	0.110	0.070
LE ESA 2	260	100	0.340	0.240	LE ESA 2	9600	3400	0.260	0.180
LE ESA 3	400	150	0.840	0.525	LE ESA 3	16000	5000	0.620	0.370
LE ESA 4	590	210	1.8	1.16	LE ESA 4	24000	10000	1.57	1.13
HE ESA 1	880	320	4.0	2.7	HE ESA 1	40000	14000	4.4	2.7
HE ESA 2	1370	580	9.7	7.5	HE ESA 2	55000	23000	9.2	7.1
HE ESA 3	2110	860	23.0	16.7	HE ESA 3	87000	30000	24.0	15.2
HE ESA 4	3260	1200	55.0	39.5	HE ESA 4	124000	46000	54.0	43.2
COINC 0	4815	1452	126.0	70.0	COINC 2	157000	42295	96.0	78.0
COINC 1	6018	1210	188.0	75.0	COINC 3	239000	37400	335.0	117.0
COINC 2	7289	1331	275.0	100.0	COINC 4	201650	33897	218.0	115.0
COINC 3	8653	1400	388.0	125.0					

spectra. However, for the ion ESA measurements and all the SSS measurements, there is significant overlap. This overlap results in a smoothing of pitch angle variations. A full description of the instrument and its calibration can be found in Hanser et al.¹⁵

4.3 Data Base

The SC5 Atlas data base is comprised of measurements of the 100-eV to 500-keV electrons and ions for 118 days from the period between day 59, 1979 and day 166, 1980. The days that were used to construct the data base are listed in Table 2. The data base was created in several parts. The two major components are (a) the electron and ion flux file and (b) the moment data base. Each of these will be discussed in detail.

Table 2. SC5 Data Base Days

YR	Day	YR	Day	YR	Day	YR	Day
1979	59	1979	125	1979	210	1979	319
	77		126		212		323
	80		127		216		328
	81		128		218		329
	87		129		225		331
	88		138		226		341
	89		141		227		348
	90		142		230		351
	91		144		232		357
	93		145		233		359
	94		146		234		361
	95		149		241		363
	103		150		248	1980	4
	104		152		254		12
	108		156		261		18
	110		157		262		27
	111		158		264		28
	112		160		271		36
	113		164		272		37
	114		166		273		42
	115		167		278		46
	116		172		279		47
	117		178		280		161
	118		180		281		162
	119		188		282		163
	120		194		293		164
	121		200		301		165
	122		206		309		166
	123		207		311		
	124		208		317		

15. Hanser, F.A., Hardy, D.A., and Sellers, B. (1979) Calibration of the Rapid Scan Particle Detector Mounted in the SCATHA Satellite, AFGL-TR-79-0167, AD A082382.

4.3.1 ELECTRON AND ION FLUX FILE

The electron and ion flux file was created from measurements of the detectors mounted parallel to the spin axis of the vehicle. The file consists of one spin (~ 57 sec) averaged fluxes for each of the ion and electron channels between 100 eV and 400 keV. High-level charging periods in eclipse and SC4 beam operations were edited from this and all SC5 data files to remove high count measurements due to particle accelerations during vehicle charging. This removed some valuable data from the data set, but the alternative of correcting each individual spectra for charging was time and manpower prohibitive. Counts from each detector channel, i , were first converted to differential number flux, $J(E_i)$, by the formula:

$$J(E_i) = C_i \times K_i \times D \quad (1)$$

where C_i is the counts for channel i (corrected for background counts in the low-energy ESA channels), K_i is a multiplicative constant containing the geometric factor and calibration constant, and D is the degradation factor calculated from in-flight calibrations for each day. Table 3 gives the channels, central energy levels, and multiplicative constants for the detector parallel to the spin axis.

Table 3. Parallel Detector Factors

Electrons			Ions		
Channel	E (keV)	Multiplicative Constant K	Channel	E (keV)	Multiplicative Constant K
LE ESA 0	0.0	0.0	LE ESA 0	0.0	0.0
HE ESA 0	0.0	0.0	HE ESA 0	0.0	0.0
LE ESA 1	0.112	588	LE ESA 1	0.145	208
2	0.271	179	2	0.353	116
3	0.679	64.9	3	0.782	36.2
4	1.50	30.3	4	1.706	13.5
HE ESA 1	4.57	34.2	HE ESA 1	4.5	5.62
2	8.97	20.8	2	10.4	2.0
3	23.2	9.26	3	25.0	8.62×10^{-1}
4	52.7	6.02	4	59.9	3.65×10^{-1}
COINC 2	96.0	3.47×10^{-2}	COINC 0	126.0	1.52×10^{-2}
3	335.0	3.28×10^{-2}	1	188.0	9.96×10^{-3}
4	218.0	1.48×10^{-2}	2	275.0	7.47×10^{-3}
			3	388.0	5.98×10^{-3}

Averages of the fluxes over the spin period of the vehicle were computed for all channels. The spin was defined as starting at a minimum magnetic pitch angle and stopping at the next minimum. With the exception of the low-energy ESA channels, a straight averaging of the number of values was performed. For the low-energy ESA channels, points were first deleted for which the flux was less than or equal to zero.

4.3.2 MOMENT DATA BASE

Unlike the moments generated in the preliminary atlas from the parallel detector (see Mullen et al),¹⁶ the moments for the final atlas were generated from the perpendicular detector in order that spin integrations over magnetic pitch angle could be performed. The perpendicular detector was mounted perpendicular to the spin axis so it measured data over nearly all pitch angles once per spin. The perpendicular detector central energies and multiplicative constants are given in Table 4.

Table 4. Perpendicular Detector Factors

Electrons			Ions		
Channel	E (keV)	Multiplicative Constant K	Channel	E (keV)	Multiplicative Constant K
LE ESA 1	0.110	714	LE ESA 1	0.148	360
2	0.260	185	2	0.340	192
3	0.620	106	3	0.840	56.2
4	1.57	32.9	4	1.8	19.2
HE ESA 1	4.4	47.2	HE ESA 1	4.0	5.88
2	9.2	23.8	2	9.7	2.17
3	24.0	11.6	3	23.0	1.00
4	54.0	7.04	4	55.0	0.431
COINC 2	96.0	3.47×10^{-2}	COINC 0	126.0	1.52×10^{-2}
3	335.0	3.28×10^{-3}	1	188.0	9.96×10^{-3}
4	218.0	1.48×10^{-2}	2	275.0	7.47×10^{-3}
			3	388.0	5.98×10^{-3}

16. Mullen, E.G., Garrett, H.B., Hardy, D.A., and Whipple, E.C. (1980)
P78-2 SCATHA Preliminary Data Atlas, AFGL-TR-80-0241, AD A094122.

For each complete spectrum (1-sec interval) the differential number flux, $J(E_i)$, was computed in the same manner as for the parallel detector Eq. (1). A simple conversion,

$$f_i = \frac{m^2}{2E_i} J(E_i) , \quad (2)$$

was used to obtain the corresponding value for the distribution function at E_i . Each spectra was assigned a central pitch angle, α .

The moment integrals,

$$M_n = \int f v^n d^3v , \quad (3)$$

(n an integer) are approximated by summations in velocity space, v , assuming symmetry in the distribution function in the plane perpendicular to the magnetic field. The summation formulas are as follows:

$$M_0 = \left[2 \sum_{j=1}^m \sum_{i=1}^n f_j(v_i) v_i^2 \Delta v_i \Delta \Psi_j \right] \times 10^{-15} = \text{number density} \quad (\text{particles/cm}^3) , \quad (4)$$

$$M_1 = \left[2 \sum_{j=1}^m \sum_{i=1}^n f_j(v_i) v_i^3 \Delta v_i \Delta \Psi_j \right] \times 10^{-10} = \text{number flux} \quad (\text{particles/cm}^2 \text{sec}) , \quad (5)$$

$$M_2 = \left[a \sum_{j=1}^m \sum_{i=1}^n f_j(v_i) v_i^4 \Delta v_i \Delta \Psi_j \right] \times 10^{-17} = \text{energy density} \quad (\text{eV/cm}^3) , \quad (6)$$

$$M_3 = \left[a \sum_{j=1}^m \sum_{i=1}^n f_j(v_i) v_i^5 \Delta v_i \Delta \Psi_j \right] \times 10^{-12} = \text{energy flux} \quad (\text{eV/cm}^2 \text{sec}) . \quad (7)$$

The multiplicative parameter a is 1.04 for electrons and 5.68×10^{-4} for ions. In the summations the subscript i refers to energy channel and the subscript j refers to the spectrum number within the spin. All integrations begin at the start of a spin and end with the last frame of a spin.

The variation with pitch angle, $\Delta\Psi_j$, is defined in terms of α_j , the central pitch angle for the j^{th} spectra within the spin (only half steps are taken for the first and last spectrum):

$$\Delta\Psi_j = \frac{\alpha_{j+1} - \alpha_{j-1}}{2} . \quad (8)$$

Spectra occurring with a sun angle of less than 40° were deleted and interpolated for. A linear interpolation on $f(v)$ as a function of time was used to replace the deleted spectra. In particular, for each energy (velocity), the data pair $[\Psi_j, f_j(v_j)]$ immediately preceding the deletion and the data pair immediately following the deletion were used as the basis for the interpolation. An interpolated spectrum was provided for each deleted spectrum. The interpolated spectra were used in the integrations. Table 1 gives the values of v , Δv , E , and ΔE used in the moment calculations.

The moments were generated over two energy ranges. The total moments (as they will be referred to throughout the atlas) used data over the entire range from ~ 100 eV to 400 keV listed in Table 4. And, the high moments only used data for channels at or above the HESA 3 channel, ~ 20 to 400 keV. A third set of moments, the low moments, were then produced simply by subtracting the high moments from the total moments. This resulted in three sets of moments that could be used for analysis.

All the moments were averaged over L-shell ranges, KP ranges, and LT intervals. They were averaged in two separate ways; first by varying the range of one parameter while using all values of the other two, and second by what we call "binning"; that is, averaging within certain ranges for all three parameters at the same time. The bin sizes used for the SC5 studies were:

LT : 1 h

L-shell : $0.5 R_E$

KP four ranges: 0 to 1+; 2- to 3+; 4- to 5+; and $\geq 6-$.

Table 5(a through d) gives the number of data points (individual moment values) for each bin for the SC5 data set. The total number of points is ~ 95000 . The number of data points for L-shells $8 R_E$ and above and below $5.5 R_E$ are biased in LT. Also the total number of data points for $KP \geq 6-$ is very low. These biases are noted to avoid misinterpretation of the statistical studies to follow.

Other SC5 data sets were constructed for special studies. Since these data sets are derived from the data sets already discussed, they can be explained quite easily and will be discussed when used in the analyses that follow.

Table 5(a). SC5 Moment Data Set

KP 0,1	L-shell (R_E)								
LT	5.0 - 5.5	5.5 - 6.0	6.0 - 6.5	6.5 - 7.0	7.0 - 7.5	7.5 - 8.0	8.0 - 8.5	8.5 - 9.0	Total
00-01	0.0	340	53	16	58	148	227	0.0	842
01-02	0.0	283	132	37	33	144	255	22	906
02-03	0.0	255	248	60	5	78	247	61	954
03-04	0.0	198	219	154	61	120	187	158	1097
04-05	0.0	255	156	264	225	239	147	38	1324
05-06	0.0	295	109	317	283	246	169	0.0	1419
06-07	0.0	236	186	277	243	321	43	0.0	1306
07-08	0.0	259	317	95	285	340	0.0	0.0	1296
08-09	10	327	344	122	285	247	0.0	0.0	1335
09-10	78	307	186	259	170	172	0.0	0.0	1172
10-11	167	199	27	303	204	79	0.0	0.0	979
11-12	213	77	37	214	547	118	0.0	0.0	1206
12-13	145	70	61	50	889	0.0	0.0	0.0	1215
13-14	77	146	0.0	78	811	29	0.0	0.0	1141
14-15	100	161	22	274	365	91	0.0	0.0	1013
15-16	14	254	152	270	315	159	0.0	0.0	1164
16-17	32	236	260	131	273	344	0.0	0.0	1276
17-18	0.0	206	305	217	203	408	0.0	0.0	1339
18-19	0.0	218	112	270	392	210	0.0	0.0	1202
19-20	0.0	245	155	278	374	117	38	0.0	1207
20-21	0.0	218	201	280	341	130	167	0.0	1337
21-22	0.0	183	249	332	182	245	187	32	1410
22-23	0.0	127	138	250	191	139	245	34	1124
23-24	0.0	227	131	90	104	79	339	0.0	970
Total	836	5322	3800	4638	6839	4203	2251	345	28234

Table 5(b). SC5 Moment Data Set

KP 2, 3	L-shell (R_E)								
LT	5.0 - 5.5	5.5 - 6.0	6.0 - 6.5	6.5 - 7.0	7.0 - 7.5	7.5 - 8.0	8.0 - 8.5	8.5 - 9.0	Total
00-01	0.0	327	75	13	274	465	534	0.0	1688
01-02	0.0	213	113	71	214	702	575	37	1925
02-03	0.0	164	164	139	46	232	899	11	1655
03-04	0.0	264	318	162	93	441	553	0.0	1831
04-05	0.0	357	211	235	452	286	392	58	1991
05-06	0.0	378	189	371	188	348	241	0.0	1715
06-07	0.0	454	250	233	88	405	84	0.0	1514
07-08	0.0	329	260	72	139	417	0.0	0.0	1217
08-09	50	364	242	148	588	175	0.0	0.0	1567
09-10	205	458	191	418	348	170	0.0	0.0	1790
10-11	240	489	235	462	215	183	0.0	0.0	1824
11-12	329	436	408	220	174	207	0.0	0.0	1774
12-13	354	567	440	86	350	39	0.0	0.0	1836
13-14	371	544	279	230	436	10	0.0	0.0	1870
14-15	295	581	60	489	519	153	0.0	0.0	2097
15-16	192	660	110	220	387	311	0.0	0.0	1880
16-17	49	423	333	231	227	473	0.0	0.0	1736
17-18	9	347	351	194	244	672	7	0.0	1824
18-19	4	260	244	319	303	620	137	0.0	1887
19-20	0.0	258	226	191	211	367	313	0.0	1566
20-21	0.0	111	361	121	315	102	514	0.0	1524
21-22	0.0	149	329	362	38	342	508	0.0	1728
22-23	0.0	227	196	568	38	265	676	0.0	1970
23-24	0.0	302	107	120	238	392	401	0.0	1560
Total	2098	8662	5692	5675	6125	7777	5834	106	41969

Table 5(c). SC5 Moment Data Set

KP 4, 5	L-shell (R_E)								
LT	5.0 - 5.5	5.5 - 6.0	6.0 - 6.5	6.5 - 7.0	7.0 - 7.5	7.5 - 8.0	8.0 - 8.5	8.5 - 9.0	Total
00-01	0.0	208	2	0.0	53	211	403	0.0	877
01-02	0.0	170	55	17	4	60	280	0.0	586
02-03	0.0	132	260	121	3	0.0	254	26	796
03-04	0.0	191	316	27	5	72	342	0.0	953
04-05	0.0	336	91	154	158	302	208	0.0	1249
05-06	4	349	21	349	116	370	29	0.0	1238
06-07	42	243	125	306	284	434	25	0.0	1459
07-08	42	185	377	115	210	169	0.0	0.0	1098
08-09	74	247	220	200	239	215	0.0	0.0	1195
09-10	106	317	163	115	92	89	0.0	0.0	882
10-11	87	256	153	79	186	126	0.0	0.0	887
11-12	119	136	212	139	148	84	0.0	0.0	838
12-13	142	197	88	62	298	0.0	0.0	0.0	787
13-14	155	116	63	72	145	0.0	0.0	0.0	551
14-15	211	154	50	154	186	0.0	0.0	0.0	755
15-16	87	237	167	171	178	68	0.0	0.0	908
16-17	0.0	414	98	138	132	159	0.0	0.0	941
17-18	0.0	345	57	175	115	165	0.0	0.0	857
18-19	0.0	152	191	67	242	83	121	0.0	856
19-20	0.0	86	223	141	173	77	59	0.0	759
20-21	0.0	103	285	330	78	50	105	30	981
21-22	0.0	92	135	330	205	73	8	0.0	843
22-23	0.0	86	79	323	153	293	133	0.0	1067
23-24	0.0	153	52	41	188	250	223	0.0	907
Total	1069	4905	3483	3626	3591	3350	2190	56	22270

Table 5(d). SC5 Moment Data Set

KP \geq 6-	L-shell (R_E)								Total
	5.0 - 5.5	5.5 - 6.0	6.0 - 6.5	6.5 - 7.0	7.0 - 7.5	7.5 - 8.0	8.0 - 8.5	8.5 - 9.0	
00-01	0.0	1	0.0	5	88	53	0.0	0.0	147
01-02	0.0	0.0	0.0	49	59	117	9	0.0	234
02-03	0.0	0.0	6	77	24	20	58	0.0	185
03-04	0.0	0.0	0.0	25	0.0	23	26	0.0	74
04-05	0.0	0.0	0.0	7	98	20	24	0.0	149
05-06	0.0	37	0.0	30	35	1	0.0	0.0	103
06-07	0.0	7	0.0	58	0.0	0.0	0.0	0.0	65
07-08	0.0	0.0	53	2	0.0	0.0	0.0	0.0	55
08-09	0.0	26	24	0.0	0.0	0.0	0.0	0.0	50
09-10	0.0	44	5	37	0.0	0.0	0.0	0.0	86
10-11	16	76	0.0	0.0	0.0	0.0	0.0	0.0	92
11-12	18	21	21	0.0	0.0	0.0	0.0	0.0	60
12-13	0.0	56	0.0	0.0	26	0.0	0.0	0.0	82
13-14	0.0	16	0.0	0.0	67	0.0	0.0	0.0	83
14-15	0.0	0.0	0.0	31	25	0.0	0.0	0.0	56
15-16	0.0	34	0.0	51	4	0.0	0.0	0.0	89
16-17	28	15	19	12	15	32	0.0	0.0	121
17-18	10	17	42	0.0	0.0	0.0	0.0	0.0	69
18-19	0.0	69	17	0.0	0.0	0.0	0.0	0.0	86
19-20	0.0	100	13	27	0.0	0.0	0.0	0.0	140
20-21	0.0	47	95	41	21	0.0	0.0	0.0	204
21-22	0.0	41	133	71	48	19	33	0.0	345
22-23	0.0	31	9	144	3	14	83	0.0	284
23-24	0.0	43	0.0	11	49	15	0.0	0.0	118
Total	72	681	437	678	562	314	233	0.0	2977

4.4 Data Analysis

Because of the number of different data bases and statistical analyses for the SC5 data, the data analysis section will be divided into three subsections. The first will deal with the flux distributions near perpendicular (90°) to the magnetic field, the next with the spin integrated moments of the distribution function, and the third with anisotropies in the fluxes.

4.4.1 FLUX DISTRIBUTIONS PERPENDICULAR TO THE MAGNETIC FIELD

The parallel detector flux file discussed in the previous section will be used here. The distribution of fluxes over KP, L-shell, and LT is nearly the same as for the moments that is given in Table 5(a through d). The only differences are due to editing of noise spikes from individual energy channels. The fluxes from the parallel detector represent particles mirroring near the equator, that is, particles with magnetic pitch angles of approximately 90° . First, we give scatter plots of the fluxes for sample energy channels as a function of L-shell, to show the kind of variation that is encountered at near-geosynchronous altitudes and to demonstrate at what energies L-shell variations become important. Second, the variation of the fluxes in LT is presented and shown to be significant for all energies, particularly for electrons. Third, spectra formed from flux averages in L-shell and KP are presented for representative LTs. Finally, spectra averaged over all times and L-shells are presented to show variation with magnetic activity.

Figure 7 shows the scatter of electron fluxes as a function of L-shell for detector channels with average energies 0.11, 1.5, 9.0, and 96 keV, plots a, b, c, and d, respectively. Clear dependence of the flux on L-shell for the L range 5.0 to 8.5 R_E is seen in the highest energy channel ($\bar{E} = 96$ keV). On examination of data from all SC5 channels, a regular decrease in flux with increase in L begins with the channel having $\bar{E} = 53$ keV. It is at approximately this energy that the effect of the convection electric field is negligible; the motions of electrons with energies above this value are dominated by the magnetic field alone. While no dependence on L is evident in Figure 7(b) and 7(c) for the 1.5- and 9-keV electrons, there appears to be a weak L-shell dependence in Figure 7(a) ($\bar{E} = 0.11$ keV). The dependence is confined to this channel (it does not appear in the next highest channel, $\bar{E} = 0.271$ keV). Since fluxes for all magnetic activities and LTs are included, this low energy variation may be due to expansion of the plasma-sphere into the lowest altitudes of the SCATHA orbit for low activities. We note that for a given energy the variation in electron flux is over approximately three orders of magnitude.

Figure 8(a) through 8(d) are corresponding plots for ion fluxes in channels with $E = 0.15$, 1.7, 10.4, and 126 keV, respectively. Again, the fluxes in the

ELECTRONS

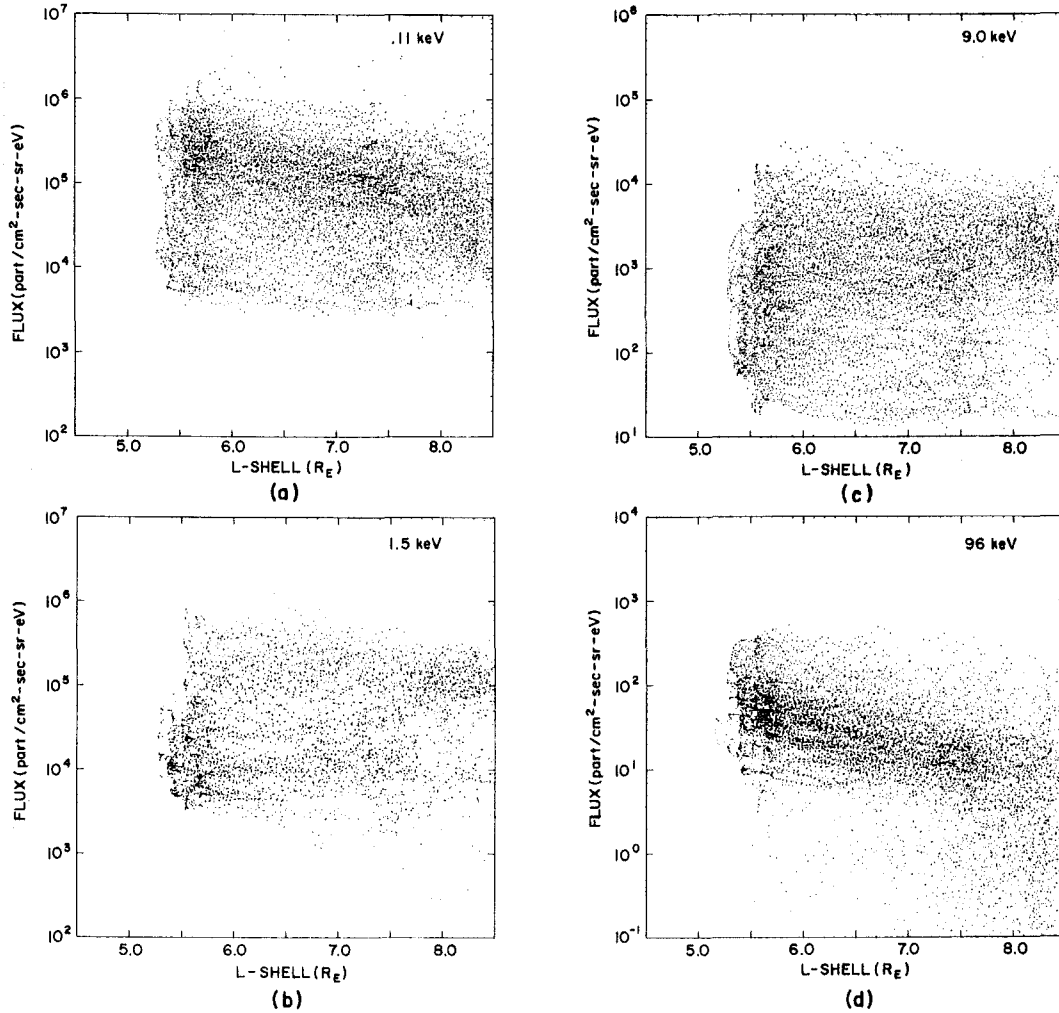


Figure 7. Distribution of Values of the Electron Differential Flux Measured Perpendicular to the Magnetic Field. The values are plotted vs L-shell and are for energy channels (a) $\bar{E} = 0.11$ keV, (b) $\bar{E} = 1.5$ keV, (c) $\bar{E} = 9.0$ keV, and (d) $\bar{E} = 96$ keV

highest energy channel are strongly ordered by L-shell (by magnetic field strength) while the lower energy fluxes are essentially independent of L. The dependence in L begins with $E = 25$ keV. The spread in the ion flux for a given energy is considerably less than that for electrons, being only ~ 2 orders of magnitude.

IONS

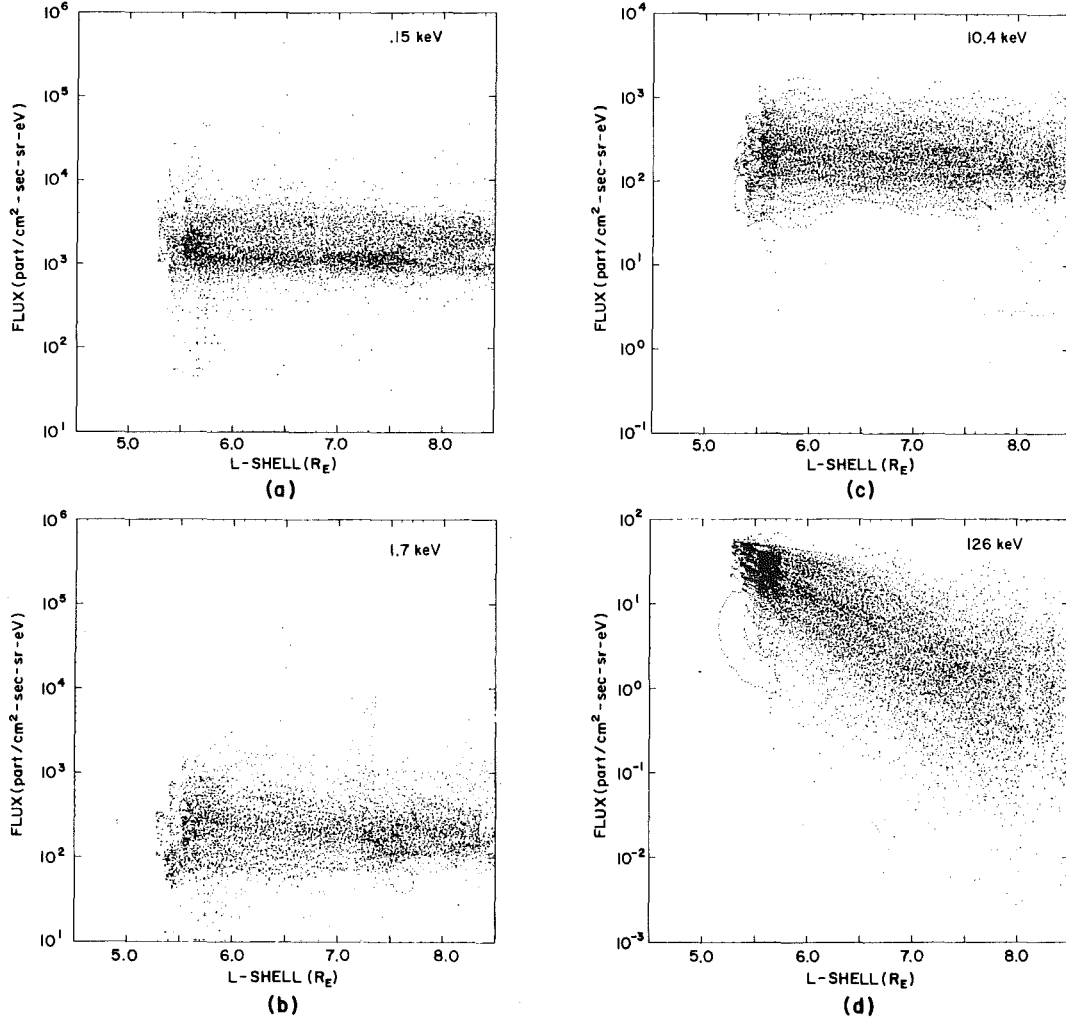


Figure 8. Distribution of Values of the Ion Differential Flux Measured Perpendicular to the Magnetic Field. The values are plotted vs L-shell and are for energy channels (a) $\bar{E} = 0.15$ keV, (b) $\bar{E} = 1.7$ keV, (c) $\bar{E} = 10.4$ keV, and (d) $\bar{E} = 126$ keV

Using the fact that the L-shell variations are minimal for the low-energy particles and well-ordered for the higher energies, we examine the flux variations in LT. Here we use averages in 1-h LT bins over all L values and for all magnetic activities. Scatter plots of all points were also examined to confirm that the average values were not unduly modified by spurious points. Figure 9 shows the average variations in LT for representative energy channels. For electrons the

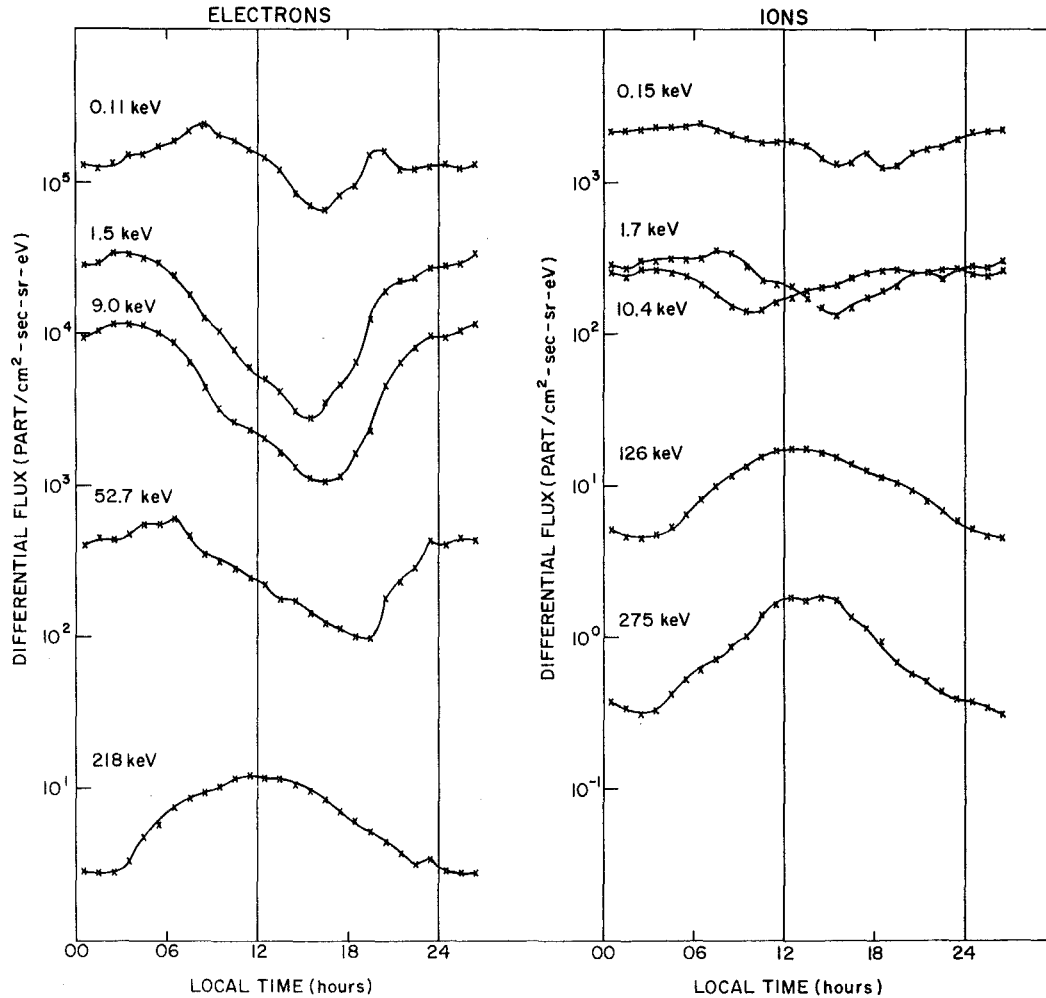


Figure 9. LT Variations of (a) Perpendicular Electron and (b) Ion Fluxes Averaged Over KP and L-shell for Selected Energy Channels

variations can be larger than an order of magnitude. The highest energy fluxes are dominated by the magnetic field. The fluxes are highest near local noon, where the field is compressed, and lowest at midnight, where the field is more taillike. At lower energies both electrons and ions show complex LT variations. For electrons the minimum moves systematically from 1600 to 1700 LT for $\bar{E} = 0.11$ keV through 1900 to 2000 LT for $\bar{E} = 52.7$ keV. In addition, the maximum fluxes occur postmidnight between 0300 and 0800 LT. The variations in the ions, while smaller in magnitude, are more complex than those of the electrons. The overall minimum varies in the opposite direction to the electrons, moving from 1900 to 2000 LT for $\bar{E} = 0.15$ keV through 0900 to 1000 LT for $\bar{E} = 10.4$ keV.

In fact, there appears to be little difference between the 1.7- and 10.4-keV flux values except for a rotation of the overall variation in LT. The maximum in the low energy ion fluxes is very broad over the whole nightside.

Figure 10 is an attempt to summarize the LT variations by presenting the full electron and ion spectra for representative LT. Here the differential number flux for electrons and ions is plotted against energy for 0000 to 0100, 0600 to 0700, 1200 to 1300, and 1500 to 1600 LT. These intervals represent the midnight, dawn, and noon sectors, and the position of the minimum low-energy electron flux, respectively. The electron and ion spectra, both show two-component populations, a lower one peaking at ~ 100 eV or less, and a higher one with peak values on the order of 1 keV for electrons and 10 keV for ions.

In the electrons, the flux peak of the higher component changes little with LT, indicating little change in average energy. The variation with LT is mainly one of intensity (or density). The spectral shape and intensity for this component varies little from midnight to dawn. By noon the intensity has dropped sharply. A minimum is reached between 1500 to 1600 LT with flux levels dropping by nearly an order of magnitude over the energy range from 1 to 10 keV.

The low-energy electron population peaks below the lowest energy channel. However, the slope of the flux becomes more negative as one proceeds from midnight to noon. This indicates that cooling of this population is taking place. While the magnitude of the fluxes also decreases from midnight to noon, the variation is not as great as for the higher energy population.

Compared to the electrons, the changes in the ions may be summarized as follows. The variations in the flux magnitudes for the high energy component are much smaller. A well-defined, broad peak in the fluxes defines the high-component average energy or temperature. The average energy increases rather dramatically from the 0000 to 0006 LT region (3 to 5 keV) to the postnoon region 1200 to 1600 LT (~ 20 keV) as a result of the decay of the 1- to 5-keV ion population. The low-energy ion population appears to peak in or near the lowest energy channel (0.15 keV). There is little change in this population from midnight to noon, but a decrease by about a factor of 2 from noon until 1500 to 1600 LT. No change in the average energy of the low-energy component is apparent.

Finally, we show the spectral changes as a function of magnetic activity. Figure 11 shows electron and ion spectra averaged over L-shell and LT for four KP bins: 0 to 1+; 2- to 3+; 4- to 5+; and ≥ 6 -. Many of the points concerning the general shape of the spectra have been made in the discussion of Figure 10. However, three additional points can be made. First, it is rather remarkable how minor the variation with magnetic activity is. Second, the changes, even more than with LT, appear to be principally in intensity, rather than in average energy. Some small amount of heating appears in the low-component electron population

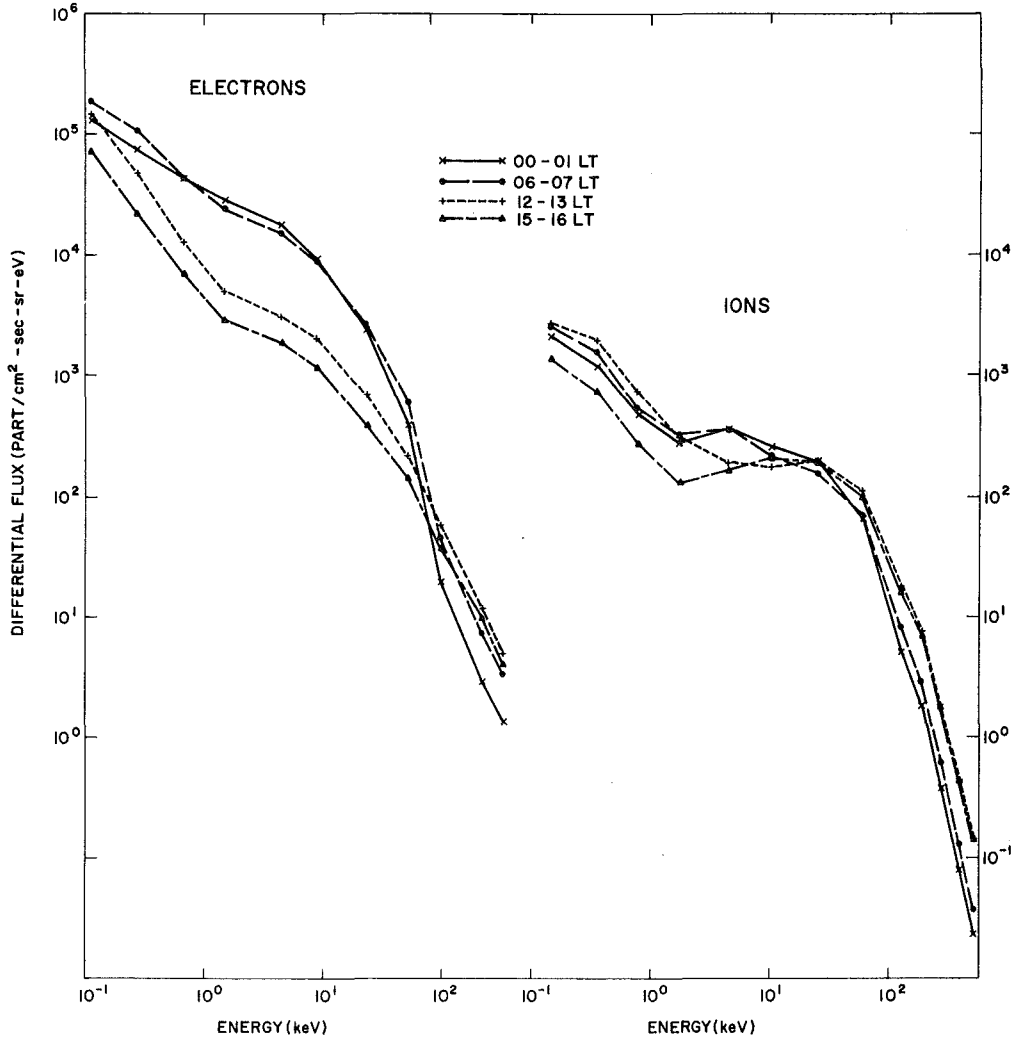


Figure 10. Differential Number Flux as a Function of Energy for (left) Perpendicular Electrons and (right) Ions for All KPs and L-shells for LT (x) = 0000-0100, (o) = 0600-0700, (+) = 1200-1300, and (Δ) = 1500-1600

with increasing magnetic activity. Third, between KP 4, 5 and $KP \geq 6$ - there is no change in the electron spectra for $E > 10$ keV, and in the ions for $E > 50$ keV. This indicates that a saturation level may have been reached. In Figure 11 the maximum values of the individual channel fluxes from the data set are indicated by the top dotted curve. The scatter overall is generally less than an order of magnitude.

We summarize the flux variations, using three energy ranges, ~ 50 keV, 1 to 50, and 0.1 to 1 keV. Above ~ 50 keV the electrons and ions are dominated by the

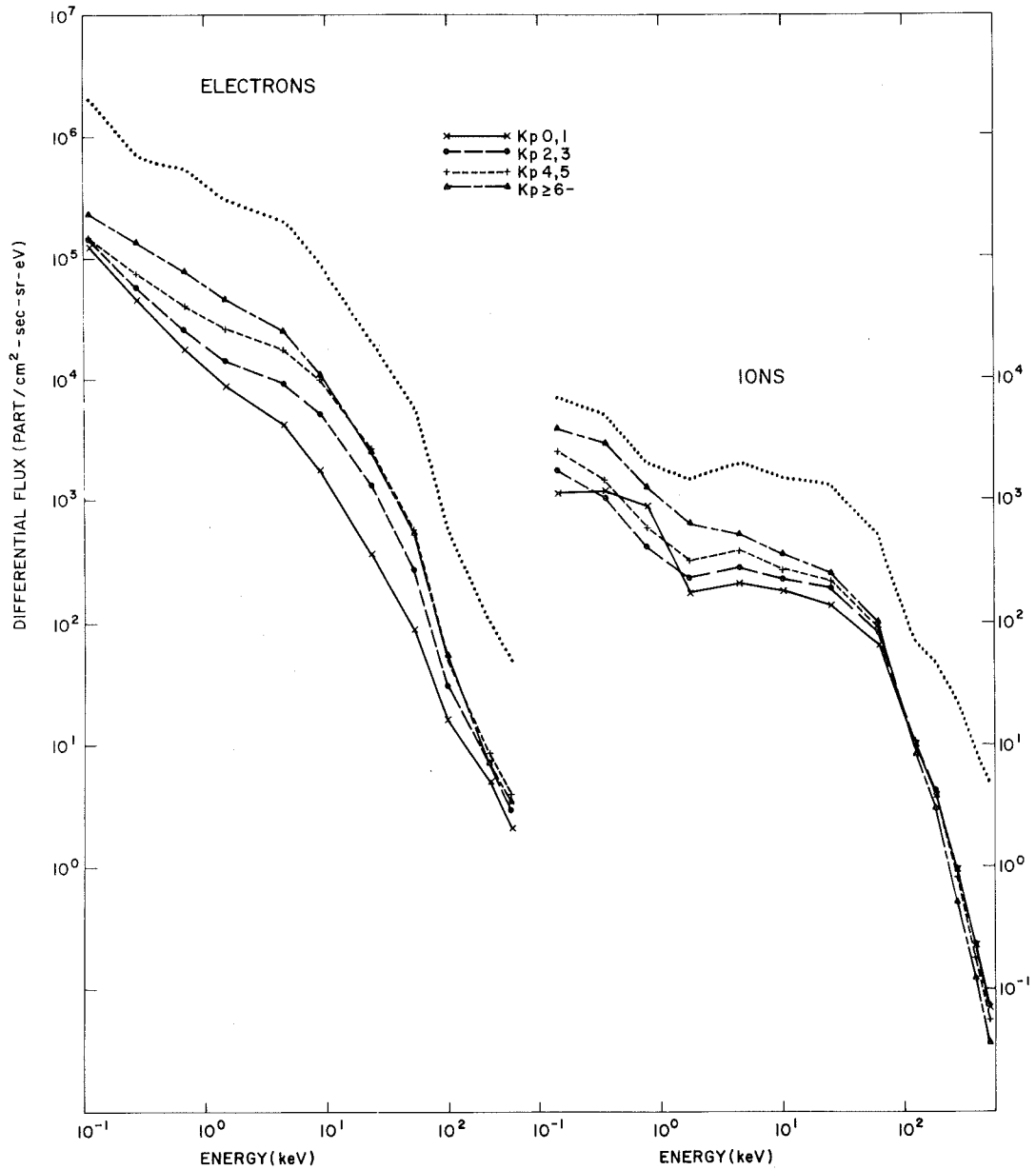


Figure 11. Differential Number Flux as a Function of Energy for (left) Perpendicular Electrons and (right) Ions for All LT and L-shells for KP Ranges: (x) = 0, 1+, (o) = 2-, 3+, (+) = 4-, 5+, and (Δ) \geq 6-. The top curves represent maximum flux values for the data set

magnetic field. They have higher fluxes for higher values of B. Since L for this data set was determined from a quiet Olson-Pfizer magnetic field model, the

high-energy particle fluxes fall off with L for all LT, and increase systematically from midnight to noon. The fluxes in this energy range increase with KP up to KP 4, beyond which they remain, on the average, the same.

Between 1 and 50 keV the electrons and ions have little L-shell dependence, but have a strong LT dependence. The electron fluxes maximize between midnight and dawn, and minimize postnoon. The LT dependence of the ion fluxes is weaker than for the electrons. It has a broad maximum throughout the nightside and has energy dependent minima on the dayside. The temperature, or average energy of the ions in this energy range maximizes in the postnoon region, and minimizes in the postmidnight region. The fluxes of both components increase systematically with increasing KP.

Between 0.1 and 1 keV the electrons cool both as a function of LT and as a function of KP. They have their lowest average energies near noon and for the lowest KPs. The intensities of both the low energy ions and electrons decrease from midnight to noon. They also decrease with magnetic activity. The low energy ion behavior for KP, 0 to 1+, is anomalous.

Finally, it should be noted that when dealing with individual moments of the distribution function, as will be done below, variations that are energy dependent will be obscured and can only be recovered by examining in great detail the way the changes vary between moments derived for different energy ranges. Thus, we will refer to the energy dependent changes in the fluxes perpendicular to the magnetic field discussed here to help interpret the moment results.

4.4.2 MOMENTS

The moment files discussed in Section 4.3 will be used here. The distribution of the moments over KP, L-shell, and LT is that given earlier in Tables 5(a) through 5(d). The moments of a distribution function can be mainly used in two ways. First, they can be used to reconstruct a representation of the distribution function whether it be an actual or an average distribution function (which is all that can be done here from the spin-averaged moments). Second, they can be used to better understand the dynamics of charged particle interactions, since the moments are the quantities that appear in the hydromagnetic approximation of the Vlasov equation for "collisionless" interactions. For a single-Maxwellian particle distribution only the zeroth and second moments are needed to define the density (n) and temperature ($kT = 2/3 \epsilon/n$). Similarly, for a multiple Maxwellian distribution function the densities and temperatures for each Maxwellian can be determined by using the same moments over the appropriate energy ranges and correcting for energy cutoff effects. Because higher moments place greater weight on higher energies, the moments can also be used to study particle variations as a function of energy.

The average behavior of the four moments with LT, L-shell, and KP are given in Figures 12 through 15. In each case the averages are calculated, varying only a single parameter, (a) for the entire energy range of the detector, from ~ 100 eV to 400 keV, and (b) for the high energy range, from ~ 200 to 400 keV. Since the moments for the total energy range are just sums of the moments of the high and low ranges, the moments for the low energy range (~ 100 eV to 20 keV) can be determined. The moments for electrons and ions are shown as separate lines on the same plot for each figure. The moments for the ions are calculated assuming the total ion population to be hydrogen; that is, the mass of hydrogen was used in Eqs. (2) through (7). This assumption affects the number density and the energy density. Corrections to certain moment results using ion composition measurements from the SC8 experiment are given in Appendix B.

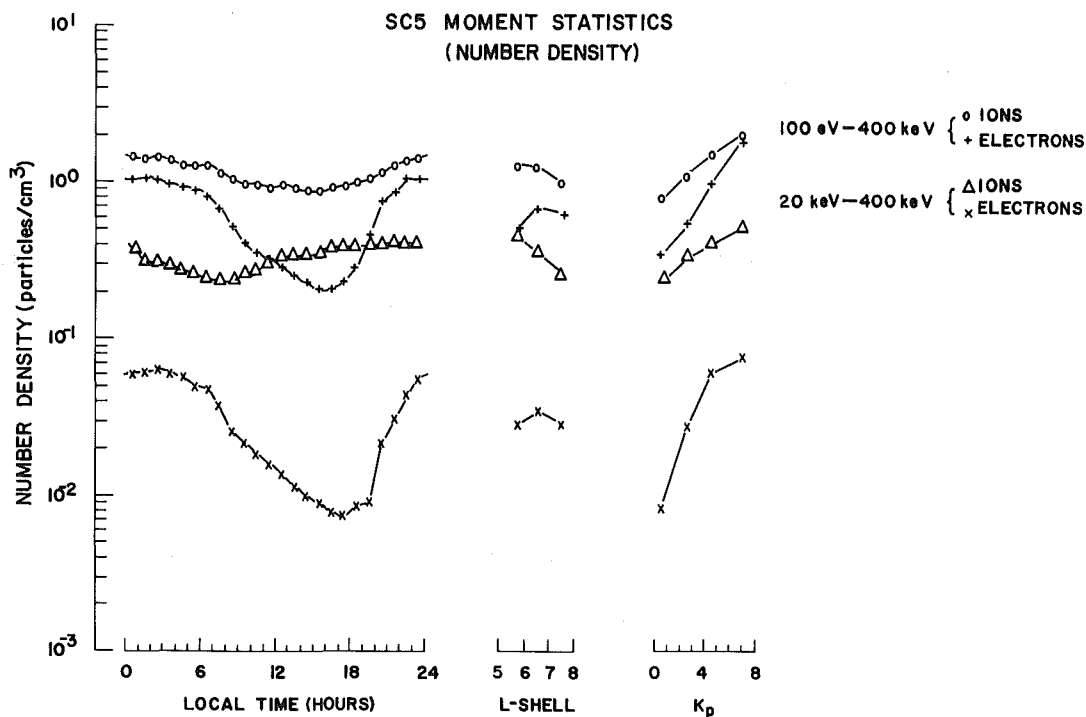


Figure 12. SC5 Number Densities for Ions and Electrons as Determined From Spin-averaged Moments for Energy Ranges 100 eV to 400 keV and 20 to 400 keV. The average number densities are plotted vs (left) LT, (center) L-shell, and (right) KP

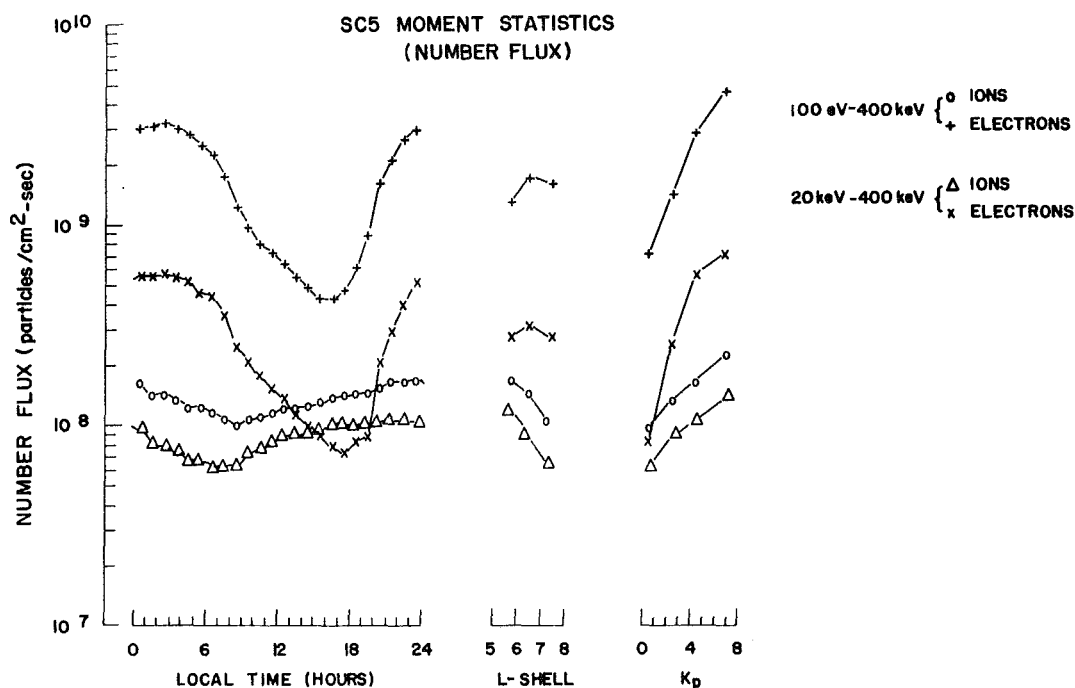


Figure 13. SC5 Number Fluxes for Ions and Electrons as Determined From Spin-averaged Moments for Energy Ranges 100 eV to 400 keV and 20 to 400 keV. The average number fluxes are plotted vs (left) LT, (center) L-shell, and (right) K_p

Perhaps the most striking feature in Figures 12 through 15 is the fact that the moments for each species behave in essentially the same way. (The differences will be pointed out later.) For the electrons there are large variations with K_p and LT and with little variation in L. The ions vary most with K_p, but also have significant and well-defined variations in LT and L. The variation in LT for electrons shows a minimum near dusk; for ions (with the exception of the total density) the minimum is near dawn. The sameness of the variations with increasing moments indicates a strong dependence of each moment on the lowest moment. This means that the average energy (or temperature, when distributions are Maxwellian) changes little over the near-geosynchronous regime. We will show this to be the case in discussions of individual moments. Because of the similar behavior of all the moments, emphasis is placed on the zeroth moment: number density.

4.4.2.1 Number Density

In this section we compare the obvious aspects of the total plasma (the ions and electrons together) and then discuss the global variations of the high and low

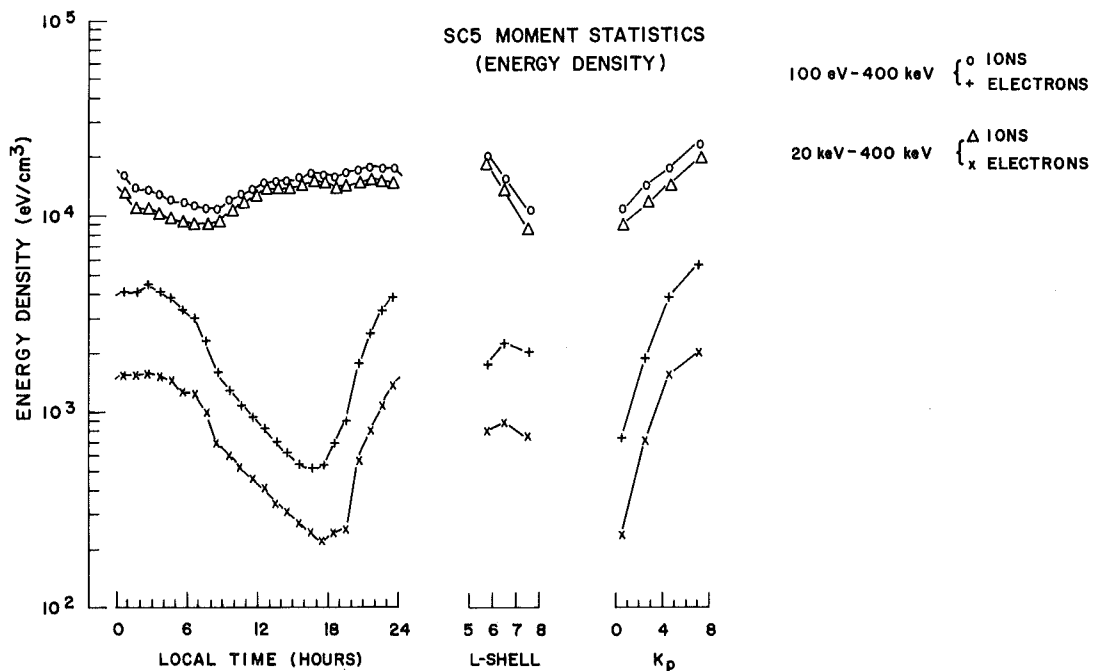


Figure 14. SC5 Energy Densities for Ions and Electrons as Determined From Spin-averaged Moments for Energy Ranges 100 eV to 400 keV and 20 to 400 keV. The average energy densities are plotted vs (left) LT, (center) L-shell, and (right) KP

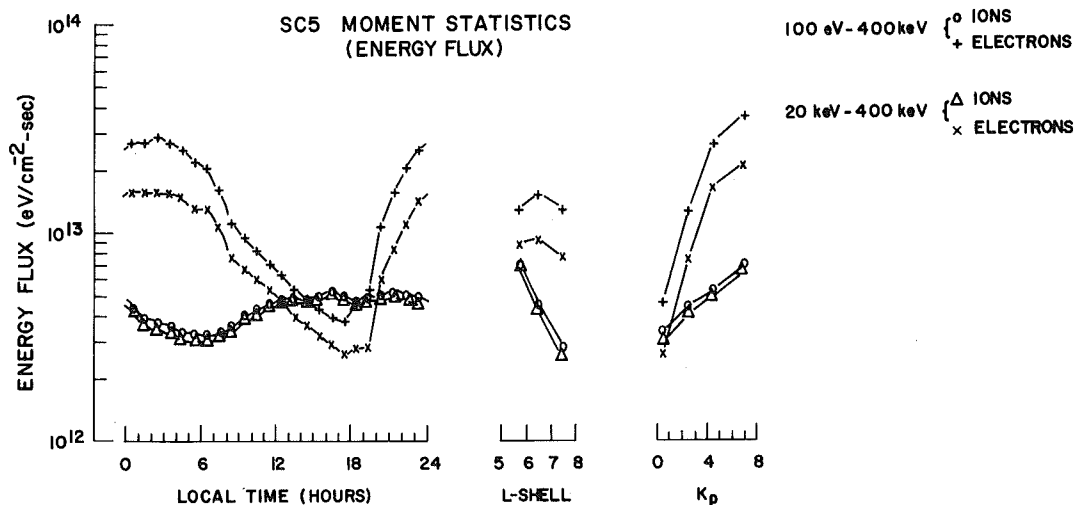


Figure 15. SC5 Energy Fluxes for Ions and Electrons as Determined From Spin-averaged Moments for Energy Ranges 100 eV to 400 keV and 20 to 400 keV. The average energy fluxes are plotted vs (left) LT, (center) L-shell, and (right) KP

populations of each species in detail. Figure 12 shows clearly that the measured ion and electron densities over the energy range 100 eV to 400 keV are not equal. When corrections are made to the ion density for ion composition the discrepancy is even greater (see Appendix B). The lower limit in energy detectability of SC5 for both species is ~ 50 eV (given the energy response width of the lowest channel). While a significant portion of the ion population could lie below this energy, there can be no doubt that a significant portion of the electron population must lie there; that is, charge neutrality must be maintained. The average spectra shown in Figure 10 also suggests this, since the low energy ion peak appears to be in the range of the lowest energy detector, while the electron distribution is still rising steeply with decreasing energy. (It is also often observed that the lowest energy SC5 ion channels are at background levels, while counts well above background are always seen in corresponding channels for electrons). The measured electron density is closest to the ion density in the midnight sector and for high values of KP. The difference is greatest on the dayside, for low L and low KP.

The amount of variability within each of the two species is also quite different. In the averages shown in Figure 12 the total ion density varies at most by a factor of 3, while the total electron density varies by up to a factor of 6. From scatter plots of the total moment number density data set the ion density can be seen to change by a factor of 20, from 0.2 to 4 cm^{-3} , while the electron density changes by a factor of 200, from 0.02 to 4 cm^{-3} . Of the three variables, LT, L, and KP, the largest average variation for both species is with KP. The LT variation of the total ion density is similar to that of the total electron density; that is, they both have minima between 1400 and 1700 LT. The high-energy ion density, on the other hand, has its minimum near dawn. (The reason for this will be discussed in Section 5.) The total density for each species depends least on L-shell. The peak of the ion density is, on the average, earthward of both $L = 5.5 R_E$ and the peak in the electron density, which lies between $L = 6$ and $7 R_E$.

For the high energy (20 to 400 keV) particle densities, the following additional observations can be made from Figure 12. The high-energy electrons constitute between 4 to 6 percent of the total electron density over the 100 eV to 400 keV range; and the high-energy ions, 20 to 25 percent of the total ion density. The LT variation in the high-energy electrons is similar to, but greater than that, of the total, and the minimum is shifted closer to dusk (~ 1800 LT). The high-energy ion density increases regularly with decreasing L-shell, while the high-energy electron density peaks between $L = 6$ and $7 R_E$. Both high-energy populations increase with KP. The high-energy electron density increase is very steep from low to moderate KP and appears to approach an upper limit at the highest KP values.

Although the density averages for all but a single parameter show systematic and regular changes in the near-geosynchronous regime, their standard deviations are large, approximately equal to the average values themselves. This is further amplification of two important aspects of the geosynchronous regime. First, that it is a highly dynamic region in space, particularly in the midnight sector; and second, that it variably lies in different plasma regimes as was indicated in Section 3. To reduce some of the dynamical effects in the data and to try and restrict our analysis to regions outside the plasmasphere we will next examine only those data taken for KP levels, 2- to 3+; that is, for moderate levels of magnetic activity. For lower values of KP SCATHA typically passes through the plasmasphere. Thus, the KP 2,3 data set represents the least dynamic conditions for which plasma-sheet characteristics can be studied.

Figure 16 (a) through 16 (d) gives the density variations for KP 2,3 in hourly LT bins and for L-shell bins of $1 R_E$. The electron and ion densities are shown as grey scale levels for both high- and low-energy ranges. The low-energy ion densities have been corrected for ion composition (see Appendix B for the uncorrected values and for the method of correction.) The density scale is logarithmic for all but the lowest values which are grouped together. Each successive level of darkness indicates an increase in density by approximately 2 to 2.5. The same scale is used for each panel; however, to do this the high energy electrons [Figure 16(a)] were first multiplied by a factor of 10.

In addition to the types of variations one sees in the single parameter averages, Figure 16 gives evidence for the types of trajectories followed by the particles. If we assume the particles enter the near-geosynchronous regime on the nightside from higher L-values than these sampled (say $L = 10 R_E$ or greater) and that their trajectories are similar to those discussed in Section 3, the density maximizes where the trajectories "pile up" as the electrons turn and move eastward, and the ions (high energy) westward.

The low-energy ion densities do not show a clear maximum in the SCATHA altitude range and are fairly uniformly distributed within the region. They constitute about 75 percent of the measured ion population with values between 0.5 and 2 cm^{-3} . The low energy ion trajectories carry the bulk of the nightside population earthward of the sampling region. Here they either sustain few losses and reappear in the SCATHA regime on the dayside, or they precipitate and are replenished on the dayside by another ion source region. The change in ion composition from the midnight to the noon sector (See Section 5) is evidence for the latter.

The low-energy electron density is given in Figure 16(d). The electrons in this range constitute more than 90 percent of the measured electron population. Low-energy electron trajectories are ordered by a tear-drop shaped, forbidden region. A minimum density should occur near dusk where electrons from the tail

NUMBER DENSITY Kp 2,3

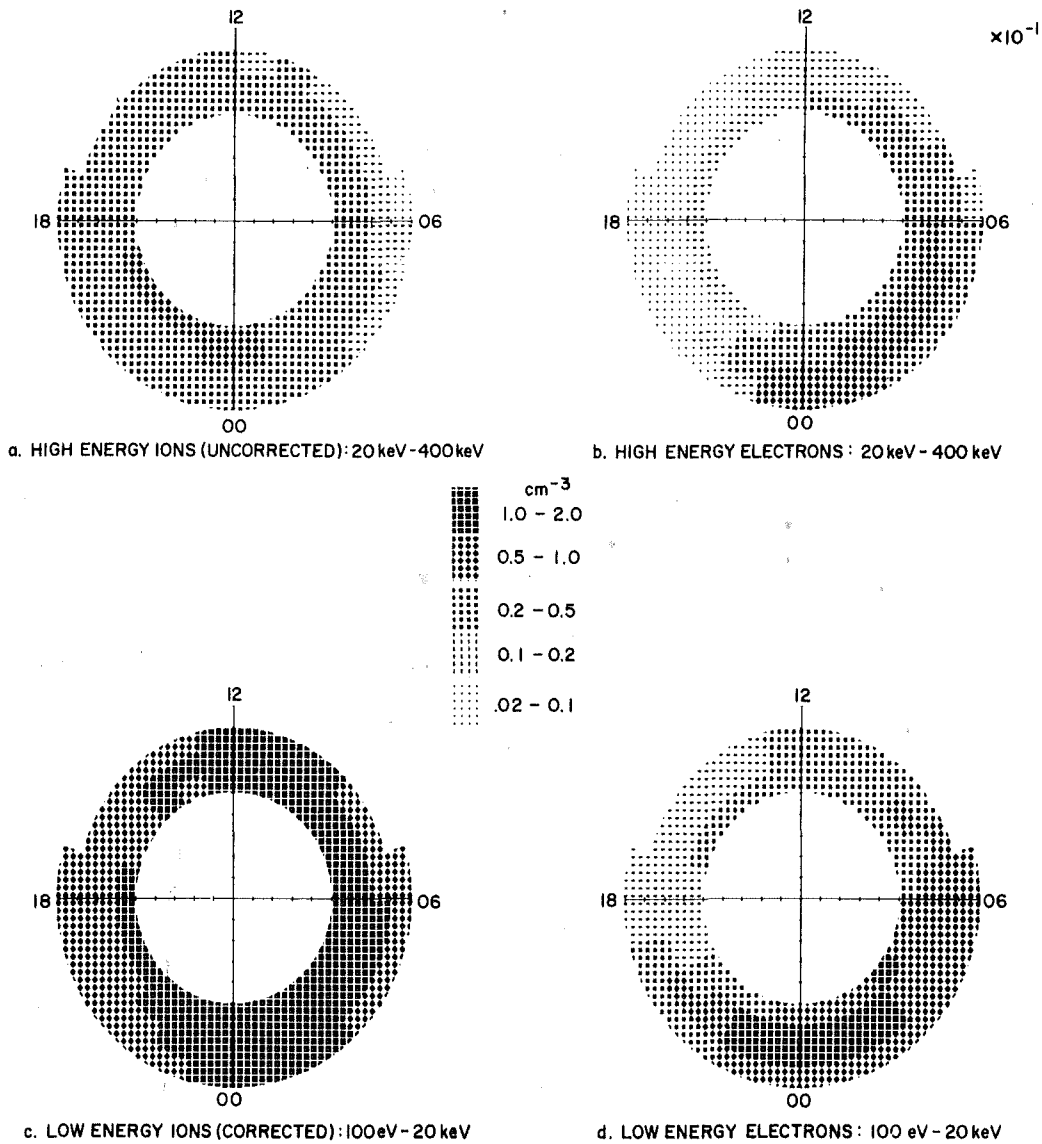


Figure 16. Variations in Number Density Coded in Polar Coordinate LT and L-shell Ranges. The densities are for (a) high-energy ions, (b) high-energy electrons, (c) low-energy ions, and (d) low-energy electrons. The code is in the center in particles/cm³ and values in (b) must be multiplied by 10⁻¹

region turn eastward to avoid the forbidden region, or where those electrons that have circulated through the noon sector are deflected out toward the dayside magnetopause. This is clearly the case in Figure 16(d). There is also a decrease in density between $\sim 0300 - 0900$ LT, not explainable by particle trajectories. The decrease is most readily explained by particle loss through precipitation. A similar decrease occurs in the high energy electrons [Figure 16(b)].

The decrease in the total electron density from 0200 to 1600 LT is shown in Figure 17 in greater detail. The x's (+'s) represent densities for L values 6 to 7 R_E (7 to 8 R_E). The maximum density near midnight is $\sim 1.1 \text{ cm}^{-3}$, and the minimum density near 1800 LT $\sim 0.12 \text{ cm}^{-3}$. There is no significant difference in density for the two L-intervals. Two distinct rates of decrease apply, one from 0200 to 0600 LT, and one from 0600 to 1600 LT. The former is less than the latter. Since the points approximate a straight line on a log-log plot, the two rates of decrease are clearly exponential. The results of the linear regressions on $\ln n$ (density) vs ϕ (LT from midnight) are shown as straight lines in Figure 17. The correlation coefficients for both fits were > 0.98 . The derived relationships are

$$n = 1.38 e^{-0.095 \phi} \text{ cm}^{-3} \quad (0200 \text{ to } 0600 \text{ LT}) \quad (9)$$

and

$$n = 2.22 e^{-0.183 \phi} \text{ cm}^{-3} \quad (0600 \text{ to } 1600 \text{ LT}) \quad (10)$$

In the first case the e-folding time is 10.5 h; in the second, 5.5 h in LT. (LT used here is only a measure of distance.) If the electrons are corotating on shells of constant B (a good zeroth order approximation in the dawnside), then LT tracks the particles and ϕ can be equated to actual time of decay.

For KP 2, 3 the electron loss rate is very well-ordered. For KP 4, 5 the dawn-sector electron decay differs from that of KP 2, 3 in the following ways. First, the density remains nearly constant at a value of $\sim 1.5 \text{ cm}^{-3}$ until 0600 LT for both the L = 6 to 7 R_E and L = 7 to 8 R_E regions. Thus, the e-folding time for the period from 0200 to 0600 LT is essentially infinite (no losses). Second, the density reaches a minimum value much earlier, between 1200 and 1400 LT. (The minimum density is nearly the same as for KP 2, 3, that is, 0.12 cm^{-3} .) Thus the e-folding LT is shorter than for KP 2, 3. This implies that the loss mechanism on the dayside is more efficient as magnetic activity increases. In addition, for higher activity the e-folding rate develops a dependence on L, decreasing as L increases.

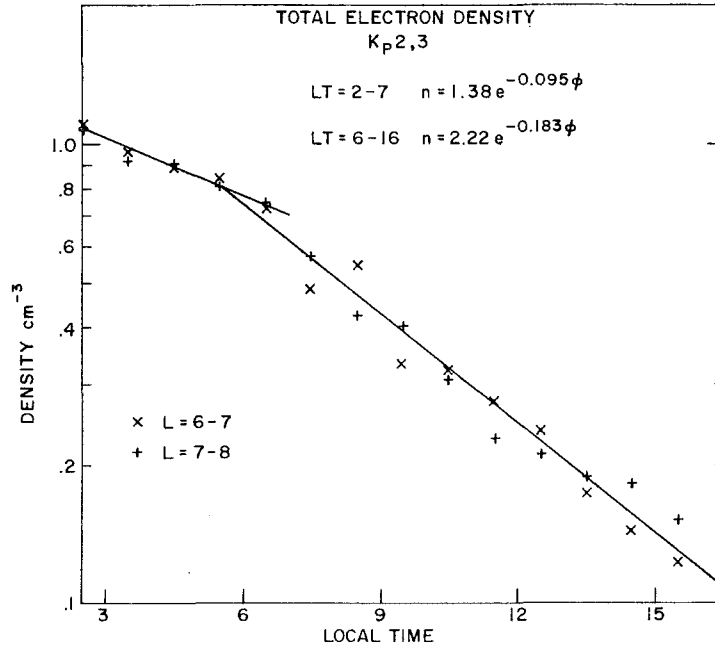


Figure 17. The Average Total Electron Density vs LT From 0200 to 1600 for a KP Range From 2- to 3+ for L-shells: (x) = 6 to 7 R_E and (+) = 7 to 8 R_E . Linear regression fits to the data from 0200 to 0700 LT and from 0600 to 1600 LT are included on the plot

The high-energy ion and electron densities for KP 2, 3 shown in Figure 16(a) and 16(b) are extremely well-ordered, and maximize premidnight and postmidnight, respectively. If the density maximum is used to determine the penetration depth, the ions penetrate earthward of the electrons by an L radius of $\sim 1.5 R_E$. As in the case of the low energy particles, high energy electron loss rates are substantially larger than those for high energy ions. There are essentially no high-energy electrons from 1400 to 2100 LT in the evening sector.

Scatter plots of ion vs electron densities for the different energy ranges show no patterned relationships. Since ion and electron populations occur in reasonable agreement with simple trajectory calculations and since they have very different loss rates, we conclude that particles in the energy range 100 eV to 400 keV are mainly indifferent to the process of maintaining charge neutrality.

For comparison to other data sets, Tables 6 and 7 give average values of the total electron and ion (uncorrected for ion composition), densities for representative LT, L-shells, and KP levels.

Table 6. 100 eV to 400 keV Electron Densities (cm^{-3}) for KP Levels 2, 3 (4, 5)

	LT			
	2300-0100	0500-0700	1100-1300	1700-1900
L-shell (R_E)				
5.5 - 6	0.8 (1.9)	0.9 (1.0)	0.3 (0.6)	0.2 (0.4)
6 - 7	1.4 (2.9)	0.8 (1.4)	0.25 (0.3)	0.1 (0.3)
7 - 8	1.1 (1.6)	0.8 (1.4)	0.2 (0.15)	0.2 (0.6)
8 - 8.5	0.9 (0.7)	0.6 (0.9)		0.1 (0.3)

Table 7. 100 eV to 400 keV Uncorrected Ion Densities (cm^{-3}) for KP Levels 2, 3 (4, 5)

	LT			
	2300-0100	0500-0700	1100-1300	1700-1900
L-shell (R_E)				
5.5 - 6	1.7 (2.6)	1.4 (2.4)	1.1 (1.3)	1.2 (1.5)
6 - 7	1.8 (2.5)	1.1 (2.3)	1.1 (1.2)	1.0 (1.4)
7 - 8	1.4 (1.8)	0.9 (1.3)	0.9 (0.7)	1.0 (1.0)
8 - 8.5	1.3 (1.2)	0.7 (0.6)		0.8 (0.6)

4.4.2.2 Energy Density (ϵ)

Figure 14 shows total average variations in the energy density, or particle pressure, with LT, L-shell, and KP level. Throughout the following we use energy density and pressure interchangeably. For an isotropic plasma they are related by a factor of $2/3$: $P = 2/3(\epsilon_I + \epsilon_E)$. For an anisotropic distribution additional information is required to determine the pressure tensor. However, the energy density is well-defined in all cases (Eq. 6). The average ion energy density is greater than that of the electrons by at least a factor of 3. And, the energy density of the high-energy ion component (20 to 400 keV) constitutes a large fraction of the total ion pressure. The total energy density (ions plus electrons) depends significantly on KP, L, and LT. In addition, the contribution each of the four populations make to the total varies greatly. In the midnight sector where the electron population is not eroded by precipitation losses, the electron contribution to the total pressure is approximately 10 to 30 percent depending on

activity and L-shell. Toward dawn the contribution of the electrons maximizes since electron trajectories are eastward and high energy ion trajectories are westward. Here electron pressure can be as much as 50 percent of the total pressure. On the dayside and through the evening sector the electron contribution falls to a few percent of the total, both because of electron inaccessibility and/or loss and because the dusk region is populated by the high-energy ions convecting westward from the midnight sector.

Tables 8 and 9 list the percentage contributions to the total pressure of the total electrons and the high-energy ions, respectively, for representative LT, L-shells, and KP levels. From Table 8 one can see that in addition to the LT variations mentioned, the electron percentage increases both with L and with magnetic activity (except at low L-shells in the evening sector). The L-dependence could have been expected from examining the number densities in Figure 12 since the electron number density is nearly constant in L while the ion density decreases with increasing L.

Table 8. Percentage Electron Energy Density for KP Levels 2, 3 (4, 5)

	LT			
	2300-0100	0500-0700	1100-1300	1700-1900
L-shell (R_E)				
5.5 - 6	9.5 (20.0)	12.5 (20.0)	4.5 (6.0)	3.0 (2.5)
6 - 7	14.0 (25.0)	21.0 (30.0)	5.5 (7.0)	2.0 (2.0)
7 - 8	22.0 (29.5)	28.0 (32.0)	8.0 (7.5)	3.0 (9.0)
8 - 8.5	26.0 (25.5)	36.5 (47.5)		4.5 (20.0)

Table 9. Percentage High-energy Ion Energy Density for KP Levels 2, 3 (4, 5)

	LT			
	2300-0100	0500-0700	1100-1300	1700-1900
L-shell (R_E)				
5.5 - 6	78.0 (65.5)	77.5 (65.0)	89.0 (88.5)	85.0 (88.5)
6 - 7	72.5 (57.5)	64.0 (49.0)	84.0 (80.5)	86.0 (88.5)
7 - 8	64.0 (56.5)	55.0 (46.5)	77.5 (79.5)	81.0 (77.5)
8 - 8.5	60.0 (62.5)	43.5 (31.5)		78.0 (68.0)

Table 9 shows the dominance of the high-energy ion population in the total pressure, particularly in the noon and evening sectors, where it can constitute nearly 90 percent of the total. Tables 8 and 9 together show that the low-energy ion population constitutes between 5 to 25 percent of the total pressure. Generally it is around 15 percent.

Values of the total pressure ($P_E + P_I$) are given in Table 10 for the same ranges of LT, L-shell, and KP used earlier. In all cases except one, the pressure maxima are more earthward than the sampling region extends. The one exception is in the midnight sector for KP 2, 3, which shows a maximum for L between 6 and 7 R_E . Generally, the pressure falls from a value greater than 20 keV/cm^3 at $L = 5.5 R_E$ to one less than 10 keV/cm^3 at $L = 8.5 R_E$ with overall gradients, positive toward the Earth, of 4 to 12 $\text{keV/cm}^3/L$. The gradients depend strongly on magnetic activity and increase between KP ranges 2, 3 and 4, 5 by a factor of 2.

Table 10. Total Energy Density ($\epsilon_I + \epsilon_E$) keV/cm^3 , for KP Levels 2, 3 (4, 5)

	LT			
	2300-0100	0500-0700	1100-1300	1700-1900
L-shell (R_E)				
5.5 - 6	27.5 (37.6)	20.4 (27.9)	22.6 (25.5)	22.2 (34.2)
6 - 7	29.7 (34.1)	14.3 (19.8)	14.0 (15.4)	17.9 (29.3)
7 - 8	19.8 (26.8)	10.7 (15.2)	9.1 (9.5)	13.8 (16.7)
8 - 8.5	16.7 (16.7)	6.4 (6.2)		9.2 (7.5)

The variations in the total energy density are sufficiently complex that to elucidate them another form of presentation is necessary. Figure 18 shows contours of constant energy density for three KP ranges: 0 to 1+; 2- to 3+; and 4- to 5+. For a magnetic field B perpendicular to and pointing out of the plane of Figure 18 and for an isotropic plasma ($P = P_I$), contours of constant P would lie along the direction of $\underline{B} \times \underline{\nabla}P/B^2$ or in the direction of the ring current. This direction (generally clockwise) is marked with arrows on the figure. The contour lines are in increments of 5 keV/cm^3 . Over the magnetospheric volume sampled, the particle pressure increases systematically with increased magnetic activity. The increase appears to emanate from within the lowest L-value displayed, 5.5 R_E . The pressure at $L = 5.5 R_E$ increases from $\sim 15 \text{ keV/cm}^3$ at KP 0, 1; to

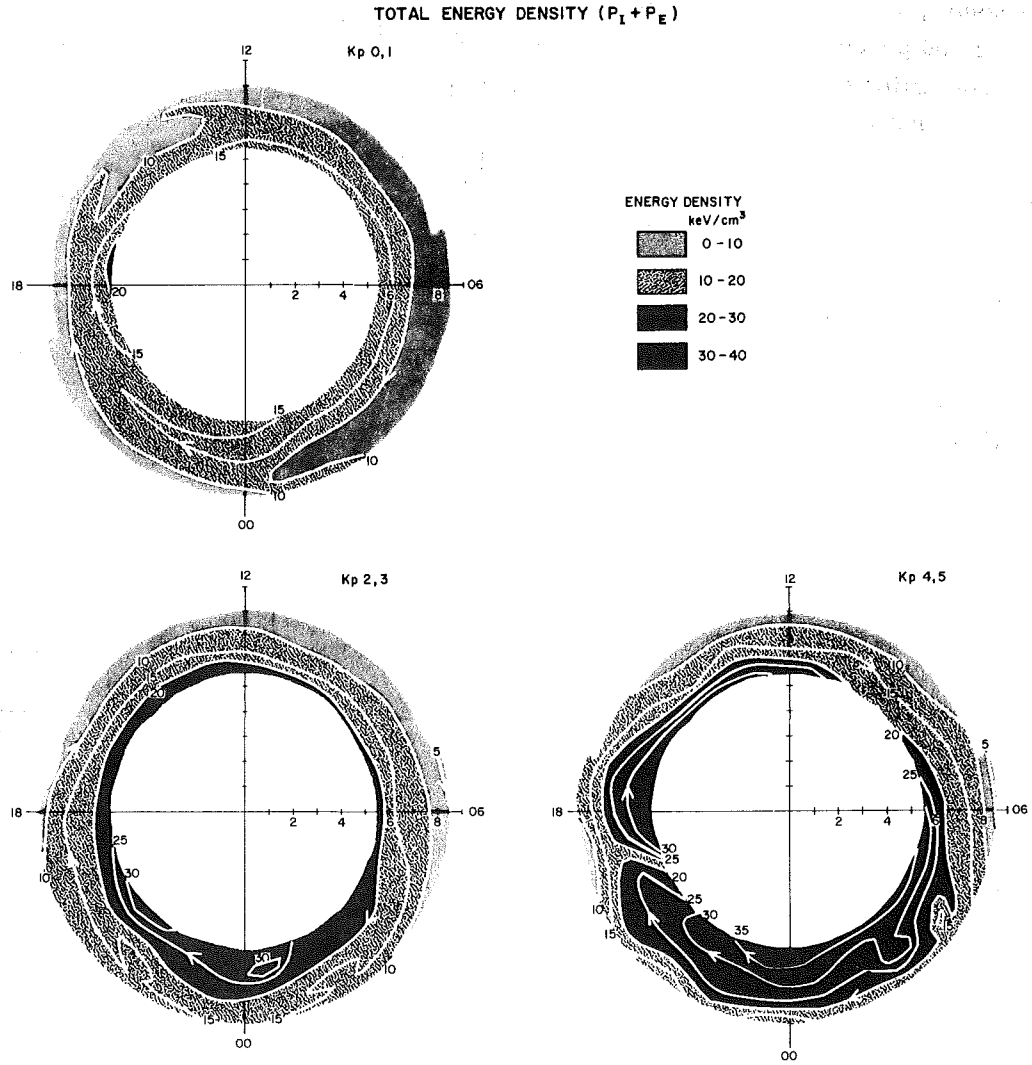


Figure 18. Contours of Constant Total Energy Density (ϵ_I and ϵ_E) in Polar Coordinate L-shell and LT Plots for KP: (a) KP = 0, 1; (b) KP = 2, 3; and (c) KP = 4, 5. The density range code is in the upper-right corner and arrows mark the direction of ring current flow

$\sim 25 \text{ keV/cm}^3$ at KP 2, 3; to $\sim 35 \text{ keV/cm}^3$ at KP 4, 5. The pressure at the largest L-values (8 to $8.5 R_E$) however, remain more nearly constant, particularly on the dayside. Thus, the gradient in P, as noted above and as can be seen by the density of contour lines, increases systematically with KP in the sampled region. At the same time, the peak in the pressure moves earthward with increasing KP. For KP 0, 1 the maximum pressure in the midnight sector lies between L = 6 and

$7 R_E$, as indicated by the reverse in the current direction. For KP 2, 3 the maximum pressure also lies between $L = 6$ and $7 R_E$ in the midnight sector, but lies earthward of $L = 5.5 R_E$ for all other LT. For KP 4, 5 the maximum pressure is earthward of $L = 5.5 R_E$ for all LT. The symmetry of contours of constant pressure also changes with KP. Except for postnoon and postmidnight tail-like extensions of the higher pressure regions, the KP 0, 1 contours are quite circular. The next level of magnetic activity, KP 2, 3, shows greater pressure inflation on the nightside, or oval-shaped contours. At the highest activity levels shown (KP 4, 5) the pressure inflation extends into all but the 0600 to 1200 LT sector where the contours flatten out. It is also evident that the structure of the contours becomes more irregular with increasing magnetic activity. This suggests that the notion of concentric circular pressure contours for the whole inner magnetosphere is too simplistic.

4.4.2.3 Average Energy (ϵ/n) .

For a system in thermal equilibrium a temperature T can be assigned to the system. In addition, if the system is composed of ideal gases and has three degrees of freedom, the equation of state for each component is of the form $P = nkT$ where P is pressure, n is density, T is temperature, and k is the Boltzmann constant. For ionized plasmas accompanied by or immersed in magnetic fields the concept of temperature is not useful at best, and can often be deceptive. Such systems are generally not isotropic and not in thermal equilibrium. For such systems the more fundamental relationship is that between particle pressure and density. The ratio of these two moments gives an average energy over the energy range used in calculating the moments and for the given species. Further, the functional relationship between P and n is useful in hydro-magnetic modeling. Generally one looks for a relationship of the form,

$$P \propto n^\gamma , \quad (11)$$

where γ is the polytropic index. For $\gamma = 1$ the average energy remains the same, and strong heating sources (sinks) must be available to maintain the average energy as the gas expands (contracts). At the other extreme, $\gamma = 5/3$ represents adiabatic expansion, in which case no heat sources are available. In the volume of the magnetosphere sampled here, the determination of the functional relationship between P and n is complicated by particle losses, both apparent (from trajectories leading into and out of the volume) and real (from particle precipitation), and source regions. It would be unrealistic to assume that these are all independent of particle energy; thus, the measured relationship between P and n will

contain information not only about plasma heating in the magnetosphere (which is the aim of the modeling procedure), but also about the source and loss processes.

Figure 19(a) through 19(d) gives scatter plots of the energy density vs number density for the four particle populations we are considering, high- and low-energy electrons and ions. Only every tenth point from the data set is included due to computer plotting limitations. The plots show that the high-energy populations are much more highly-ordered than the low-energy populations, and that the energy density is directly proportional to the number density in each case. The straight lines in Figure 19 pass through the centers of the distributions and have slopes equal to 1. Therefore, the average energy (ϵ/n) for the high energy populations is constant to a high degree. Values of the energy density for $n = 1 \text{ cm}^{-3}$ give the overall (all L, LT, and KP) average energy for the data set. For the high-energy ions $E_{AV} = 30 \text{ keV}$; for the corresponding electrons $E_{AV} = 22 \text{ keV}$.

The scatter of the low-energy populations from linearity is much greater. The low energy electron values [Figure 19(d)] appear to have two controlling mechanisms one for lower densities, and another for higher. The former has a smaller slope than the latter. In Figure 19(d) the solid line represents a constant E_{AV} and the dashed line an E_{AV} that would vary as $n^{2/3}$ ($\gamma = 5/3$).

Variations of the near-constant average energy are presented as a function of LT and L-shell in Figure 20(a) through 20(d). The 3-D plots correspond to the density plots in Figure 16(a) through 16(d), again for the KP range 2- to 3+. Because the variation in average energy is much smaller than that of number density and energy density, the grey scale used advances linearly from 10 to 50 keV for the high-energy populations, and from 1 to 4 keV for the low-energy populations. (Note that here the low average energies have been multiplied by 10 to use the same grey scale.)

As expected, the high-energy electrons [Figure 20(b)] show little variation in average energy over the entire sampled region. They vary by no more than a factor of 2 from 20 to 40 keV. The higher average energies are in the dusk region. The high-energy ion average energy, [Figure 20(a)] shows somewhat greater variation, by at most a factor of 3, from 20 to 60 keV. The variation is extremely well-ordered by L-shell, increasing systematically with decreasing L.

Values of the average energy for the high-energy electrons and ions are listed in Tables 11 and 12 for representative values of KP, L, and LT. The standard deviations for the averages are less than 100 percent of the values for electrons and less than 20 percent for protons. The tables show that the average energies remain nearly constant with increasing magnetic activity. In fact, there may even be a decrease in average energy with increased KP for high-energy ions in the dawn sector.

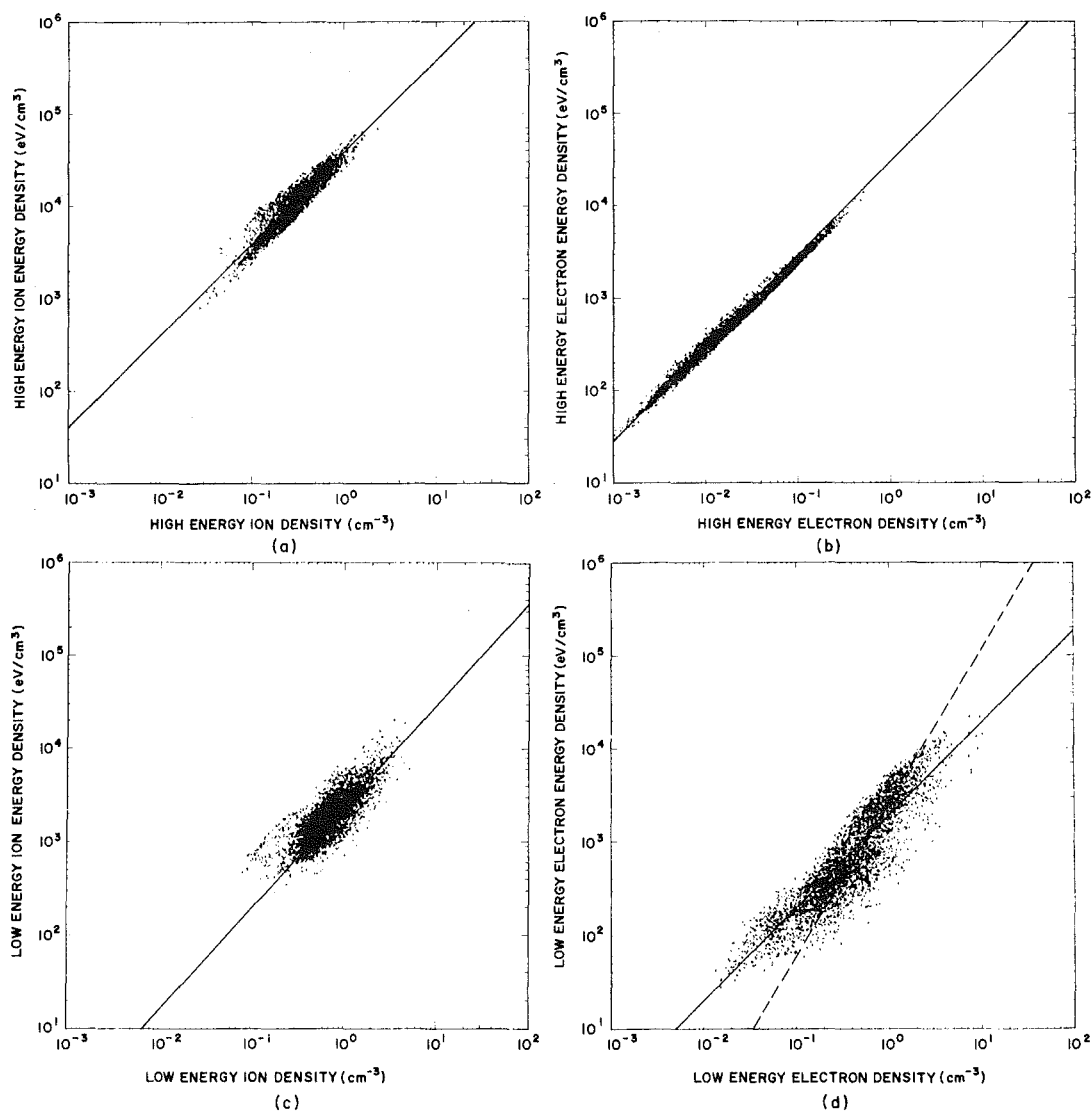


Figure 19. Scatter Plots of Energy Density vs Number Density for (a) High-energy Ions, (b) High-energy Electrons, (c) Low-energy Ions, and (d) Low-energy Electrons

The major variation in average energy for the low-energy components, apparent in Figure 20(c) and 20(d), is in LT. For ions, the average energy maximizes (minimizes) in the dusk-to-midnight (dawn-to-noon) sector. While not as clear a variation, the electron average energy maximizes (minimizes) in the midnight-to-dawn (noon-to-dusk) sector.

AVERAGE ENERGY (ED/N) Kp2,3

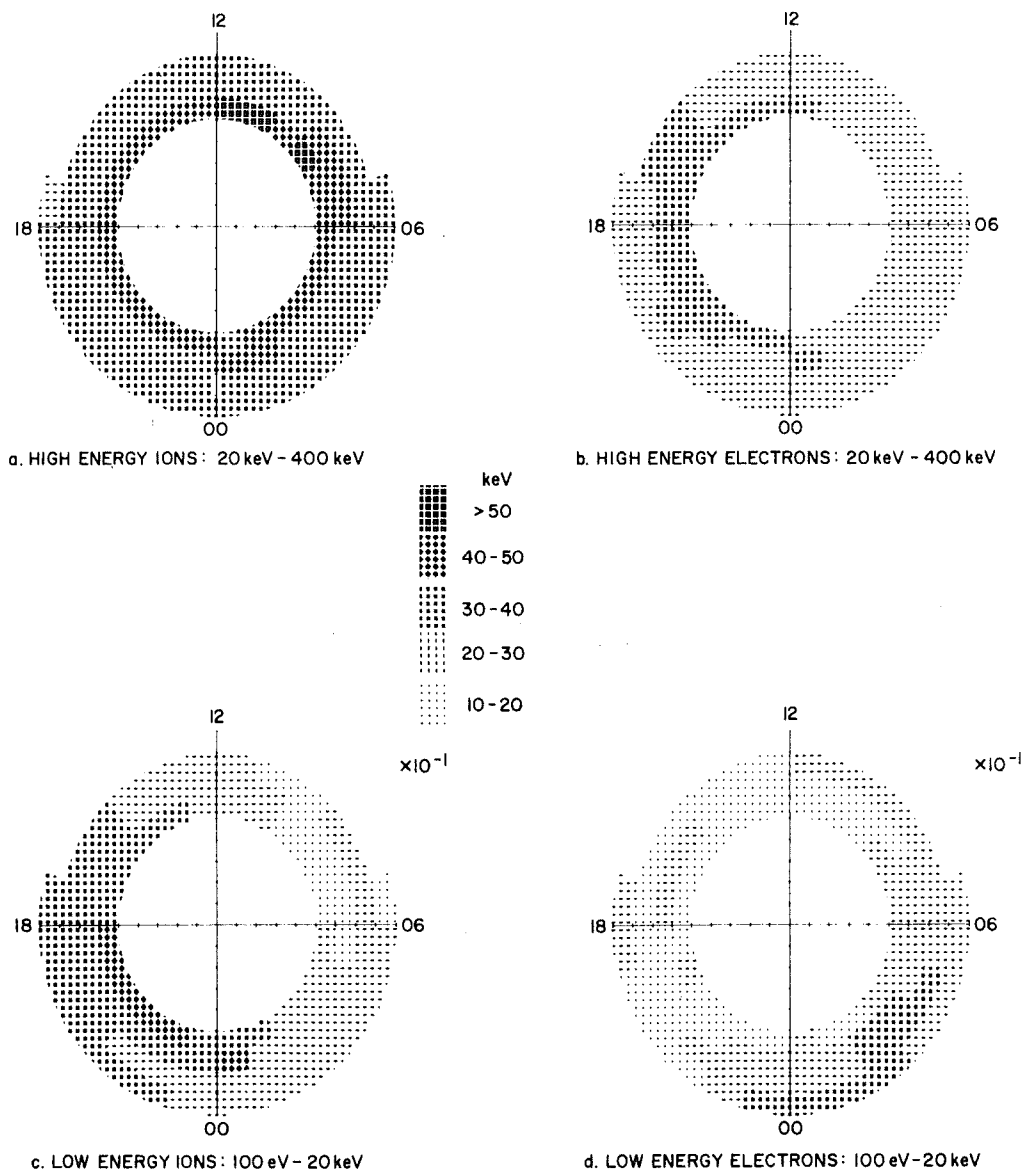


Figure 20. Variations in Average Energy Coded in Polar Coordinate LT and L-shell Ranges. The average energies are for (a) high-energy ions, (b) high-energy electrons, (c) low-energy ions, and (d) low-energy electrons. The code is in the center in keV and values in (c) and (d) must be multiplied by 10^{-1}

Table 11. Electron High-energy Average Energy (keV) for KP Levels 2, 3 (4, 5)

	LT			
	2300-0100	0500-0700	1100-1300	1700-1900
L-shell (R_E)				
5.5 - 6	30.0 (28.0)	27.0 (27.0)	31.0 (31.0)	32.0 (35.0)
6 - 7	29.0 (25.0)	27.0 (26.0)	30.0 (30.0)	33.0 (34.0)
7 - 8	26.0 (26.0)	25.0 (25.0)	29.0 (29.0)	30.0 (29.0)
8 - 8.5	24.0 (25.0)	24.0 (24.0)		27.0 (26.0)

Table 12. Ion High-energy Average Energy (keV) for KP Levels 2, 3 (4, 5)

	LT			
	2300-0100	0500-0700	1100-1300	1700-1900
L-shell (R_E)				
5.5 - 6	41.0 (35.0)	47.0 (38.0)	50.0 (45.0)	45.0 (42.0)
6 - 7	39.0 (31.0)	41.0 (34.0)	39.0 (38.0)	38.0 (38.0)
7 - 8	34.0 (37.0)	33.0 (30.0)	35.0 (35.0)	32.0 (34.0)
8 - 8.5	33.0 (35.0)	31.0 (31.0)		30.0 (36.0)

Tables 13 and 14 give average values of the average energy for representative values of KP, L-shell, and LT. The standard deviations can be as much as 50 percent of the total for both ions and electrons, but are generally considerably lower. A systematic increase (decrease) in electron (ion) average energy occurs in the midnight sector with increasing magnetic activity. (Actually, this variation is more apparent between KP ranges 0, 1 and 2, 3. The 2300 to 0100 LT average energy for electrons for the KP range 0, 1 as a function of increasing L is 1.2, 1.3, 1.5, and 1.6 keV. For ions it is 4.1, 3.5, 3.2, and 3.1 keV.)

Here, we note that if the high- and low-energy populations were truly Maxwellian, temperatures could be recovered by using the equation

$$kT = 2/3 E_{AV} \quad , \quad (12)$$

and making a density dependent error function correction to E_{AV} . (This is necessary since E_{AV} is computed over a partial energy range.)

Table 13. Electron Low-energy Average Energy (keV) for KP Levels 2, 3 (4, 5)

	LT			
	2300-0100	0500-0700	1100-1300	1700-1900
L-shell (R_E)				
5.5 - 6	1.9 (2.2)	2.5 (3.4)	1.8 (1.7)	1.6 (1.5)
6 - 7	2.1 (2.2)	2.4 (2.9)	1.8 (2.1)	2.0 (1.4)
7 - 8	2.9 (3.0)	2.6 (2.5)	1.9 (2.5)	1.5 (2.0)
8 - 8.5	3.4 (3.7)	2.8 (2.5)		2.3 (2.7)

Table 14. Ion Low-energy Average Energy (keV) for KP Levels 2, 3 (4, 5)

	LT			
	2300-0100	0500-0700	1100-1300	1700-1900
L-shell (R_E)				
5.5 - 6	3.6 (3.0)	2.0 (2.3)	2.4 (2.0)	3.8 (4.0)
6 - 7	3.7 (3.1)	1.9 (2.2)	2.3 (2.4)	3.8 (3.9)
7 - 8	2.7 (2.6)	2.3 (2.8)	2.2 (2.4)	3.8 (3.4)
8 - 8.5	2.5 (2.2)	2.2 (2.0)		3.1 (2.5)

4.4.2.4 Number Flux

The omnidirectional number flux and energy flux show average variations with L-shell, LT, and magnetic activity level that are very similar to those of the energy density. (See Figures 13 through 15.) In each case the electron fluxes are greater than the ion fluxes by more than an order of magnitude. This is due to the factor of $m^{-1/2}$ in the flux moment calculations that is not present in those for number and energy density.

Table 15 gives the total electron number flux averaged over the designated LT, L-shell, and KP ranges. Two points are evident in the table that can also be

Table 15. Total Electron Number Flux ($\times 10^9$) ($\text{cm}^2 \text{sec}^{-1}$) for KP Levels 2, 3 (4, 5)

	LT			
	2300-0100	0500-0700	1100-1300	1700-1900
L-shell (R_E)				
5.5 - 6	2.0 (5.7)	1.7 (3.8)	0.70 (1.2)	0.43 (0.78)
6 - 7	3.7 (7.8)	2.2 (4.3)	0.58 (0.79)	0.31 (0.53)
7 - 8	3.3 (5.3)	2.2 (4.0)	0.56 (0.46)	0.39 (1.4)
8 - 8.5	3.1 (2.9)	1.8 (2.3)		0.36 (1.1)

seen in Figure 13. First, the electron number fluxes are significantly higher in the midnight and dawn regions than those in the noon and evening regions. Second, the electron number fluxes increase substantially with KP.

Tables 16, 17, and 18, give percentages of the total electron flux for the high-energy (20 to 400 keV) electron number flux, high-energy ion number flux and low-energy (100 eV to 20 keV) ion number flux, respectively. The tables cover the same time, distance, and activity ranges as Table 15. Clearly, the percentage of low-energy electrons can also be obtained from Table 16. The high-energy electron flux is 10 - 30 percent of the total electron flux for KP levels ≥ 2 - and ≤ 5 +. The percentage is highest near noon, but increases with KP only near midnight. The percentages of high- and low-energy ions (Tables 17 and 18) maximize near dusk and tend to decrease with increasing magnetic activity in the midnight and dawn regions. It should be noted that on the average the high-energy ions can contribute up to seven times more flux than the low-energy ions.

Table 16. Percentage High-energy Electron Number Flux of Total Electron Number Flux for KP Levels 2, 3 (4, 5)

	LT			
	2300-0100	0500-0700	1100-1300	1700-1900
L-shell (R_E)				
5.5 - 6	18.0 (19.0)	24.0 (23.0)	28.0 (25.0)	31.0 (14.0)
6 - 7	9.0 (17.0)	21.0 (24.0)	23.0 (25.0)	19.0 (12.0)
7 - 8	16.0 (24.0)	17.0 (15.0)	18.0 (28.0)	16.0 (7.0)
8 - 8.5	18.0 (23.0)	14.0 (17.0)		14.0 (15.0)

Table 17. Percentage High-energy Ion Number Flux of Total Electron Number Flux for KP Levels 2, 3 (4, 5)

	LT			
	2300-0100	0500-0700	1100-1300	1700-1900
L-shell (R_E)				
5.5 - 6	7.5 (3.2)	5.9 (3.3)	37.0 (12.0)	29.0 (26.0)
6 - 7	4.2 (2.0)	2.8 (1.7)	14.0 (11.0)	35.0 (35.0)
7 - 8	2.9 (2.0)	2.0 (1.4)	9.3 (12.0)	22.0 (6.9)
8 - 8.5	2.4 (2.6)	1.2 (0.7)		16.0 (3.3)

Table 18. Percentage Low-energy Ion Number Flux of Total Electron Number Flux for KP Levels 2, 3 (4, 5)

	LT			
	2300-0100	0500-0700	1100-1300	1700-1900
L-shell (R_E)				
5.5 - 6	3.5 (12.0)	3.2 (2.8)	5.3 (3.1)	13.0 (7.8)
6 - 7	2.2 (1.6)	2.3 (2.4)	6.3 (5.4)	13.0 (10.0)
7 - 8	1.9 (1.6)	1.9 (1.8)	5.9 (6.5)	11.0 (3.1)
8 - 8.5	1.8 (1.7)	1.7 (1.4)		8.9 (2.0)

Scatter plots of the data (every 20th point is plotted) are given in Figures 21 and 22. In Figure 21 the number fluxes for the high- and low-electron populations are each plotted against the total electron flux. Figure 21(a) shows that the low-energy electron flux is highly correlated with the total flux. This is primarily because it constitutes most of the electron number flux. The upper bound of the low-energy flux approaches 100 percent of the total (straight line is one-to-one correlation). The total flux ranges from 6×10^7 - 2.5×10^{10} ($\text{cm}^2 \text{sec}^{-1}$). However, there are extremely few cases for which the total electron flux is greater than 10^{10} ($\text{cm}^2 \text{sec}^{-1}$) and none where the flux reaches 3×10^{10} ($\text{cm}^2 \text{sec}^{-1}$). The lower bound of the total electron flux is 4×10^7 ($\text{cm}^2 \text{sec}^{-1}$). The high-energy electron number flux [Figure 21(b)] varies over an equally wide range but is about an order of magnitude smaller in value than the total electron flux. It ranges

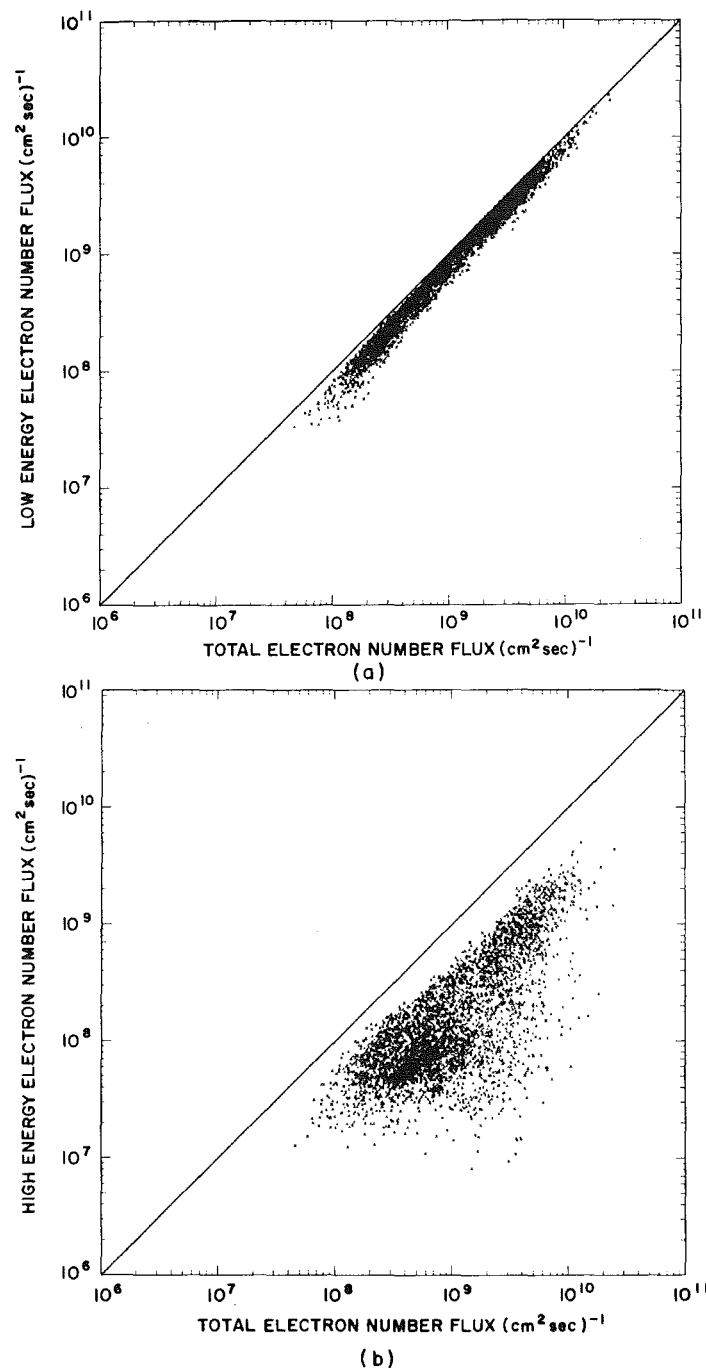


Figure 21. Scatter Plots of (a) Low-energy and (b) High-energy Electron Number Flux vs Total Electron Number Flux. The 45° straight lines signify equality. The fluxes were obtained from the first moment over the appropriate energy range

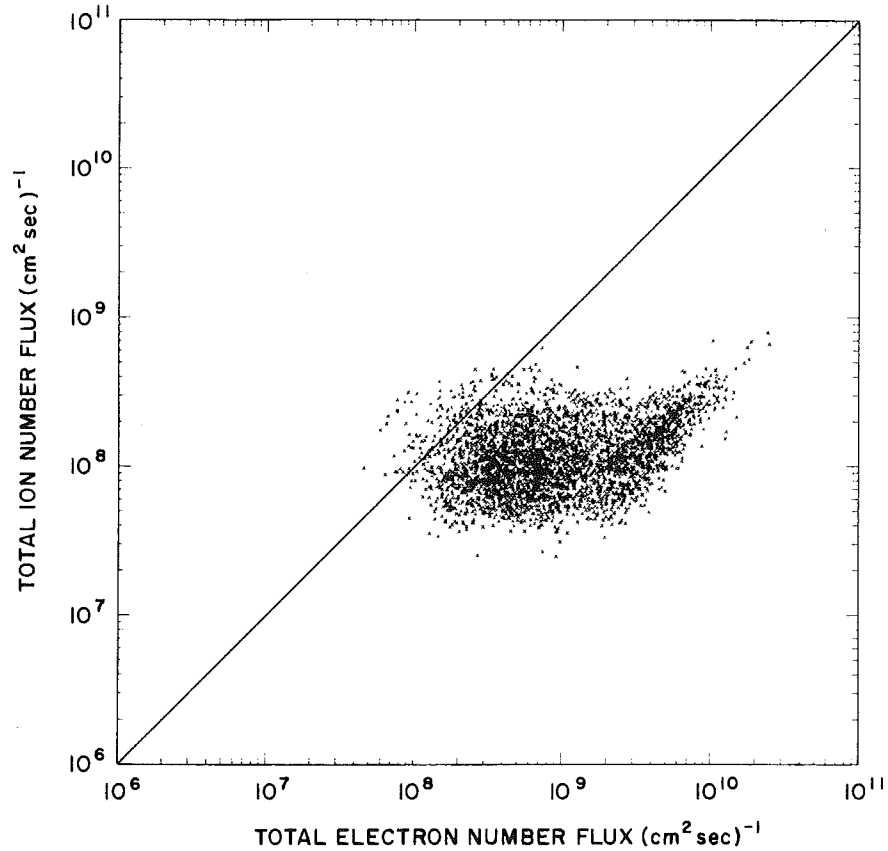


Figure 22. Scatter Plot of Total Ion Number Flux vs Total Electron Number Flux. The 45° straight line signifies equality. The fluxes were obtained from the first moments

$8 \times 10^6 - 5 \times 10^9 \text{ (cm}^2\text{sec)}^{-1}$. In addition, the values do not correlate well with the total flux. But, they appear to have a well-defined upper bound significantly less than 100 percent (straight line). The upper bound is ~ 65 percent of the total at low total flux values, and ~ 40 percent of the total at high values.

Figure 22 is the scatter plot of the total ion number flux vs the total electron number flux. Again the straight line shows where they are equal. There is a small percentage of cases at the low end of the electron flux range for which the ion flux exceeds the electron flux. The overall range of the ion flux is considerably smaller than the electron range, approximately 1.5 orders of magnitude from 2.5×10^7 to $8 \times 10^8 \text{ (cm}^2\text{sec)}^{-1}$. For high values of the total electron flux [values greater than $2 \times 10^9 \text{ (cm}^2\text{sec)}^{-1}$] there is a lower bound on the ion flux that increases with increasing total electron flux. It starts at approximately

0.1 percent at $2 \times 10^9 \text{ (cm}^2\text{sec)}^{-1}$ and goes to approximately 2.5 percent at $2 \times 10^{10} \text{ (cm}^2\text{sec)}^{-1}$. The number fluxes are critical to spacecraft charging model calculations and will be highlighted in the discussion at the end of the section.

4.4.3 PITCH ANGLE ANISOTROPIES

The SC5 data were used to determine the anisotropy of the electron fluxes between ~ 100 and 400 eV and the ion fluxes between 4 and 400 keV. The lower-energy ion fluxes were not used because noise rejection criteria in generating the data base reduced the data base below a statistically significant sample level. The data base consists of ten minute averages of anisotropy indices (AIs) of the form used by Kaye et al,¹⁷ but modified slightly to range from -1 to +1.

The data base was set up in several steps. First, a single AI was determined for each ion and electron energy channel once per spin. The index was

$$AI = \frac{F_{90}}{F_{45}} - 1 \quad \text{for } F_{45} > F_{90} \quad (13)$$

$$AI = - \left(\frac{F_{45}}{F_{90}} - 1 \right) \quad \text{for } F_{90} \geq F_{45} \quad ; \quad (14)$$

where AI is the anisotropy index, F_{90} is the flux measured perpendicular to the magnetic field in $\text{part/cm}^2\text{-sec-sr-eV}$, and F_{45} is the flux measured 45° to the magnetic field in $\text{part/cm}^2\text{-sec-sr-eV}$. The 90° and 45° measurements used were the first ones encountered during the spin (the spin starts at a minimum pitch angle) unless one of the points was missing due to sun pulse rejection mentioned earlier. In that case, the second set was used. The high and low points within a 10-min LT interval were discarded and if three or more points remained, they were averaged to get one 10-min average data base point. All the data bases except the low-energy ions contained 10000 - 14000 10-min averages. The low-energy ion data bases contained only approximately 3000 data points. The flux at 45° was used instead of 40° or less to maximize the size of the data base. Also, sample runs of AIs at both 40° and 45° showed only very small differences (< 0.02) in the indices for the two angles.

The nomenclature used by West¹⁸ will be used in referring to pitch angle distributions of the individual flux channels. Three types will be identified

17. Kaye, S.M., Lin, C.S., Parks, G.K., and Winckler, J.R. (1978) Adiabatic modulation of equatorial pitch angle anisotropy, J. Geophys. Res. 83:2675.
18. West, H.I., Jr. (1979) The signatures of the various regions of the outer magnetosphere in the pitch angle distributions of energetic particles in Quantitative Modeling of Magnetospheric Processes, W.P. Olson, Ed., American Geophysical Union, Washington, D.C., p. 150.

depending on whether the AI is positive, negative, or near zero. A positive AI will represent a normal distribution since the distribution is peaked near 90° and would appear as a normal frequency distribution if plotted as flux vs pitch angle in Cartesian coordinates. A negative AI will represent a butterfly distribution since it would appear as a butterfly on a polar plot of flux vs pitch angle. And, an AI near zero will represent an isotropic distribution although it does not necessarily mean that the loss cone is filled with precipitating particles. In general, we take the tendency toward isotropy and away from normal distributions to indicate the presence of disturbances or interactions that scatter particles to lower pitch angles. Since we do not include any loss cone information in the AI, care must be taken in interpreting the results.

The indices for both ions and electrons were first statistically averaged over 0.5 L-shell bins and 3-h LT bins for all KP. Four 3-h LT bins between 0600 and 1800 were then averaged to get a dayside value. Likewise, four 3-h LT bins between 1800 and 0600 were averaged to get a nightside value. The two 3-h periods around local noon (0900 to 1500) and local midnight (2100 to 0300) were also averaged. The results for representative energy channels are given in Tables 19 and 20 for electrons and ions, respectively. The numbers in parentheses are for noon and midnight.

Table 19. Electron Anisotropy Indices (All KP)

Energy (keV)	L-shell	AI	
		Day	Night
0.11	5.5-6.0	0.39 (0.43)	0.21 (0.19)
	6.0-6.5	0.37 (0.43)	0.13 (0.12)
	6.5-7.0	0.35 (0.40)	0.11 (0.07)
	7.0-7.5	0.26 (0.29)	0.10 (0.00)
	7.5-8.0	0.18 (0.16)	0.03 (-0.06)
1.5	5.5-6.0	0.48 (0.52)	0.29 (0.27)
	6.0-6.5	0.43 (0.48)	0.20 (0.20)
	6.5-7.0	0.38 (0.40)	0.15 (0.11)
	7.0-7.5	0.29 (0.32)	0.11 (0.05)
	7.5-8.0	0.22 (0.25)	0.07 (0.04)
9.0	5.5-6.0	0.35 (0.35)	0.30 (0.28)
	6.0-6.5	0.34 (0.34)	0.20 (0.19)
	6.5-7.0	0.33 (0.36)	0.17 (0.14)
	7.0-7.5	0.29 (0.33)	0.15 (0.10)
	7.5-8.0	0.28 (0.36)	0.10 (0.06)
96.0	5.5-6.0	0.30 (0.33)	0.15 (0.12)
	6.0-6.5	0.29 (0.34)	0.07 (0.05)
	6.5-7.0	0.28 (0.33)	0.03 (-0.02)
	7.0-7.5	0.27 (0.38)	-0.02 (-0.06)
	7.5-8.0	0.21 (0.37)	-0.15 (-0.12)

Table 20. Ion Anisotropy Indices (All KP)

Energy (keV)	L-shell	AI	
		Day	Night
4.0	5.5-6.0	0.18 (0.22)	0.04 (0.01)
	6.0-6.5	0.17 (0.20)	0.01 (-0.02)
	6.5-7.0	0.15 (0.20)	0.02 (0.00)
	7.0-7.5	0.12 (0.18)	0.03 (0.00)
	7.5-8.0	0.16 (0.19)	0.01 (-0.03)
10.0	5.5-6.0	0.15 (0.15)	0.10 (0.10)
	6.0-6.5	0.18 (0.19)	0.08 (0.08)
	6.5-7.0	0.19 (0.21)	0.08 (0.05)
	7.0-7.5	0.16 (0.18)	0.09 (0.06)
	7.5-8.0	0.19 (0.18)	0.10 (0.06)
55.0	5.5-6.0	0.34 (0.35)	0.35 (0.34)
	6.0-6.5	0.37 (0.42)	0.18 (0.18)
	6.5-7.0	0.38 (0.47)	0.14 (0.08)
	7.0-7.5	0.44 (0.54)	0.08 (0.03)
	7.5-8.0	0.42 (0.52)	0.06 (0.02)
126.0	5.5-6.0	0.50 (0.55)	0.26 (0.21)
	6.0-6.5	0.52 (0.58)	0.07 (0.07)
	6.5-7.0	0.48 (0.59)	0.01 (-0.08)
	7.0-7.5	0.53 (0.68)	-0.06 (-0.15)
	7.5-8.0	0.51 (0.66)	0.00 (-0.08)

The electron values in Table 19 show several patterns. The day indices are always higher than the night indices for all L-shells. This suggests that for electrons in the energy range 100 eV to 400 keV most interactions that cause pitch angle scattering away from a more normal distribution toward a more isotropic distribution occur on the nightside of the magnetosphere where injection events occur. The data also show that the midnight region, in most cases, has more isotropic distributions than the total nightside region. The table also shows there is a trend away from a normal distribution with increasing L-shell indicating more disturbance regions farther out. This is most likely due to the fact that substorms start at higher L-shells and move inward. The distance they move in depends on the intensity of the storm. Therefore, higher L-shells see weaker storms as well as the stronger storms, thus keeping those regions in more disturbed (more particle scattering) states. The electrons over the whole energy range behave in a similar manner although the absolute AI levels vary somewhat with energy.

The ion behavior, on the other hand, is somewhat different as can be seen in Table 20. The degree of anisotropy in the day region seems to be near constant for a particular energy range independent of L-shell. The degree of anisotropy

increases systematically with energy. In the night region the near constancy of AI with L holds for the lower two energies, while a dropoff in AI with L is evident for the higher energies. The day values for ions as in the case for electrons are higher than the night values indicating that the most dynamical behavior occurs in the midnight region. Except for the innermost L-ranges at the higher energies, the spectra are near isotropic in the night region.

Tables 21 and 22 give the day and night AIs averaged between L equals 6 to 8 R_E as a function of KP for electrons and ions, respectively. The electron AIs show no significant change in the day sector and a decrease with increasing KP in the night sector. The ions show no consistent pattern day or night with KP.

Table 21. Electron Anisotropy Indices (L = 6 to 8)

Energy (keV)	KP	AI	
		Day	Night
0.11	0, 1	0.32 (0.33)	0.21 (0.14)
	2, 3	0.32 (0.35)	0.09 (0.04)
	4, 5	0.22 (0.28)	-0.04 (-0.06)
1.5	0, 1	0.34 (0.34)	0.27 (0.23)
	2, 3	0.34 (0.39)	0.14 (0.14)
	4, 5	0.29 (0.32)	0.03 (0.01)
9.0	0, 1	0.34 (0.37)	0.20 (0.18)
	2, 3	0.32 (0.36)	0.18 (0.16)
	4, 5	0.25 (0.27)	0.09 (0.08)
96.0	0, 1	0.27 (0.34)	0.01 (-0.04)
	2, 3	0.26 (0.35)	-0.03 (-0.06)
	4, 5	0.23 (0.35)	-0.12 (-0.15)

The AIs averaged over all KP are given in Figure 23 for (a) 9-keV electrons, (b) 96-keV electrons, (c) 10-keV ions, and (d) 126-keV ions. The plots are in polar coordinates of LT and L-shell. The codes on the plots reflect ranges of the AIs that are identified in the middle of the plot. Those regions with slashes are regions where the pitch angle distributions are either butterfly or represent regions where coning or streaming along field lines is taking place. The two lower-energy plots are seen to be well-represented in the dawn, evening, noon, and midnight quadrants by their table averages. The higher (~ 100 keV) energy plots provide some additional information on regions of high-energy particle access to the near-geosynchronous region of space.

Table 22. Ion Anisotropy Indices (L = 6 to 8)

Energy (keV)	KP	AI	
		Day	Night
4.0	0, 1	0.19 (0.22)	0.04 (-0.02)
	2, 3	0.15 (0.19)	0.03 (0.00)
	4, 5	0.11 (0.17)	-0.02 (-0.01)
10.0	0, 1	0.12 (0.15)	0.17 (0.16)
	2, 3	0.19 (0.21)	0.09 (0.07)
	4, 5	0.20 (0.23)	0.01 (0.00)
55.0	0, 1	0.44 (0.50)	0.20 (0.16)
	2, 3	0.39 (0.49)	0.08 (0.05)
	4, 5	0.40 (0.44)	0.08 (0.05)
126.0	0, 1	0.52 (0.61)	0.06 (-0.01)
	2, 3	0.52 (0.63)	0.06 (-0.17)
	4, 5	0.46 (0.56)	0.01 (0.00)

Using the particle trajectory program described in Section 3, the high-energy electrons were traced back in time from different LT and radial distances from the SCATHA orbit. The ~ 100 -keV electrons, unless on trapped circular orbits, enter the magnetosphere and turn eastward in the regions designated as having butterfly distributions (slashed regions) on Figure 23(b); that is, in the pre-midnight region. Similarly the high-energy ion access region to the SCATHA orbit as determined by particle tracing is the postmidnight region. The ions enter in an eastward direction and then turn westward. For both ions and electrons day-side particles are primarily on trapped orbits. To a first order the butterfly type distribution regions in the high-energy anisotropy plots in Figure 23 reflect processes due to particle entry at geosynchronous orbits. More work must be done using measured magnetic moments and more accurate field models for higher activity levels before the plots can be fully explained.

4.5 Discussion

The middle-energy particle populations have been identified as the determinants of spacecraft charging at geosynchronous altitudes. Generally speaking, most spacecraft in near-geosynchronous environments while in sunlight can emit, through photoionization, a much greater electron current than they intercept from the environment. Thus, satellite charging is directed toward impeding the loss of photoelectrons, and positive satellite potentials of a few eV can cause acceleration of sufficient numbers of electrons to the vehicle to cause current balance. However, when a satellite is in darkness (eclipse) and/or sufficient high energy

ANISOTROPY INDICES

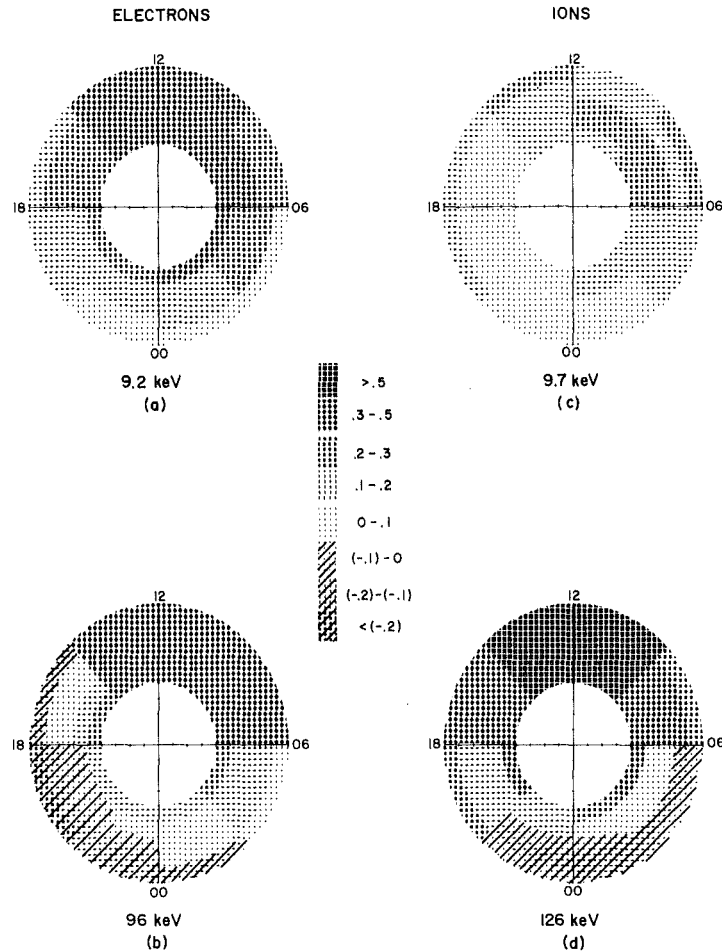


Figure 23. Anisotropy Indices Averaged Over All KP and Plotted in Polar Coordinate Representations of LT and L-shell for (a) 9-keV Electrons, (b) 96-keV Electrons, (c) 10-keV Ions, and (d) 126-keV Ions. The codes represent ranges of the indices and are identified in the center of the figure

electron fluxes impinge on the vehicle, the middle-energy environmental currents and their interactions with the vehicle dominate the charging process.

Since spacecraft charging results from current imbalance at the satellite surface, any empirical model of the charging process requires knowledge of the ambient currents (number fluxes) for all components of the plasma. In addition, one must know the backscattered and secondary emission properties of the

spacecraft surface for each plasma component. These depend on both the magnitude of the incident current and on the energy of the incident particles. The latter dependence has been the principal reason for presenting the middle-energy particle data in two energy ranges, ~ 100 eV to 20 keV and 20 to 400 keV. The high-energy electron number fluxes have been found to be directly proportional to the charging level for the most severe SCATHA sunlight charging periods (Mullen and Gussenhoven).¹⁹ This is most probably due to the energy dependence of back-scattered and secondary emission properties of the satellite materials. Laframboise et al²⁰ have shown that for Maxwellian electron distributions the backscattered and secondary electron current from a material surface exactly balance the incident electron current at a given temperature (average energy) level, called the threshold temperature for that material. For typical satellite materials the threshold temperature is 0.5 to 5 keV. For a single Maxwellian the balance is obtained independent of the magnitude of the number flux. Thus, although the low-energy electrons have the highest number fluxes, it is possible that they contribute little to spacecraft charging because of their self-balancing interaction with the spacecraft. The ion number fluxes, although less than the electron number fluxes by more than an order of magnitude, must also be considered in producing charging as well as maintaining current balance since they can cause large ion-induced secondary electron emissions.

As an example of the levels and percentages of the high and low, electron and ion number fluxes seen during high-level spacecraft charging events on SCATHA, flux values are given, for the three spacecraft charging case studies reported by Mullen and Gussenhoven.¹⁹ The three charging events occurred on days 114, 241, and 363, 1979. Table 23 gives the number flux percentages of the total electron number flux for high and low, electron and ion particle populations. The total electron number fluxes for these periods are also included. It is quite evident from Table 23 that the total electron number flux is significantly higher than the average values in the midnight region given earlier in Table 17. Another significant variation from the average values is the very high percentage of high-energy electrons, approximately 50 percent. While the percentage could be raised by a decrease in the total electron flux due to the repulsion of low-energy electrons by the negatively-charged satellite, it is quite clear that the actual high-energy electron current is greatly enhanced over average values. It should also be noted that

19. Mullen, E.G., and Gussenhoven, M.S. (1982) High Level Spacecraft Charging Environments Near Geosynchronous Orbit, AFGL-TR-82-0063, AD A118791.

20. Laframboise, J.G., Godard, R., and Kamitsuma, M. (1982) Multiple floating potentials, "threshold-temperature" effects and "barrier" effects in high-voltage charging of exposed surfaces on spacecraft, in Proceedings International Symposium on Spacecraft Materials in Space Environment, Toulouse, France, 8-11 June 1982 (to be published).

Table 23. Population Percentages of Total Electron Number Flux for Three High-level Charging Days

	Day		
	114	241	363
KP	3+	7-	5
Total electron number flux $\times 10^9 \text{ (cm}^2 \text{ sec)}^{-1}$	4.3	13.0	10.0
% Low-energy electrons	44.0	62.0	53.0
% High-energy electrons	56.0	38.0	47.0
% Low-energy ions	2.5	1.5	2.4
% High-energy ions	1.7	1.5	1.4

Table 23 shows quite low percentages of ion fluxes in spite of the fact that low-energy ions are attracted to the satellite.

In summary, the middle-energy currents and particle populations are very dynamic, changing in their characteristic behavior with energy, magnetic activity, L-shell, and LT. Some of the results such as seeing more disturbed environments near midnight were to be expected. Other results such as the large (up to 50 percent) contribution of the electrons to the total particle pressure were not anticipated. The particle pressures from SC5 will also be used to determine the plasma β 's (ratios of particle pressure to magnetic field pressure) in Section 6. The tables and plots of the particle results should provide a useful data base for modelers and theoreticians alike who have a need to better understand the near-geosynchronous plasma regime.

5. SC8 ION COMPOSITION RESULTS

The 0.1- to 32-keV ion composition experiment known as SC8 was built and operated under the direction of Dr. R. G. Johnson of the Lockheed Palo Alto Research Laboratory. Only measurements of two species, singly ionized hydrogen and oxygen, will be discussed in this section.

5.1 Introduction

Measurements of ion composition in the magnetosphere reveal the source(s) of magnetospheric particles and, in addition, can indicate the dynamical processes that transport the ions from their source. In the simplest view there are two

sources, the topside ionosphere, which is rich in O^+ and the solar wind, which has a He^+ content of ~ 4 percent. Both are sources of H^+ , which has generally been considered to be the major ion component throughout the magnetosphere at all times. Since the ionosphere also is a source for He^+ , researchers have looked at less abundant species such as He^{++} , O^{++} , and the ratios of the abundance of the various components to provide more continuing evidence for source identification, (see reviews by Shelley,²¹ Johnson,²² and Geiss et al²³).

One of the more surprising results to come from recent studies was the discovery that the oxygen abundance in the plasma sheet could equal and even exceed the proton abundance. This occurs principally during periods of high magnetic activity (Peterson et al²⁴ and Lennartsson et al²⁵). This discovery has effectively reversed the relative importance of the roles of the solar wind and the ionosphere as sources for the equatorial magnetosphere and possibly even as sources for the high-latitude region, the tail lobes (Sharp et al²⁶).

A statistical analysis of the H^+ and O^+ data from the SC8 ion composition was performed. The results of the analysis together with short discussions on the instrumentation and data base are given below. In addition, in Appendix B the SC8 data is used to correct ion data results from SC5, which measured ions without mass discrimination.

5.2 Instrumentation

The Lockheed Energetic Ion Composition Experiment, SC8, measures ions with energies per unit charge (keV/q) from 100 eV/q to 32 keV/q in 24 logarithmically-spaced energy steps and with masses 1 to 160 AMU. The instrument consists of three ion mass spectrometer heads (CXAs), each consisting of a Wien velocity filter in series with an electrostatic analyzer and a channel electron multiplier sensor. The detector characteristics are summarized in Table 24

-
21. Shelley, E.G. (1979) Heavy ions in the magnetosphere, Space Sci. Rev. 23:465.
 22. Johnson, R.G. (1979) Energetic ion composition in the earth's magnetosphere, Rev. Geophys. Space Phys. 17:696.
 23. Geiss, J., Balsiger, H., Eberhardt, P., Walker, H.P., Weber, L., and Young, D.T. (1978) Dynamics of magnetospheric ion composition as observed by the GEOS mass spectrometer, Space Sci. Rev. 22:537.
 24. Peterson, W.K., Sharp, R.D., Shelley, E.G., Johnson, R.G. (1981) Energetic ion composition of the plasma sheet, J. Geophys. Res. 86:761.
 25. Lennartsson, W., Sharp, R.D., Shelley, E.G., Johnson, R.G., and Balsiger, H. (1981) Ion composition and energy distribution during 10 magnetic storms, J. Geophys. Res. 86:4628.
 26. Sharp, R.D., Carr, D.L., Peterson, W.K., and Shelley, E.G. (1981) Ion streams in the magnetotail, J. Geophys. Res. 86:4639.

Table 24. SC8 Ion Detector Characteristics

Detector	Particle	Energy-per-unit Charge (keV/q)
CXA 1	ions	0.10, 0.13, 0.17, 0.21, 0.27, 0.35, 0.45, 0.58
CXA 2	ions	0.75, 0.96, 1.23, 1.58, 2.03, 2.61, 3.35, 4.30
CXA 3	ions	5.5, 7.1, 9.1, 11.7, 15.1, 19.4, 24.9, 32.0

which is taken from Kaye et al.²⁷ Each detector measures in eight energy-per-unit charge steps and has a resolution of 5° FWHM. The instrument operates in two modes. One mode (sweep mode) sweeps in mass per unit charge, acquiring a full mass (32 points) and energy (24 points) spectrum every 16 sec. The other mode (locked mode) samples one particular mass and obtains a complete (24 points) energy spectra every 1/2 sec. In normal operation the detectors alternate between a sweep and a lock mode every 64 sec. Background samples are periodically taken over the whole mass range. A complete description of the instrument is given in Stevens and Vampola¹ and Kaye et al.²⁷

5.3 Data Base

The data used in this study are 1-h averages of differential energy fluxes for mass 1 (H^+) and mass 16 (O^+) in each of the 24 different energy steps listed in Table 24. The data were provided on magnetic tape by Dr. R.G. Johnson of Lockheed. The fluxes were provided in units of $keV/cm^2\text{-sec-sr-keV}$. The data include both negative and positive values due to background subtractions, and the negative values were included in the statistical calculations. No pitch angle discrimination was made in the data set, and a 1-h average consists of the total data available in that 1-h time span. For these reasons it is impossible to estimate the error introduced by assuming isotropy as we do in the calculations below.

In the following we will refer to each hourly average of the differential energy flux for a given central energy as one data point. The data points for a sample day, 11 February, 1979 (day 42), are displayed in Figure 24 by energy channel and by UT. This day is chosen not to represent typical oxygen and hydrogen flux variations (these have not yet been established), but to show types of variations in the data points that are commonly encountered. A discussion of the events on this

27. Kaye, S.M., Johnson, R.G., Sharp, R.D., and Shelley, E.G. (1981a)
Observations of transient H^+ and O^+ bursts in the equatorial magnetosphere,
J. Geophys. Res. 86:1335.

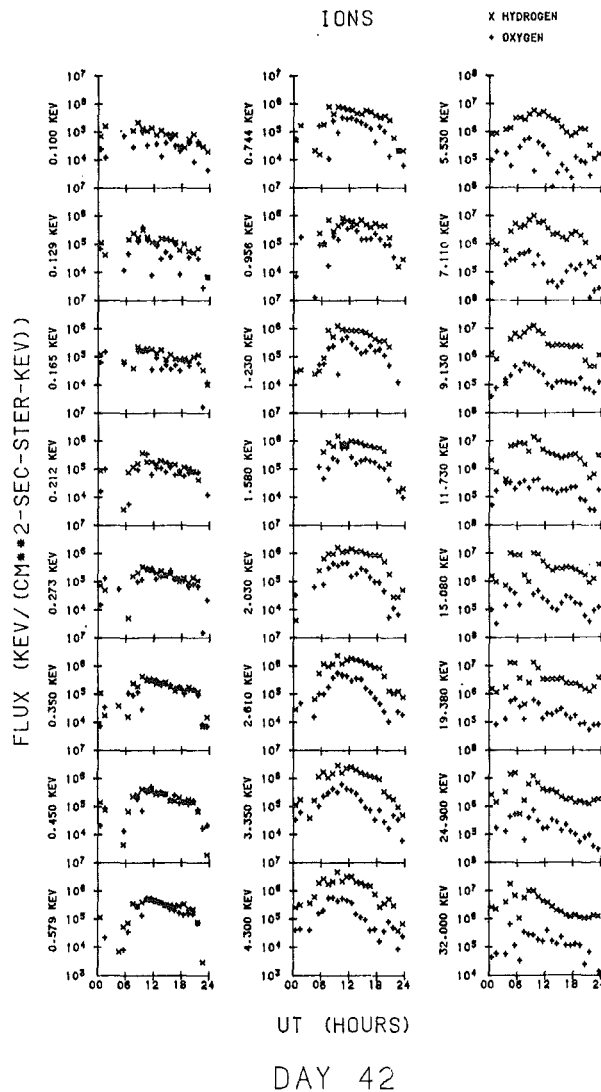


Figure 24. Hourly Averages of SC8 O^+ (+) and H^+ (x) Differential Energy Fluxes for the 24 SC8 Energy Channels on Day 42, 1979. Missing data points indicate values are below the lower plotting limits

day has been given by Moore et al.²⁸ They identify a stationary plasma sheet crossing from ATS and SCATHA electron data at ~ 0700 UT. They further identify a dynamic injection event between 0900 to 1000 UT. Prior to the plasma sheet

28. Moore, T.E., Arnoldy, R.L., Feynman, J., and Hardy, D.A. (1981) Propagating substorm injection fronts, J. Geophys. Res. 86:6713.

crossing both O^+ and H^+ fluxes in all but the highest-energy channels are severely depressed, falling below background levels.

The data base consists of 1597 data points for each energy channel and for each species, taken over 72 days that are listed in Table 25.

Table 25. Days From 1979 in SC8 Data Base

42	87	113	126	158	210
43	88	114	128	164	212
44	89	115	129	167	216
45	93	116	138	168	218
46	94	117	141	178	225
47	95	118	145	180	226
52	103	119	146	188	227
53	104	120	149	194	230
59	108	122	150	200	232
77	110	123	152	206	233
80	111	124	156	207	234
81	112	125	157	208	241

5.4 Data Analysis

For the statistical analysis the data were initially binned as follows: KP in bins 0 to 1+, 2- to 3+, 4- to 5+, and ≥ 6 -; LT in eight 3-h bins (0000 to 0300, 0300 to 0600, etc.); and four L-shell bins, 5-6, 6-7, 7-8, and > 8 . Bin averages of the data points were constructed for each energy channel. The number of data points for each bin varied from 0 to 57. The percentages of the number of data points for all L-shell, KP, and LT bins are shown in Figure 25. The poorest sampling overall is for the highest KP bin (≥ 6 -). Additionally, there is no coverage for high L-shell values on the dayside, and spotty coverage for low L-shell values on the night side. When single bin averages are used, the number of points in the bin will be given.

5.4.1 POWER LAW SPECTRA FITTING

Averaged data will be presented in two formats. In one, average fluxes in individual energy channels will be presented as functions of KP, L-shell, and LT. In the second format number densities and mean energies will be calculated for each bin. To do this an energy spectrum is constructed for each bin using the individual energy channel averages. The energy spectrum is then fit by a power law spectrum;

$$\frac{dJ(E)}{dE} = \frac{dJ(E_0)}{dE} \left(\frac{E}{E_0} \right)^\alpha, \quad (15)$$

where $dJ(E)/dE$ is the differential energy flux, E is the energy, E_0 is a reference energy (1keV), and $dJ(E_0)/dE$ is the value of dJ/dE at E_0 . For such a distribution the density over the measured energy range, assuming isotropy, is

$$n = 4\pi \left(\frac{\mu m_p}{2} \right)^{1/2} J(E_0) \frac{1}{(\alpha - 1/2)} \left(\frac{E_2^{\alpha-1/2} - E_1^{\alpha-1/2}}{E_0^\alpha} \right), \quad (16)$$

where E_2 is the maximum energy of the detector in keV, E_1 is the minimum energy of the detector in keV, m_p is the proton mass in gms, μ is the number of AMUs for the ion measured, $J(E_0)$ is the differential energy flux in keV/cm²-sec-sr-keV at the reference energy 1 keV. The average energy of the spectrum over the same range is

$$E_{AVE} = \left[\frac{\alpha - 1/2}{\alpha + 1/2} \right] \left[\frac{E_2^{\alpha+1/2} - E_1^{\alpha+1/2}}{E_2^{\alpha-1/2} - E_1^{\alpha-1/2}} \right]. \quad (17)$$

Figure 26 is a plot of E_{AVE} as a function of the spectral index (α) for $E_2 = 32$ keV, and $E_1 = 0.1$ keV. The average energy is approximately an order of magnitude greater than α . In general, α will be discussed instead of E_{AVE} .

Figure 27 is an example of the average energy spectra for hydrogen and oxygen for the bin: KP = 2, 3; LT = 2100-2400; L-shell = 6 to 7. The averages contain 22 data points. The average values of the differential energy flux are plotted with their positive standard deviations, which are generally large (on the order of or greater than the flux value itself). Standard deviations are higher for oxygen than for hydrogen, and are smallest for both species in the range 2 to 10 keV. Power law fits to the spectra are shown as straight lines. The fits give densities (n), spectral indices (α), and correlation coefficients (r) for

$$\begin{aligned} \text{hydrogen: } n &= 0.72 \text{ cm}^{-3}, \alpha = 0.86, r = 0.99; \text{ and} \\ \text{oxygen: } n &= 0.26 \text{ cm}^{-3}, \alpha = 0.69, r = 0.95. \end{aligned}$$

A definite trend away from the power law fits can be seen for both species at the highest energies as the spectra begin to turn over. Nevertheless, the fits are very good and only fall outside the standard deviations for one point.

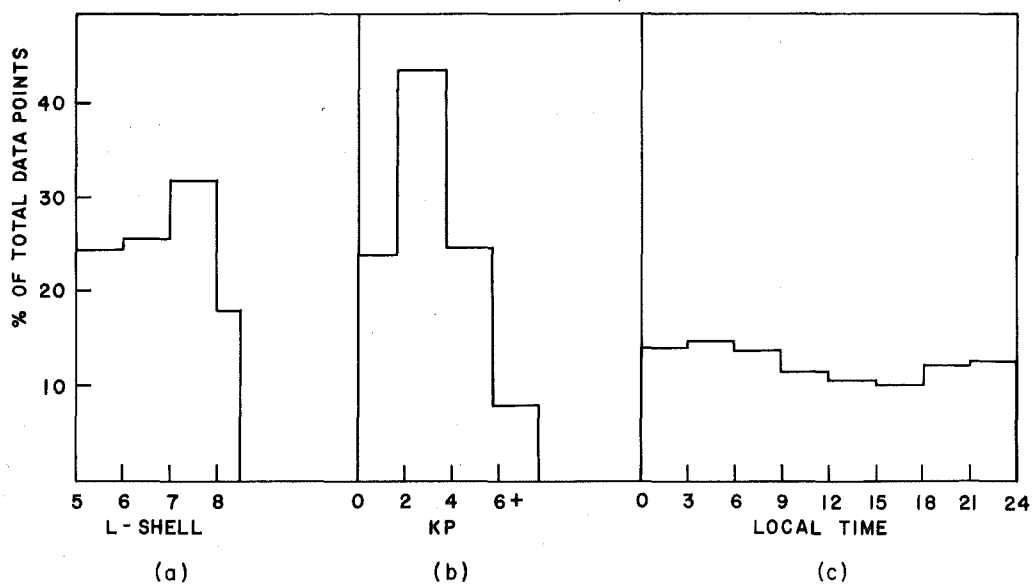


Figure 25. Percentage of SC8 Hourly Average Data Base Points as a Function of (a) L-shell, (b) KP, and (c) LT

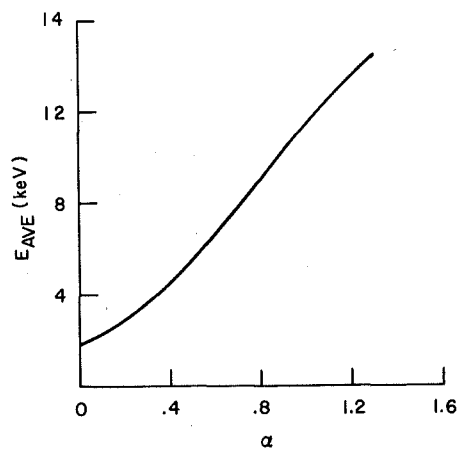


Figure 26. SC8 Average Energy (E_{AVE}) vs the Spectral Index (α) for the SC8 Energy Range 0.1 to 32 keV

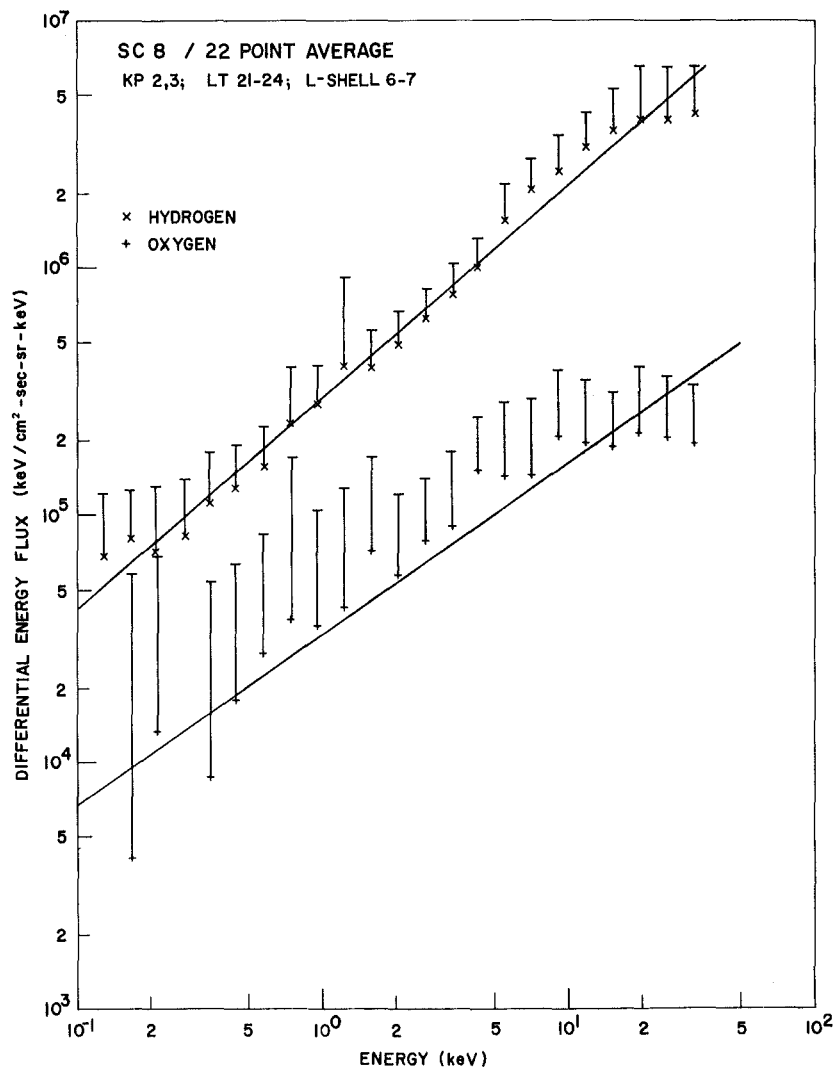


Figure 27. Average Energy Spectra for H^+ (x) and O^+ (+) With Their Positive Standard Deviations for SC8 Data Points for the Ranges $KP \geq 2-$ and $\leq 3+$, L-shell 6 to 7 R_E and LT 2100 to 2400. Superimposed on the spectra are straight line power law fits

5.4.2 THE $n(O^+)/n(H^+)$ RATIO

For each bin described above average values of the $n(O^+)/n(H^+)$ ratios were calculated. Table 26 gives the resulting averages and the number of hourly-averaged spectra that were used to form the averages. The number of data points for the two species are the same. The far right-hand column is the average by bin over LT for a given KP and L-shell. The range of $n(O^+)/n(H^+)$ values is from 0.08 to 3.44, a variation of close to 1.5 orders of magnitude. The extremely high values of the ratio (> 2) occur, with one exception, for highest KP values ($\geq 6-$), and of these, the most extreme are on the dayside. The exception occurs in the lowest KP bin, in the midnight sector, for L between 5 and 6. The lowest values, < 0.3 , occur in the nightside and are more prevalent the lower the KP range, and the higher the L-shell value. Figure 28 shows the distribution of the $n(O^+)/n(H^+)$ ratio over the total bin array. More than 30 percent of the bins have a ratio ≥ 1.0 .

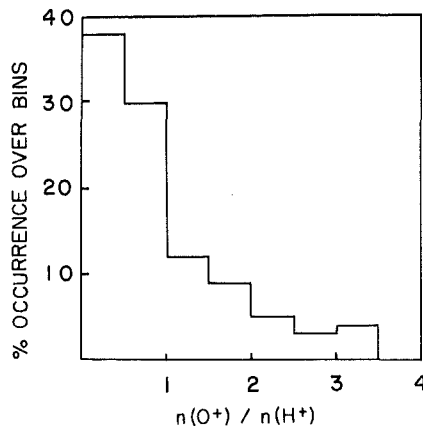


Figure 28. Distribution of the Oxygen to Hydrogen Density Ratios for the SC8 Data Set in Percent of Time the Density Bin Averages Fall Within 0.5 Increments

5.4.3 VARIATION WITH KP

Young et al²⁹ established the geosynchronous variations in the $n(O^+)/n(H^+)$ ratio with KP and solar flux using GEOS 2 data. We use the SC8 data base to

29. Young, D.T., Balsiger, H., and Geiss, J. (1982) Correlations of magnetospheric in composition with geomagnetic and solar activity, J. Geophys. Res. 87:9077.

Table 26. Average $n(\text{O}^+)/n(\text{H}^+)$ Ratios and (Number of Points)

LT	0-3	3-6	6-9	9-12	12-15	15-18	18-21	21-24	Bin Average
L	-	0.75(2)	0.58(11)	0.61(22)	0.67(24)	1.47(21)	1.23(13)	3.06(4)	(1.19±0.89)
KP 0, 1	1.56(5)	0.43(7)	0.35(19)	0.79(7)	1.03(22)	0.65(17)	0.57(9)	0.41(10)	(0.72±0.41)
5	0.25(11)	0.22(33)	0.21(27)	0.66(12)	-	0.46(9)	0.18(15)	0.15(16)	(0.30±0.19)
6	0.08(26)	0.13(18)	0.14(2)	-	-	-	0.16(4)	0.10(16)	(0.12±0.03)
7	-	0.47(3)	0.55(17)	0.59(37)	0.95(55)	0.84(34)	0.79(24)	0.48(3)	(0.67±0.19)
KP 2, 3	0.45(7)	0.23(23)	0.44(18)	0.90(43)	1.35(19)	0.43(21)	0.43(27)	0.36(22)	(0.57±0.37)
5	0.27(43)	0.31(42)	0.58(57)	1.00(9)	1.86(1)	0.35(6)	0.22(27)	0.26(29)	(0.61±0.57)
6	0.12(50)	0.39(30)	0.93(3)	-	-	-	0.16(15)	0.11(30)	(0.34±0.35)
7	-	0.62(3)	0.65(5)	0.47(10)	1.78(27)	1.52(24)	1.32(15)	0.96(6)	(1.05±0.46)
KP 4, 5	0.68(9)	0.61(7)	0.73(12)	1.06(26)	0.83(8)	0.48(10)	0.43(14)	1.07(17)	(0.74±0.24)
6	0.62(18)	0.80(30)	0.92(39)	0.48(8)	0.75(2)	0.46(9)	0.31(13)	0.26(16)	(0.58±0.24)
7	0.33(24)	0.74(22)	-	-	-	-	0.95(4)	0.21(12)	(0.56±0.35)
8	-	2.78(1)	1.67(2)	2.62(3)	3.44(6)	0.51(8)	1.86(10)	-	(2.14±1.03)
KP ≥6-	1.70(5)	2.32(1)	2.71(1)	2.42(7)	3.18(5)	3.40(8)	1.70(2)	1.50(7)	(2.37±0.71)
5	1.17(14)	1.02(5)	1.03(7)	-	-	0.60(2)	2.15(2)	2.03(6)	(1.33±0.62)
6	0.28(12)	1.86(8)	-	-	-	-	0.84(3)	0.53(8)	(0.88±0.69)

confirm the variation with KP and to examine variations in LT and in the limited L-shell range available. Variations in the H^+ and O^+ densities with these variables will also be presented. In each case, the data are averaged by bin in either LT or L-shell and shown as a function of KP and the other variable.

Figure 29 is a plot of the averages by bin over LT for given L-shells (right-hand column in Table 26) as a function of KP. Also shown in Figure 29 (heavy line) is the exponential variation with KP determined by Young et al²⁹ from GEOS 2 satellite data for geosynchronous orbit. (The comparison with the GEOS data will be discussed later in the section.) The figure shows a clear L-shell variation in the density ratios as well as the expected increase in the ratio with KP. However, for low KP and low L the trend reverses, decreasing the ratio from KP 0, 1 to KP 2, 3. For these conditions the satellite is no longer on the average within the plasma sheet, but more likely in the plasmasphere.

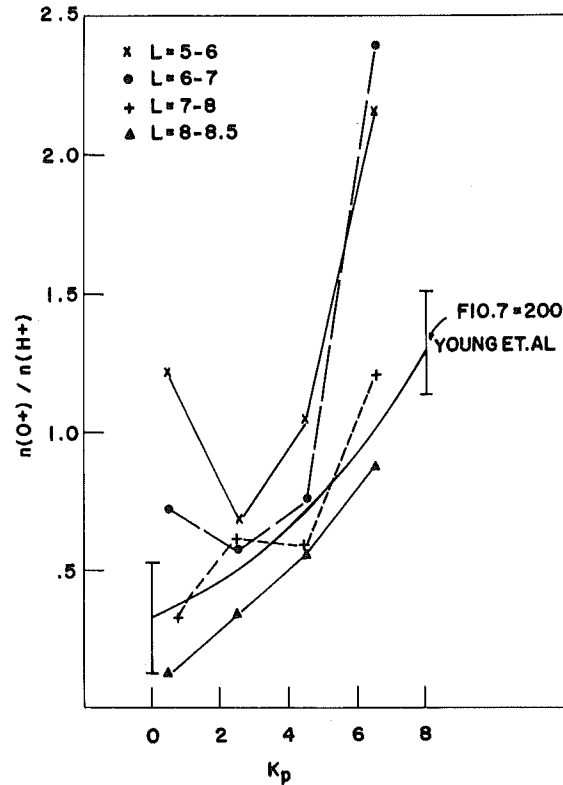


Figure 29. Average Oxygen to Hydrogen Number Density Ratios vs KP for L-shell Ranges (x) 5 to 6 R_E , (o) 6 to 7 R_E , (+) 7 to 8 R_E , and (Δ) 8 to 8.5 R_E . Superimposed on the plot is the empirically determined exponential variation with KP (including error bars) given by Young et al²⁸ for a 10.7-cm flux level of 200

The corresponding O^+ and H^+ densities are shown in Figure 30 as a function of KP. The hydrogen varies much less than oxygen as a function of KP. The variation is near linear. The oxygen varies more exponentially than linearly with KP. The hydrogen density appears to saturate at large KP at about 1 cm^{-3} . On the other hand, no tendency toward saturation appears in $n(O^+)$.

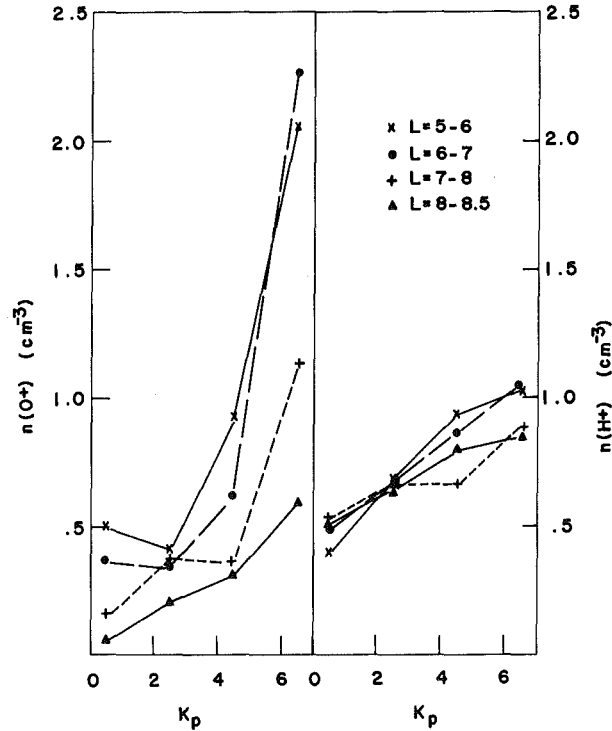


Figure 30. Average Oxygen (Left) and Hydrogen (Right) Number Densities vs KP for L-shell Ranges (x) 5 to 6 R_E , (o) 6 to 7 R_E , (+) 7 to 8 R_E , and (Δ) 8 to 8.5 R_E

5.4.4 VARIATION WITH L-SHELL

Figure 31 presents the same data shown in Figures 29 and 30, but plotted to show L-shell variations for different levels of KP. Logarithmic scales are used for the O^+/H^+ density ratio [Figure 31(a)], the O^+ density [Figure 31(b)] and the H^+ density [Figure 31(c)]. Although there is considerable structure in the variations, overall the density ratio decreases with increasing L values. The ratio variation results almost entirely from the variation in $n(O^+)$. The hydrogen density for each activity range appears as a broadly-peaked distribution in L.

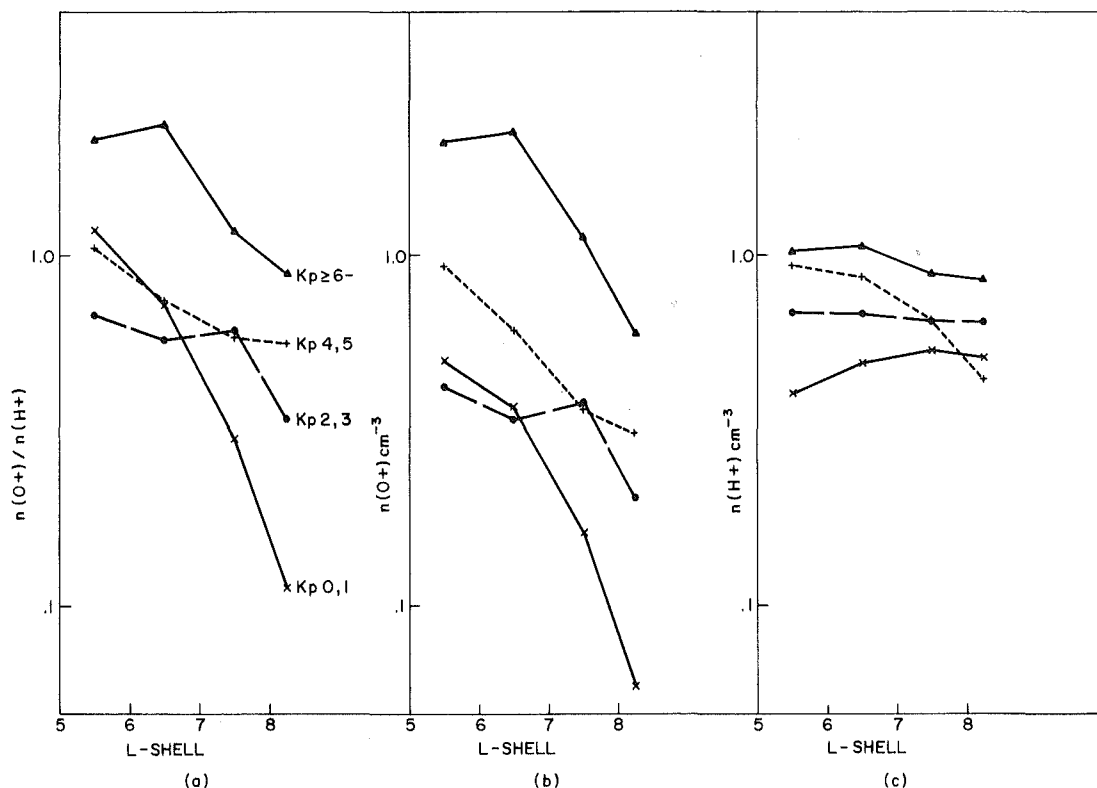


Figure 31. Twenty-four Hour Average Oxygen to Hydrogen Number Density Ratio, (a); Oxygen Number Density, (b); and Hydrogen Number Density, (c) vs L-shell for KP Levels (x), 0, 1, (o) 2, 3, (+) 4, 5, and (Δ) ≥ 6 -

The peak increases and shifts earthward with increasing KP. On the other hand, the oxygen density for each KP range decreases with increasing L. The most regular and severe decrease is for the lowest activity level, KP 0, 1.

Further inspection of Table 26 shows that a significant variation in the O^+/H^+ density ratio occurs as a function of LT. For all except the lowest L and lowest KP range, a local maximum occurs on the dayside in the noon sector. The noon maximum is especially prominent for KP 2, 3 at all L values. These variations, discussed in more detail below, suggest that L-shell variations may also differ in various LT sectors. For this reason we next examine the L-shell variation only over those LT sectors that have strongest contributions from the plasma sheet, namely the 2100 to 0600 LT period in the midnight sector. The results of averaging are given in Figure 32 in the same format as Figure 31.

The hydrogen density again exhibits fewer changes than oxygen as it does for averages over all LT. In particular, the KP 0, 1 curve is nearly identical in form to that in Figure 31(c), the difference being that the midnight sector has slightly

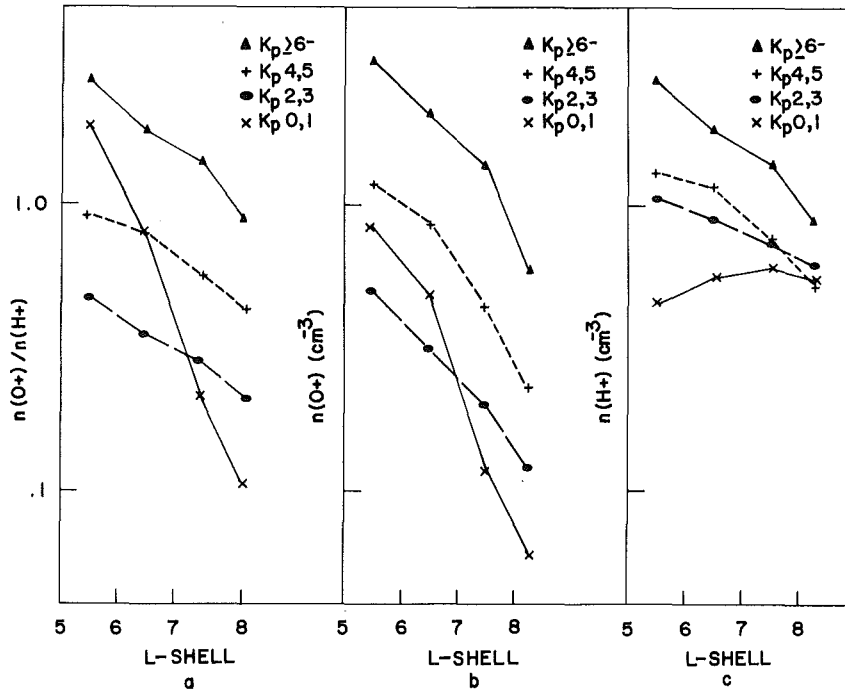


Figure 32. 2100 to 0600 LT Averaged Oxygen to Hydrogen Number Density Ratio, (a); Oxygen Number Density, (b); and Hydrogen Number Density, (c) vs L-shell for KP Levels (\times) 0, 1, (\bullet) 2, 3, ($+$) 4, 5, and (Δ) $\geq 6-$

more enhanced values. This distribution in L and LT suggests a rather uniform ringlike distribution of hydrogen with a broad maximum between $L = 6.5$ and $8.5 R_E$. At times when KP remains within 0, 1 for extended periods, the plasma sheet, as determined by the electron population, can recede well beyond $L = 7 R_E$ in the midnight sector (Gussenhoven, et al³⁰). The hydrogen population may relax outward in this way, as well. For higher levels of activity the hydrogen density is several times higher in the midnight region than the overall average for low L-shells, and decreases with increasing L to near the overall average value for $L > 8 R_E$. Thus, for $KP \geq 2-$ the H^+ density in the midnight sector shows a pronounced increase in density with KP and with decreasing L-values.

The O^+ density is also well-ordered in the midnight sector, falling much faster than $n(H^+)$ with increasing L. Again, the KP 0, 1 case stands out from the other three activity levels for its high values at low L and extraordinarily steep

30. Gussenhoven, M.S., Hardy, D.A., and Burke, W.J. (1981) DMSP/F2 electron observations of equatorward auroral boundaries and their relationship to magnetospheric electric fields, *J. Geophys. Res.* 86:768.

slope. The uniformity in the $n(H^+)$ and $n(O^+)$ variations with L is directly reflected in the variations of the O^+/H^+ density ratio.

We conclude then, that in the midnight sector (2100 to 0600 LT) there are real and systematic decreases with increasing L in all three quantities, $n(H^+)$, $n(O^+)$, and $n(O^+)/n(H^+)$, for all but the lowest magnetic activities. The case of KP 0, 1 appears as an anomaly among these variations, principally because $n(O^+)$ has inflated values at low L . This, coupled with a decreasing hydrogen population at low L leads to extraordinary O^+/H^+ ratios for quiet times over the L -shell range 5.5 to 7 R_E .

Variations with L in other LT periods are hard to characterize. In the noon sector there is some indication that the O^+/H^+ density ratio increases with L . However, there is insufficient data at higher L -values, due to SCATHA orbit constraints, to properly determine any daytime L -dependence.

5.4.5 LT VARIATIONS

To better distinguish LT variations, Figures 33 and 34 show four plots of the O^+ and H^+ density variations as a function of LT for each KP range, for the L -shell range of 6 to 7, and the total L -shell range (excluding data for L greater than 8), respectively. The solid lines represent the O^+ density variations, and the dashed lines those for H^+ . The 0000 to 0300 LT average value is plotted twice, at the beginning and at the end of each graph for continuity through midnight.

In Figure 33 the H^+ variations, which have been found to display relatively small variations in KP or L when averaged over all LT, have LT variations that can be as large as a factor of 5. The H^+ density systematically decreases (except for $KP \geq 6$ -) from the nightside to the dayside. For this single L -range the minimum does not occur in the same 3-h dayside bin for each KP level. Figure 34 also shows the average densities and their standard deviations over the L range 5 to 8 R_E . For the total L -averaged values and for all KP levels, the H^+ density minimum is between 1200 to 1500 LT. Also, the H^+ densities between 1200 to 1500 LT remain nearly constant at values between 0.3 to 0.5 cm^{-3} within the standard deviation of any of the four individual averages. This is in part due to averaging over all L since the minimum moved with LT for $L = 6$ to 7 R_E in Figure 33. Clearly, the minimum in the H^+ density near noon is in part responsible for the increase in the O^+/H^+ density ratio seen earlier on the dayside.

To show how the minimum shifts as a function of energy, Figure 35 shows average energy flux vs LT plots for each individual energy channel. The averages in Figure 35 were taken over the entire SC8 data set for periods when KP was ≥ 2 - and ≤ 3 +. A shift in the position of the minimum to earlier LT with increasing energy is evident. This behavior, which was also shown in the SC5 moment plots, is due to the different trajectories of different energy particles in the

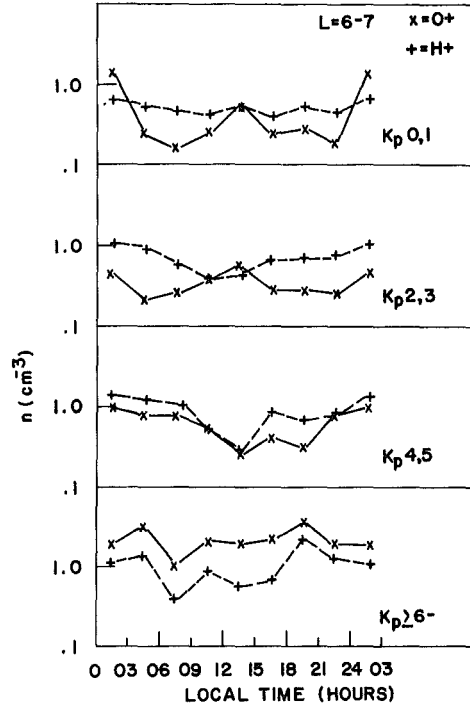


Figure 33. Oxygen (x) and Hydrogen (+) Density Variations as a Function of LT for Four KP Ranges for the L-shell Range of 6 to 7 R_E

Earth's magnetic and electric fields. This type behavior was observed with particle spectrometers on ATS-5 and modeled for the ATS-5 data set by McIlwain.¹² Figure 36 is the same type plot as Figure 35 except for periods $KP \geq 4-$ and $\leq 5+$. The minimums can be seen to change somewhat due to the new field configuration. The well-behaved pattern in LT appears then to be the result of a large portion of the H^+ population originating in the plasma sheet.

The variations of the O^+ density with LT are more complex. Here the total L-average variations are not dissimilar to the $L = 6$ to 7 variations. Therefore, we will focus on the total L-averages in Figure 34. For $KP 2, 3$ there is a maximum in the O^+ density between 1200 to 1500 LT, where the H^+ density minimizes. For $KP 0, 1$ the overall maximum is in the midnight sector, but a local maximum also occurs in the noon sector. Both the lower KP ranges have minimum O^+ densities in the dawn and dusk sectors. For $KP 4, 5$ the O^+ density follows the H^+ density, exceeding it only in the noon sector. For $KP \geq 6-$ the O^+ density is greater than the H^+ density for all LT.

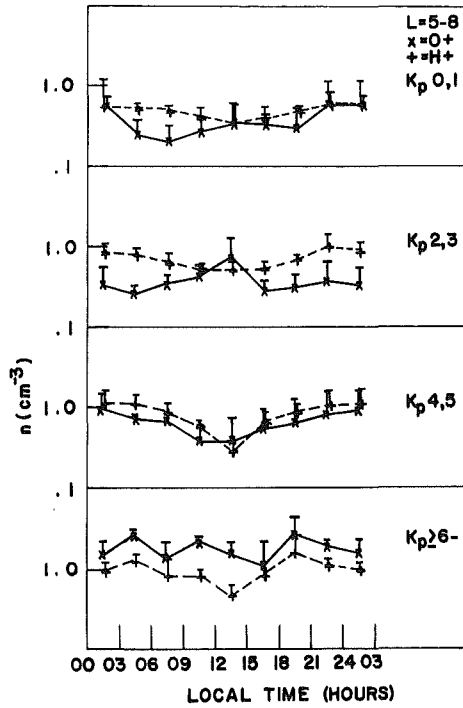


Figure 34. Oxygen (x) and Hydrogen (+) Density Variations as a Function of LT for Four KP Ranges Over the L-shell Range of 5 to 8 R_E

To show energy-dependent LT variations for O^+ similar to those shown for H^+ , Figures 37 and 38 give the average O^+ energy flux vs LT plots for KP 2, 3 and KP 4, 5, respectively. Missing points indicate the average value was below the plot minimum. (This is due in part to the fact negative numbers were retained for the statistics after background subtraction.) The minima here seem to have no well-ordered pattern. Since the ultimate source for the O^+ is the ionosphere, the mechanisms that deposit these ions near-geosynchronous orbits will have to be better understood before the variations can be explained.

5.4.6 POLAR PLOTS

Summary maps of $n(H^+)$, $n(O^+)$, and $n(O^+)/n(H^+)$ in 3-D format for each KP range are given in Figure 39. The format for the plots is the same in all cases. The densities and density ratios are coded and presented in a circular LT - L-shell format, with noon at the top and minimum L toward the center. The coding is in rather crude steps of 0.5 cm^{-3} , except at the lowest values, where the spacing is finer. The top row is the H^+ density, the middle row, the O^+ density, and the bottom row the density ratios. Each column of three maps is for the same KP

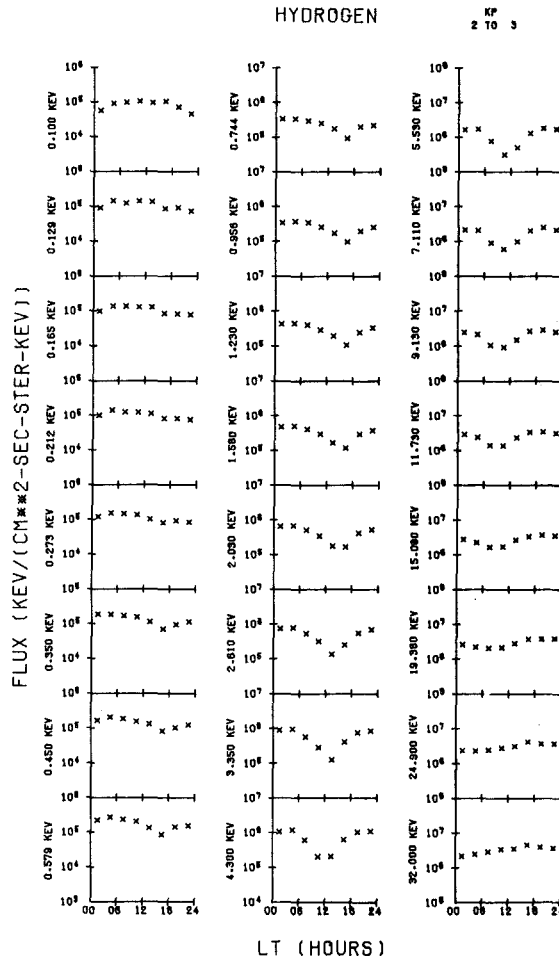


Figure 35. Average Hydrogen Differential Energy Fluxes for All 24 SC8 Channels vs LT for the KP Range $\geq 2-$ and $\leq 3+$

level, with the lowest level on the left. Points to be made for each set of maps [$n(H^+)$, $n(O^+)$, and density ratio] follow sequentially and apply only to the L-shell range 5.5 to 8.5 R_E and the energy range 0.1 to 32 keV.

There is an overall minimum level of the H^+ density between 0.2 and 0.5 cm^{-3} . For the lowest KP range there are enhanced regions above the minimum ranging up to values of 0.5 to 1.0 cm^{-3} . These regions are not well-patterned. As KP increases the density increases from the midnight sector spreading to the dawn and dusk sectors. An overall decrease of the density with increasing L appears in all but the lowest KP levels. The H^+ density has a minimum in the

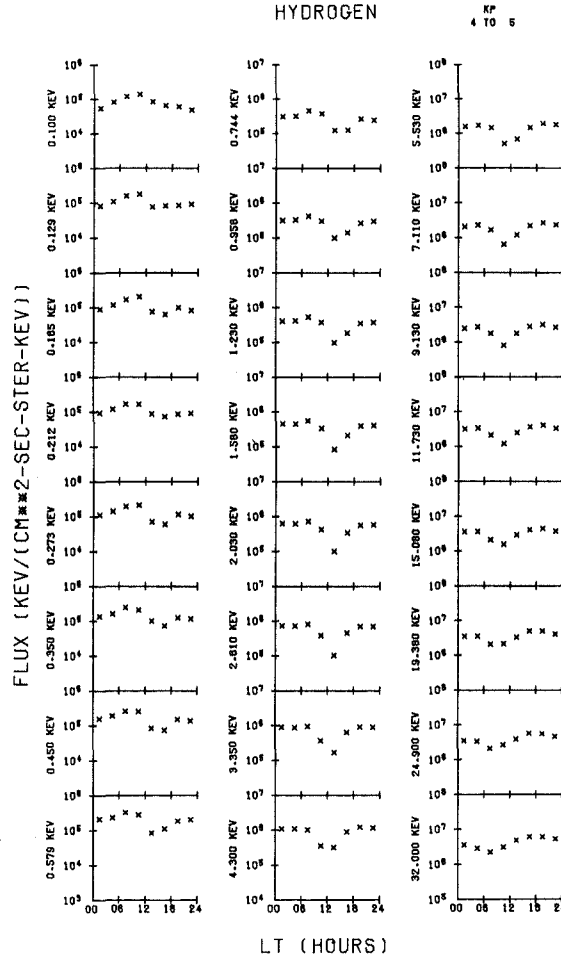


Figure 36. Average Hydrogen Differential Energy Fluxes for All 24 SC8 Channels vs LT for the KP Range $\geq 4-$ and $\leq 5+$

noon sector for all KP levels. The maximum value of the H^+ density is 2.3 cm^{-3} , which occurred in the dusk sector between $L = 6$ and $7 R_E$ at $KP \geq 6-$.

The minimum O^+ density was less than 0.2 cm^{-3} (0.05 cm^{-3} for $L = 8$ to $8.5 R_E$). In the lowest KP range, except for the inner L-shell rings most of the spatial extent of near-geosynchronous altitudes has O^+ densities $< 0.2 \text{ cm}^{-3}$. It is difficult to characterize the way in which the O^+ density increases with magnetic activity. The dramatic increase for the highest KP levels is the most significant feature. The O^+ density has values greater than 1.5 cm^{-3} at all LT and reached maximum values near 4.0 cm^{-3} . The highest densities tend to occur at lowest L values. Unlike the H^+ density there is no regularly occurring minimum in the O^+

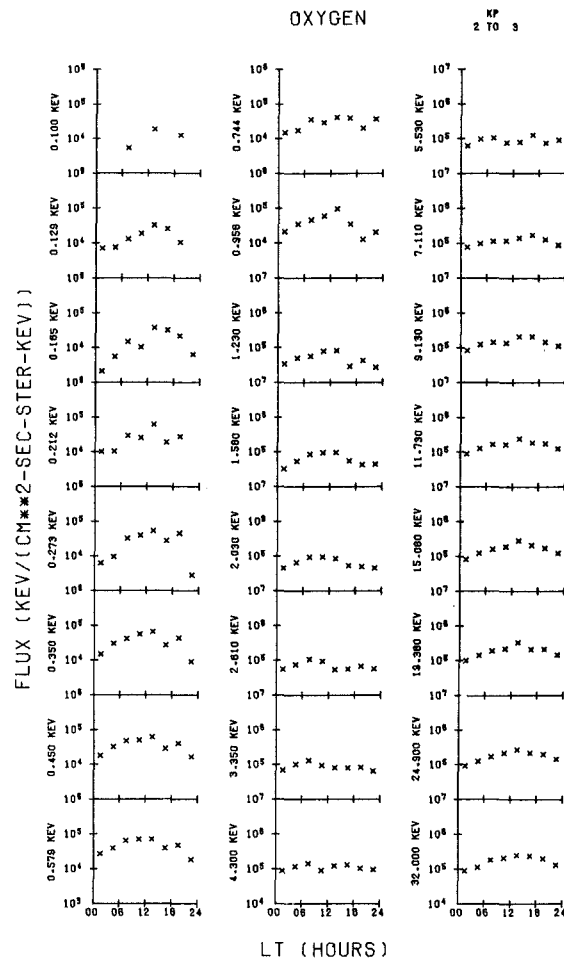


Figure 37. Average Oxygen Differential Energy Fluxes for All 24 SC8 Channels vs LT for the KP Range ≥ 2 - and $\leq 3+$

density near noon. In the midnight sector the O^+ density clearly falls off with increasing L. The maps seem to indicate that multiple source regions exist that cannot be clearly identified here.

The $n(O^+)/n(H^+)$ density ratios have the following properties. They are largest in the dayside, primarily due to decreased H^+ and a possible previously mentioned dayside O^+ source. The KP 0, 1 ratios appear anomalous and need to be studied in more detail. The nightside ratios increase systematically with KP and decrease with L. There is insufficient data to determine where the nightside density ratios maximize in L.

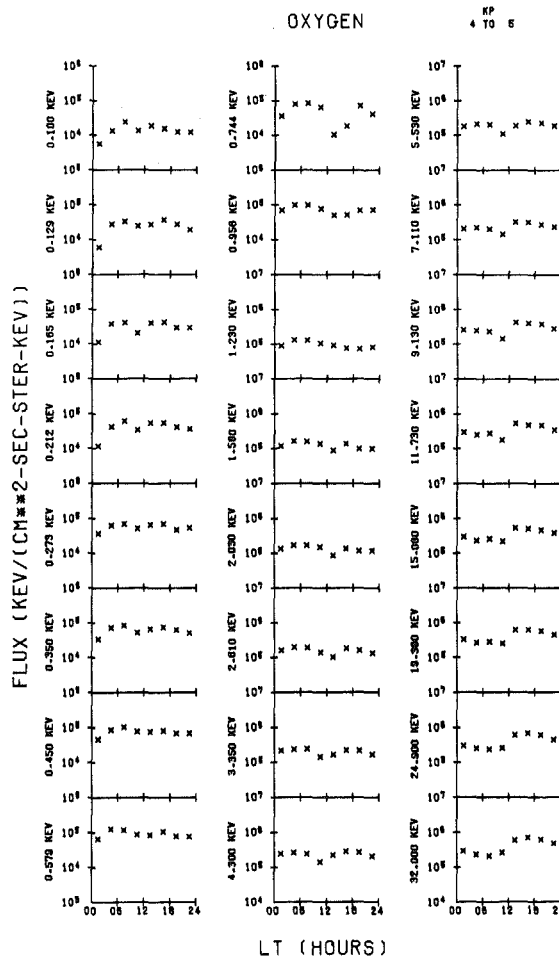


Figure 38. Average Oxygen Differential Energy Fluxes for All 24 SC8 Channels vs LT for the KP Range $\geq 4-$ and $\leq 5+$

5.5 Discussion

The density ratios reported here are much higher than those reported by Balsiger et al³¹ for 1977 and 1978 GEOS 1 and 2 data. However, the ratios are near those reported by Young et al²⁹ for 1979 GEOS 2 data. A large statistical study done by Young et al²⁹ using four years of GEOS 1 and 2 ion composition data from 1977 to 1981 showed that the O^+ density increases not only with magnetic activity (KP), but also with solar EUV flux. They propose that as the EUV flux

31. Balsiger, H., Eberhardt, P., Geiss, J., and Young, D.T. (1980) Magnetic storm injection of 0.9- to 16- keV/e solar and terrestrial ions into the high-altitude magnetosphere, J. Geophys. Res. 85:1645.

increases, the O^+ scale height in the ionosphere is raised. This brings a larger population of O^+ into regions where acceleration mechanisms (specifically those due to parallel electric fields) operate to move O^+ up from the ionosphere into the magnetosphere. Since solar EUV flux increases toward solar maximum and the solar maximum for this solar cycle began around 1979, the increased O^+/H^+ density ratios reported here are consistent with current thinking.

A more specific comparison of SCATHA data with GEOS 2 data can be seen in Figure 29. Here the empirically-determined exponential density ratio variation with KP given by Young et al²⁹ for a 10.7-cm flux of 200 is superimposed on the SC8 measured ratios. For the moderate KP range (2- to 5+), where our statistical sample is best, the average values in our study fall within the error bars of the GEOS 2 curve (shown at the two ends of the curve) with one exception (L between 5 and 6 R_E and KP between 4- and 5+). The differences in the lowest and highest KP ranges for the L-shell range 5 to 7 R_E is probably in part due to the small statistical sample, but is also probably due in part to real L-variations because of different L-sampling regions of SCATHA and GEOS 2. The good overall agreement between the SCATHA and GEOS 2 data sets supports our results which use a much smaller data base, and it, in effect, cross calibrates SC8 with the GEOS 2 instrument.

One of the most interesting and useful aspects of ion measurements is their highly anisotropic and transient character, which provides direct information on acceleration and transport mechanisms. Since the ion composition data available for the atlas did not contain pitch angle information, a short summary of two studies of SCATHA data by Lockheed scientists (Kaye et al^{27, 32}) will be presented here.

Kaye et al²⁷ conducted a statistical study of 94 short-lived H^+ and O^+ bursts observed in the equatorial magnetosphere. They concluded:

1. The bursts were transient phenomena with characteristic lifetimes of the order of minutes, which occurred in either or both H^+ and O^+ but predominantly in O^+ , and which were associated with enhanced levels of geomagnetic activity.
2. The bursts had a local time distribution which peaked near midnight, and there were more bursts observed postmidnight ($L > 7$) than premidnight ($L < 7$).
3. The average energy of the bursts was < 1 keV, with energy widths of the order of $\Delta W / \langle W \rangle \simeq 0.5 - 1.5$.
4. The pitch angle distributions of 90 percent of the bursts were consistent with approximately field aligned distributions near the equator.
5. Although most of the bursts had a simple structure, some of them had pitch angle distributions that varied with energy.

32. Kaye, S.M., Shelley, E.G., Sharp, R.D., and Johnson, R.G. (1981b) Ion composition of zipper events, J. Geophys. Res. 86:3383.

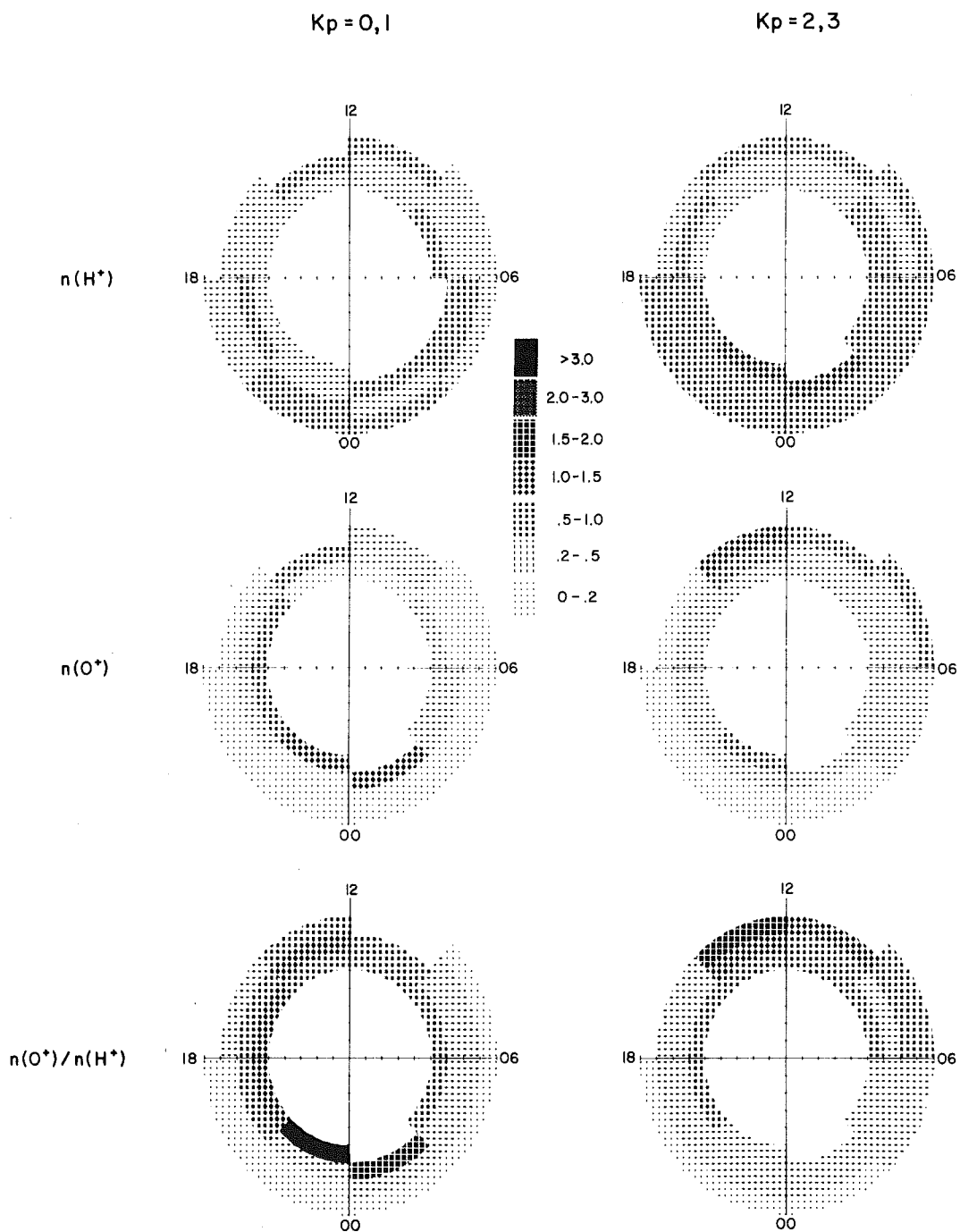


Figure 39. SC8 Hydrogen (Top), Oxygen (Middle), and O^+/H^+ (Bottom) Coded Densities in Polar Coordinate LT - L-shell Formats for KP Levels 0, 1 (Left), 2, 3 (Left Center), 4, 5 (Right Center) and ≥ 6 (Right). The code levels (density and ratio) are given in the center of each page

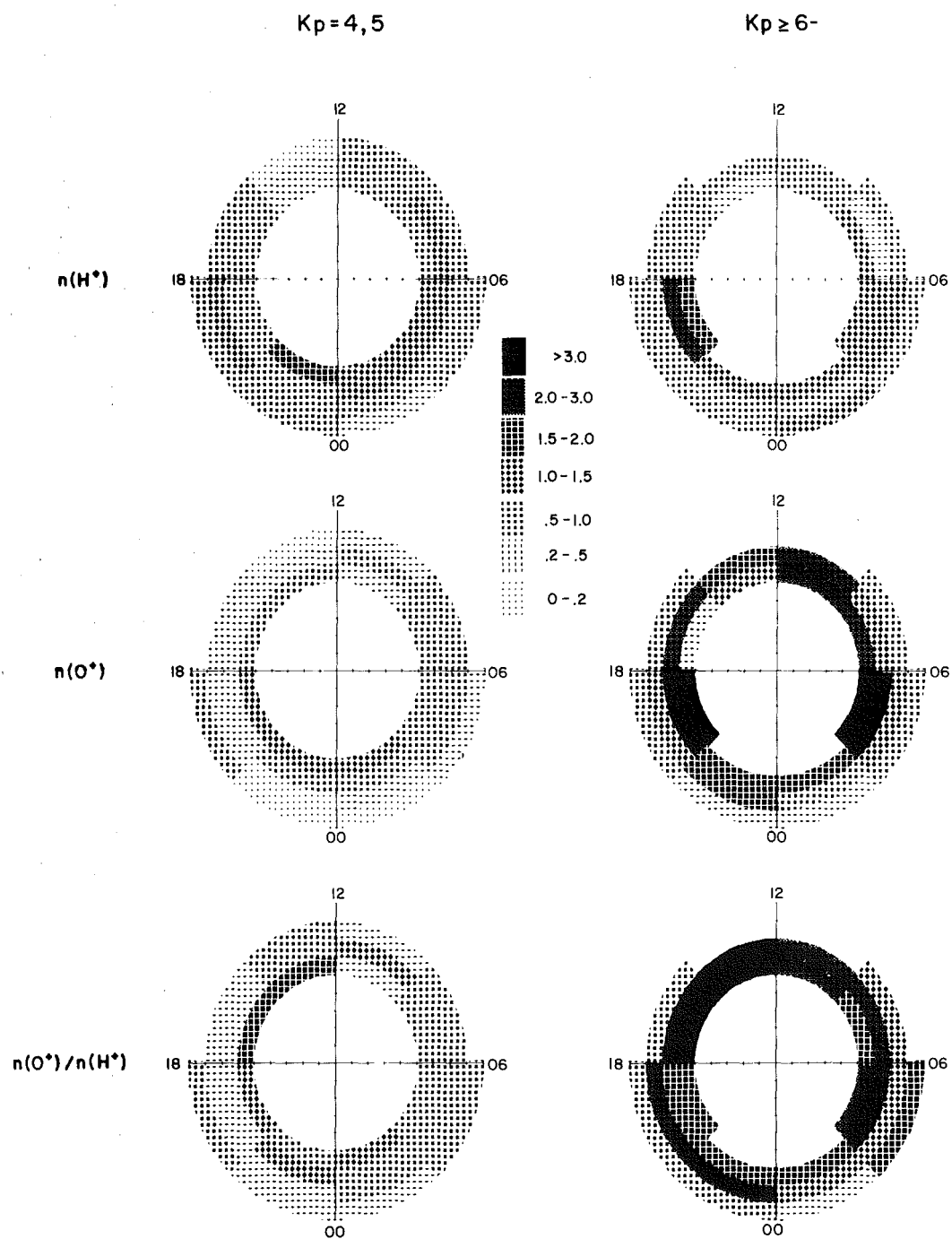


Figure 39. (Contd)

6. The pitch angle width of the bursts was typically $5^\circ - 25^\circ$."

In the second study, Kaye et al³² investigated the ion composition of "zipper events" first identified by Fennell et al³³ from SCATHA spectrograms. On an energy vs time spectrogram, an ion distribution composed of a low-energy component with peak fluxes along the field line and a high-energy component with peak fluxes perpendicular to the field line appear as a zipper. Kaye et al found from their study that the low-energy component parallel to the field was primarily O^+ and the high-energy component perpendicular to the field was primarily H^+ . They concluded that two different sources existed for the two populations, "a direct ionospheric source for the low-energy and primarily parallel fluxes and most probably the plasma sheet for the higher-energy and primarily perpendicular fluxes."

In summary, high solar flux levels occurred during the period of SCATHA data collection used in this atlas. This resulted in unusually high O^+/H^+ density ratios, but ratios which are consistent with other measurements taken over the same period. No comparable statistical study of O^+/H^+ density ratio variations with L-shell or LT has yet been performed. The results here indicate variations do exist that must be considered in developing models of the near-geosynchronous regime.

6. SC11 MAGNETIC FIELD RESULTS

Magnetic field measurements on the SCATHA satellite were made by the SC11 magnetometer that was built and operated under the direction of Dr. B.G. Ledley of NASA/Goddard. The model field values and L-shell values used here and in other sections of this report were obtained from a 1976 version of the Olson-Pfizer³⁴ model field that includes the dipole tilt and seasonal effects.

6.1 Introduction

Magnetic field measurements in the near-geosynchronous regions of space are necessary to understand certain dynamic properties of the magnetosphere relating to spacecraft charging. Models of the magnetic field typically describe an average, quiet field, and cannot be used to study plasma-field interactions in a disturbed magnetosphere. As has been shown in earlier sections, magnetic field

33. Fennell, J.F., Croley, Jr., D.R., and Kaye, S.M. (1981) Low-energy ion pitch-angle distributions in the outer magnetosphere: Ion zipper events, J. Geophys. Res. 86:3375.

34. Olson, W.P., and Pfizer, K.A. (1974) A quantitative model of the magnetospheric magnetic field, J. Geophys. Res. 79:3739.

measurements are critical to understanding particle measurements especially during periods of highly anisotropic flux distributions.

In this section we will compare SCATHA magnetic field measurements with a model field at different L-shell values for different magnetic activity levels. More importantly, we will compute the magnetic pressure and compare it directly to the total particle pressure. Results of this section will be useful in future studies relating to wave-particle interactions and should contribute to a better understanding of magnetosphere dynamics as it affects spacecraft charging.

6.2 Instrumentation

The SC11 magnetometer is a triaxial fluxgate magnetometer with the three sensors mounted in a mutually orthogonal configuration. The magnetometer sensors are located at the end of a 4-m boom. Each axis has a range of approximately ± 500 gammas ($1 \text{ gamma} = 10^{-5} \text{ Gauss}$). Preflight calibrations indicated that the absolute accuracy of the measurement of the ambient magnetic field along any of the three axes was less than 1 gamma at a 1 sigma confidence level. A calibration pulse built into the instrument is used to check the sensitivity levels of all three axes on orbit.

6.3 Data Base

The SC11 magnetic field data were received from Patrick Air Force Base as 15-sec averages of the three components of the magnetic field (B_x , B_y , and B_z) in Earth-centered inertial (ECI) coordinates. Also received were the three components of the Olson-Pfitzer³⁴ model field and the L-shell values computed from the model for the same periods as the SC11 data. The magnetic field data (measured and modeled) were first transformed into solar magnetic (SM) coordinates. In SM coordinates B_z is parallel to the north magnetic pole, B_y is perpendicular to the Earth-sun line, and B_x completes the Cartesian coordinate system and is positive in the sunward direction. A data base of 15-sec values for 120 days listed in Table 27 was used in the atlas studies. In addition to the 15-sec average data base, a data base of 1-min averages of the total magnetic field pressure ($B^2/8\pi$) in eV/cm^3 was generated to compare to the particle pressures calculated from the SC5 data.

6.4 Data Analysis

For each day in the data base the three components of the SC11 measured magnetic field and the Olson-Pfitzer model field in SM coordinates were plotted together as a function of UT. For magnetically quiet times ($KP \leq 1+$) the model field was found to be in excellent agreement with the measured values.

Table 27. SC11 Data Base Days

Yr	Day	Yr	Day	Yr	Day
1979	59	1979	145	1979	272
	76		146		273
	77		149		278
	80		150		279
	81		152		280
	87		156		281
	88		157		282
	89		158		293
	90		160		301
	91		164		309
	93		166		311
	94		167		317
	95		168		319
	103		172		323
	104		178		328
	108		180		329
	110		188		331
	111		194		341
	112		200		348
	113		206		351
	114		207		357
	115		208		359
	116		210		361
	117		212		363
	118		216	1980	4
	119		218		12
	120		225		18
	121		226		27
	122		227		28
	123		230		36
	124		232		37
	125		233		42
	126		234		46
	127		241		47
	128		248		161
	129		254		162
	138		261		163
	141		262		164
	142		264		165
	144		271		166

Figures 40 through 43 show the measured field components B_x , B_y , and B_z (solid lines) in gammas (nanoteslas) superimposed on the respective model field components (dashed lines) as a function of UT, LT, MLT, magnetic latitude, L-shell, geographic latitude, and geographic longitude. The four days (days 156, 212, and 309, 1979 and day 36, 1980) are all magnetically quiet days ($\Sigma KP = 8, 4+, 4+, \text{ and } 6-, \text{ respectively}$) and represent periods when the satellite was near perigee in the noon, morning, midnight and evening LT regions. The measured and model fields

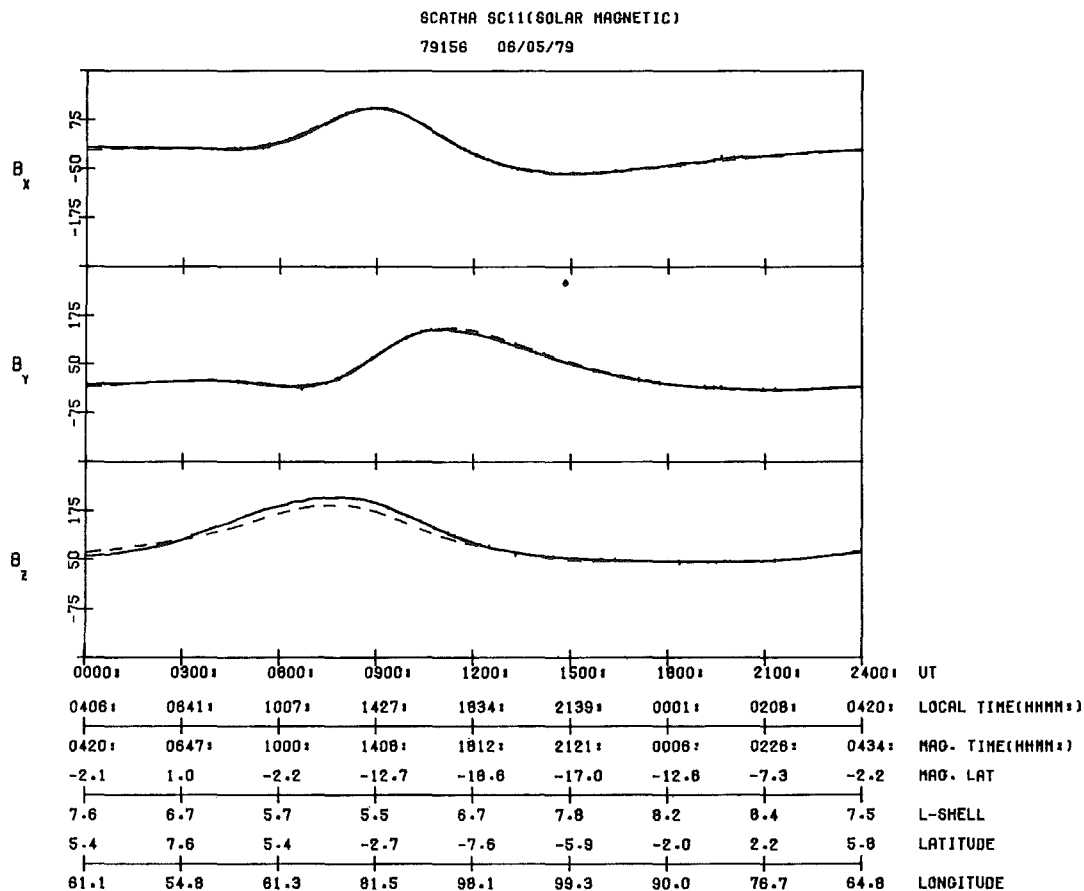


Figure 40. Magnetic Field Intensities in Gammas as Measured on (Solid Line) and Modeled for (Dashed Line) the SCATHA Satellite on a Magnetically Quiet Day, Day 156, 1979. The B_x (top), B_y (middle), and B_z (bottom) components in solar magnetic coordinates are plotted vs UT, LT, MLT, magnetic latitude, L, geographic latitude, and geographic longitude

SCATHA SC11(SOLAR MAGNETIC)
79212 07/31/79

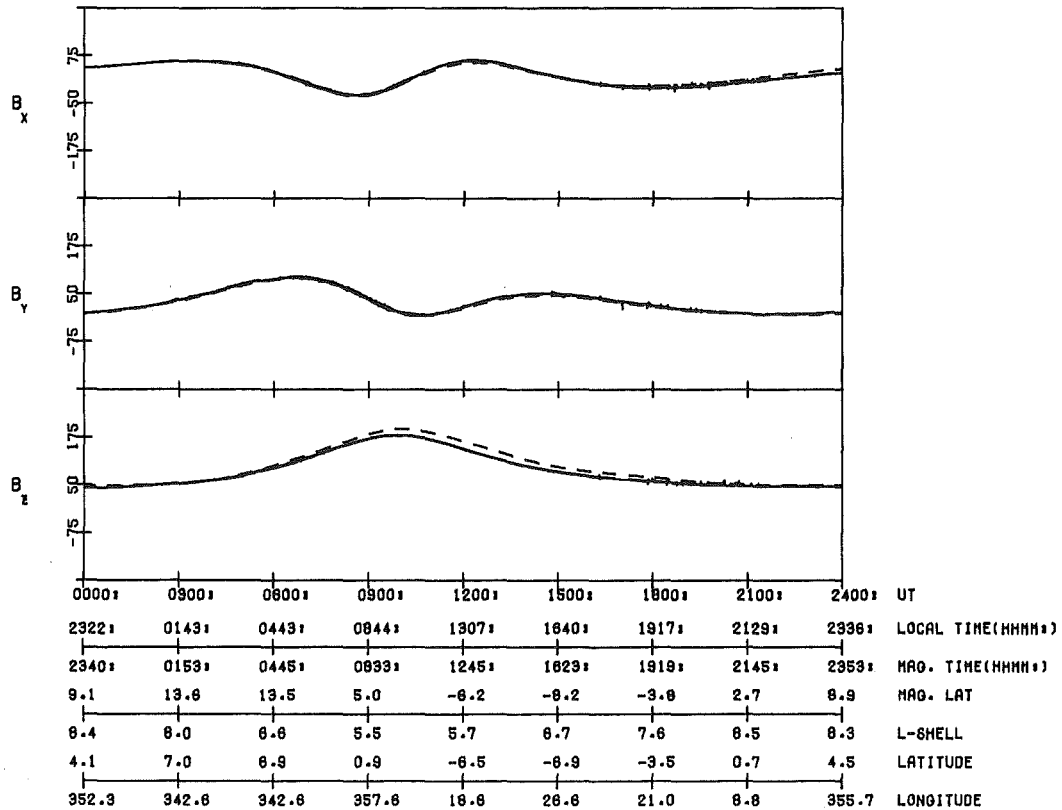


Figure 41. Magnetic Field Intensities in Gammas as Measured on (Solid Line) and Modeled for (Dashed Line) the SCATHA Satellite on a Magnetically Quiet Day, Day 212, 1979. The B_x (top), B_y (middle), and B_z (bottom) components in solar magnetic coordinates are plotted vs UT, LT, MLT, magnetic latitude, L, geographic latitude, and geographic longitude

SCATHA SC11(SOLAR MAGNETIC)

79309 11/05/79

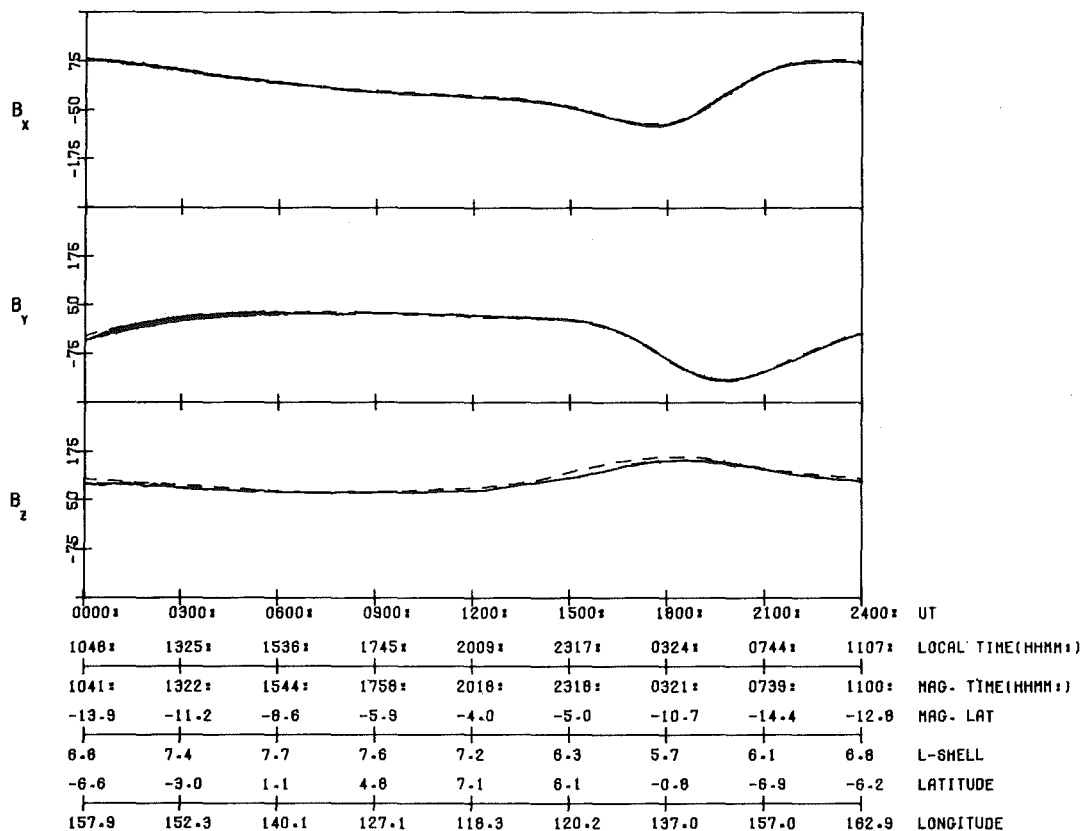


Figure 42. Magnetic Field Intensities in Gammas as Measured on (Solid Line) and Modeled for (Dashed Line) the SCATHA Satellite on a Magnetically Quiet Day, Day 309, 1979. The B_x (top), B_y (middle), and B_z (bottom) components in solar magnetic coordinates are plotted vs UT, LT, MLT, magnetic latitude, L, geographic latitude, and geographic longitude

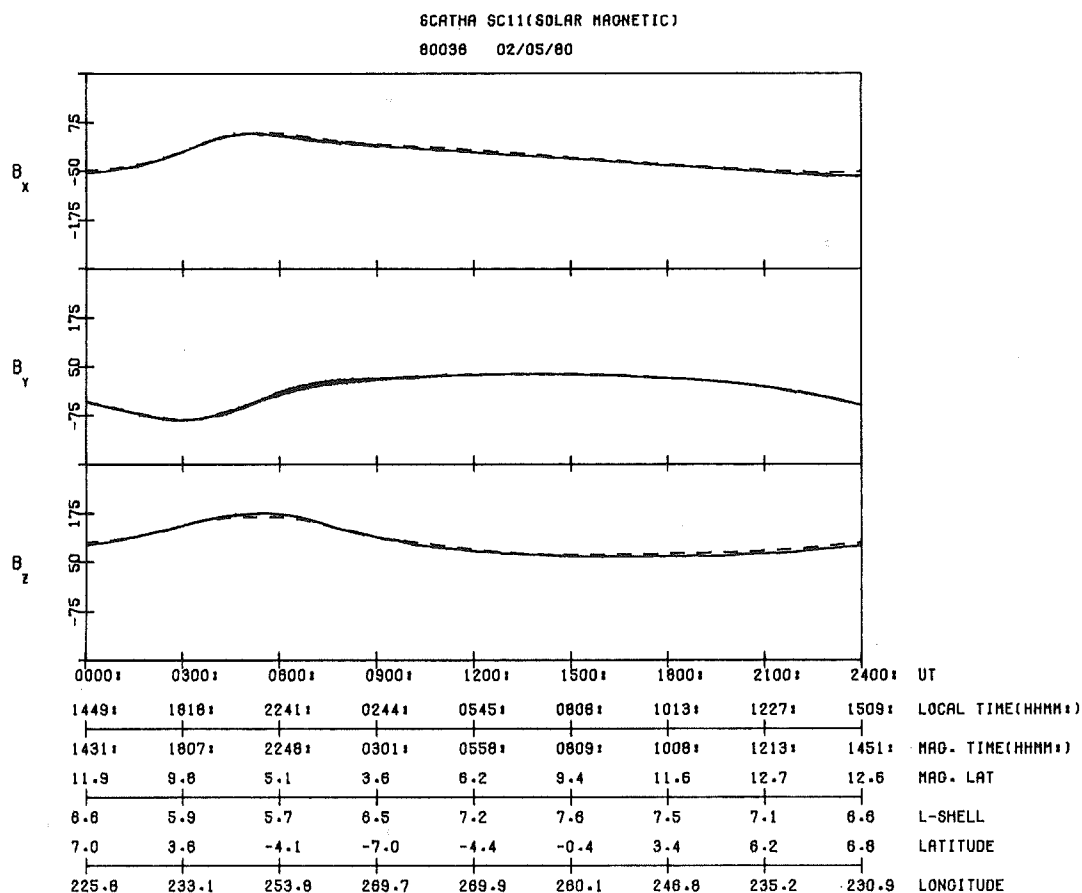


Figure 43. Magnetic Field Intensities in Gammas as Measured on (Solid Line) and Modeled for (Dashed Line) the SCATHA Satellite on a Magnetically Quiet Day, Day 36, 1980. The B_x (top), B_y (middle), and B_z (bottom) components in solar magnetic coordinates are plotted vs UT, LT, MLT, magnetic latitude, L, geographic latitude, and geographic longitude

agree particularly well for the x- and y-components, and show disagreement of 5 to 10 percent in the z-component only in the most earthward positions. Thus, the geosynchronous region is very well modeled by Olson-Pfizer for magnetically quiet periods. On the other hand, Figures 44 and 45 show data for two very magnetically active days (days 115 and 241, 1979 with $\Sigma KP = 54$ - and 45-, respectively). Here it can be seen that although the model gives a good baseline, deviations can be very large in all three components of B.

To determine the average variations in B as a function of L-shell, KP, and LT, the measured field components (15-sec averages) were subtracted from the model field components and the differences averaged as a function of LT in 1-h bins, L-shell in $0.5 R_E$ bins, and KP in the familiar 0, 1; 2, 3; 4, 5; and ≥ 6 - bins. The resulting averages and their standard deviations (σ 's) are given in Tables 28 through 30 for B_x , B_y , and B_z , respectively. Each average value contains over 20000 points. For B_x the largest σ 's and average differences occur in the midnight region (2100 to 0300 LT) at high L-values and for high KP. For B_y the largest σ 's and average differences are early morning (0100 to 0600 LT) and late evening (1800 to 2200 LT). The L and KP average differences are all near zero while the L and KP σ 's increase with distance and magnetic activity level, respectively. The B_x and B_y component average differences are small relative to the σ 's and can be positive or negative. The B_z average differences, on the other hand, are all positive and significantly large except possibly for the KP 0, 1 case, the σ 's are also all large. The differences are larger on the nightside than the dayside. The z-component of the magnetic field measures departures from a dipole type field to a more taillike field and is most sensitive to small changes in magnetic activity levels. Figure 46 shows an example of this for day 172, 1979, a day in which KP ranged from 2- to 4. A long lasting difference of 20 to 50 γ 's can be seen in B_z , while B_x and B_y remain near the model values except for very short periods. It might be possible to model these long time (on the order of hours) decreases in B_z during moderate KP conditions ($2 \leq KP \leq 4$) but no attempt will be made here. The high KP conditions seen in Figures 44 and 45 are seemingly beyond present modeling capabilities. In summary, the magnetic field model (Olson and Pfizer³⁴), tested near-geosynchronous altitudes, is in excellent agreement with measured data for low KP levels (KP 0, 1), has a significantly higher B_z component of the field in SM coordinates for moderate KP levels (2 to 4); and can only be used as a baseline from which to look at field deviations for high KP levels (KP ≥ 4).

In Section 4 statistical analyses were performed on the total particle energy density. Here we present the corresponding results of analyses of the magnetic field energy density, $B^2/8\pi$. One-minute averages of $B^2/8\pi$ were binned in L-shell, KP and LT and the bin averages calculated. Figures 47 and 48 show the

SCATHA SC11(SOLAR MAGNETIC)
79115 04/25/79

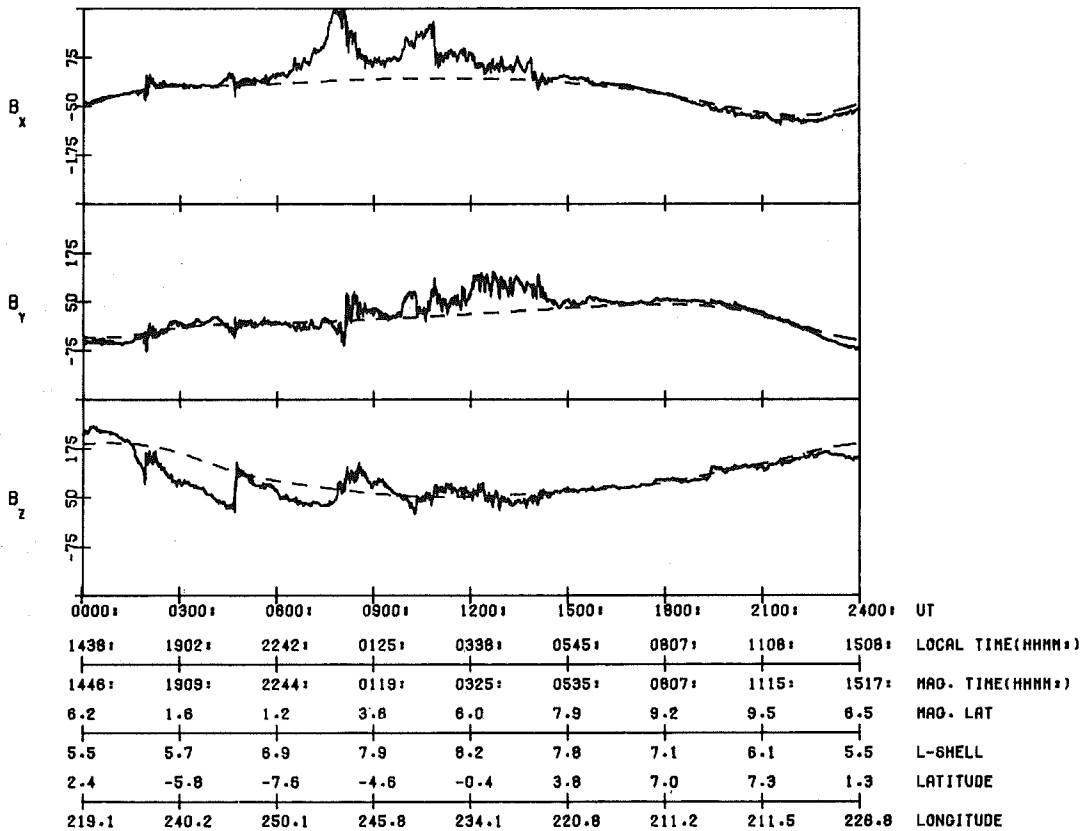


Figure 44. Magnetic Field Intensities in Gammas as Measured on (Solid Line) and Modeled for (Dashed Line) the SCATHA Satellite on a Magnetically Disturbed Day, Day 115, 1979. The B_x (top), B_y (middle), and B_z (bottom) components in solar magnetic coordinates are plotted vs UT, LT, MLT, magnetic latitude, L, geographic latitude, and geographic longitude

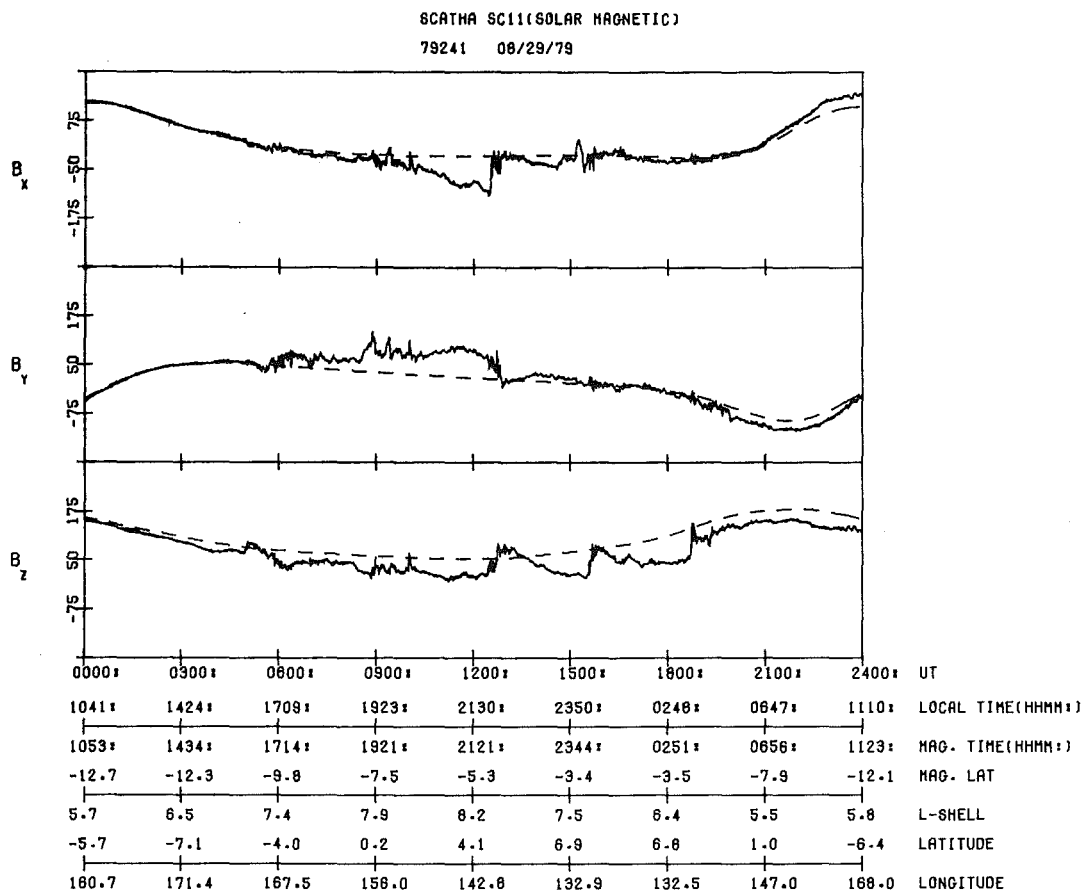


Figure 45. Magnetic Field Intensities in Gammas as Measured on (Solid Line) and Modeled for (Dashed Line) The SCATHA Satellite on a Magnetically Disturbed Day, Day 241, 1979. The B_x (top), B_y (middle), and B_z (bottom) components in solar magnetic coordinates are plotted vs UT, LT, MLT, magnetic latitude, L, geographic latitude, and geographic longitude

Table 28. Magnetic Field Model - Measured B_x Averages

LT (h)	B_x (Model - Measured) Average (γ)	σ (γ)
00-01	-9.2	31.8
01-02	-6.8	21.4
02-03	-6.4	21.8
03-04	-2.5	14.2
04-05	-1.9	10.4
05-06	-0.8	8.7
06-07	-0.3	8.1
07-08	-1.6	8.1
08-09	-1.6	8.8
09-10	-1.1	7.9
10-11	-0.6	7.1
11-12	-0.6	7.0
12-13	-0.0	6.7
13-14	1.0	8.3
14-15	0.9	9.3
15-16	1.2	11.2
16-17	0.8	11.9
17-18	1.2	12.2
18-19	0.4	11.8
19-20	-0.4	11.9
20-21	-1.1	14.7
21-22	-2.6	20.7
22-23	-4.9	25.7
23-24	-7.3	29.0
<u>L-shell (R_E)</u>	<u>Average (γ)</u>	<u>σ (γ)</u>
5.2-6.0	0.8	12.5
6.0-7.0	0.1	12.2
7.0-8.0	-1.8	16.6
≥ 8.0	-9.6	20.7
<u>KP</u>	<u>Average (γ)</u>	<u>σ (γ)</u>
0, 1	0.4	8.7
2, 3	-1.3	11.9
4, 5	-2.6	16.8
≥ 6	-9.1	34.3

Table 29. Magnetic Field Model - Measured B_y Averages

LT (h)	B_y (Model - Measured) Average (γ)	σ (γ)
00-01	-0.5	9.5
01-02	-3.7	13.4
02-03	-7.0	19.7
03-04	-6.3	22.0
04-05	-4.3	19.5
05-06	-3.0	16.0
06-07	-0.8	12.9
07-08	0.4	9.7
08-09	1.0	9.1
09-10	1.2	9.5
10-11	0.8	8.8
11-12	1.7	11.3
12-13	1.3	9.0
13-14	1.6	11.5
14-15	1.7	9.3
15-16	0.9	10.6
16-17	0.2	10.7
17-18	0.6	14.3
18-19	2.3	17.4
19-20	2.3	21.5
20-21	3.4	19.7
21-22	3.5	18.0
22-23	2.7	12.6
23-24	2.0	10.2
<u>L-shell (R_E)</u>	<u>Average (γ)</u>	<u>σ (γ)</u>
5.2-6.0	1.1	12.2
6.0-7.0	0.1	12.8
7.0-8.0	-0.9	13.8
≥ 8.0	0.5	21.2
<u>KP</u>	<u>Average (γ)</u>	<u>σ (γ)</u>
0, 1	0.1	5.9
2, 3	0.3	11.0
4, 5	-0.5	17.7
≥ 6 -	0.2	29.5

Table 30. Magnetic Field Model - Measured B_z Averages

LT (h)	B_z (Model - Measured) Average (γ)	σ (γ)
00-01	21.0	19.3
01-02	19.1	18.7
02-03	18.2	18.9
03-04	17.6	17.8
04-05	17.9	14.9
05-06	15.4	14.0
06-07	11.6	14.4
07-08	7.7	14.0
08-09	7.5	17.5
09-10	6.0	19.1
10-11	5.9	19.5
11-12	6.7	24.0
12-13	6.6	23.8
13-14	9.9	24.4
14-15	10.2	22.7
15-16	10.7	23.1
16-17	12.5	23.1
17-18	18.2	21.9
18-19	23.9	21.7
19-20	26.9	21.4
20-21	23.5	20.1
21-22	19.8	18.8
22-23	20.2	17.6
23-24	21.6	17.6
<u>L-shell (R_E)</u>	<u>Average (γ)</u>	<u>σ (γ)</u>
5.2-6.0	19.8	24.7
6.0-7.0	15.7	21.7
7.0-8.0	11.2	18.8
≥ 8.0	15.4	13.7
<u>KP</u>	<u>Average (γ)</u>	<u>σ (γ)</u>
0, 1	4.5	10.5
2, 3	13.6	16.4
4, 5	21.4	23.8
≥ 6 -	29.3	31.9

SCATHA SC11(SOLAR MAGNETIC)
79172 06/21/79

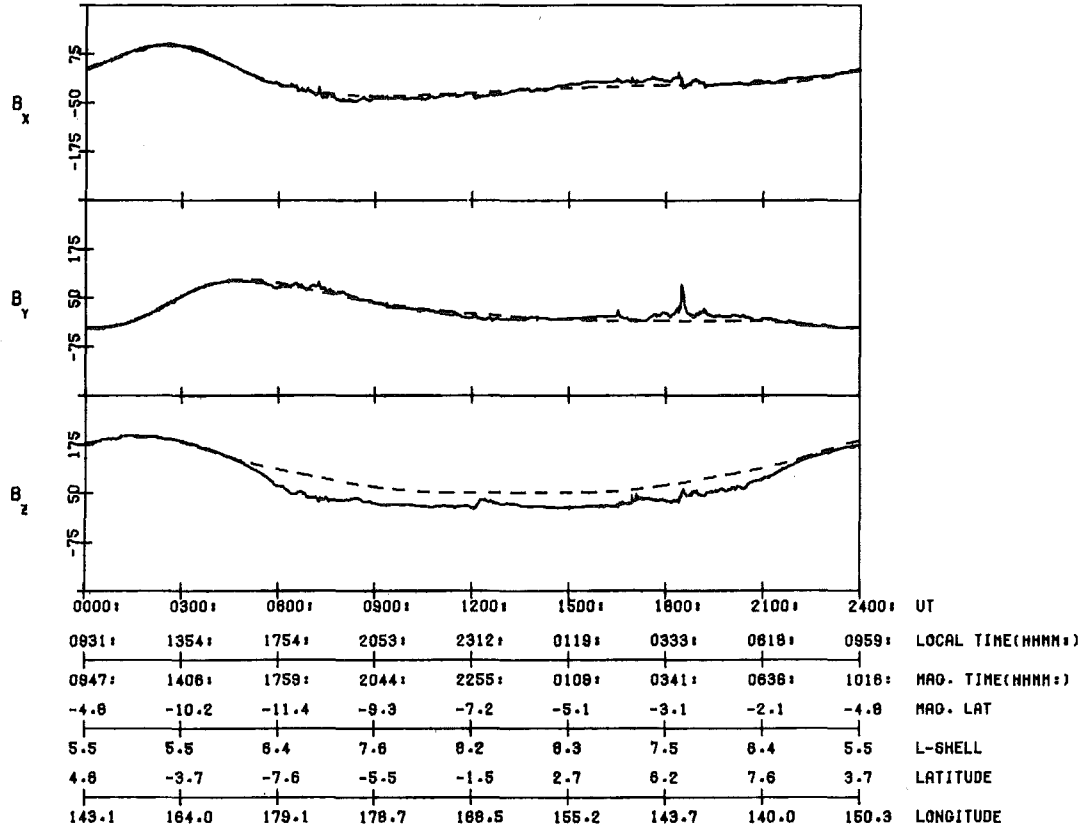


Figure 46. Magnetic Field Intensities in Gammas as Measured on (Solid Line) and Modeled for (Dashed Line) the SCATHA Satellite on a Moderately Active Day, Day 172, 1979. The B_x (top), B_y (middle) and B_z (bottom) components in solar magnetic coordinates are plotted vs UT, LT, MLT, magnetic latitude, L, geographic latitude, and geographic longitude

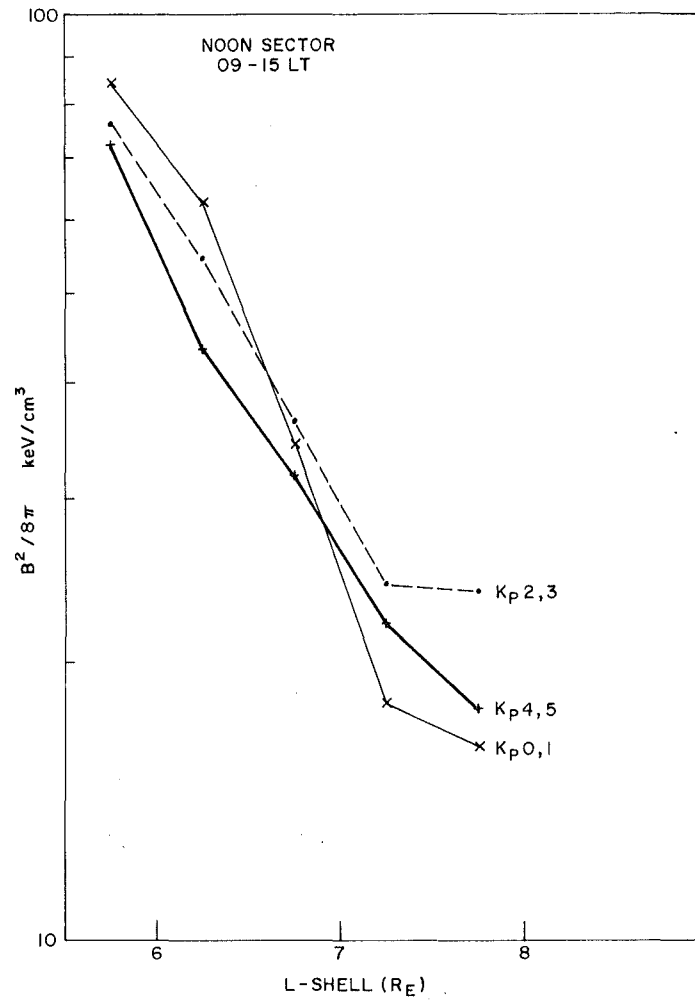


Figure 47. Average Magnetic Field Energy Densities Between 0900-1500 LT vs L-shell for KP Ranges (x) 0 to 1+, (o) 2- to 3+, and (+) 4- to 5+

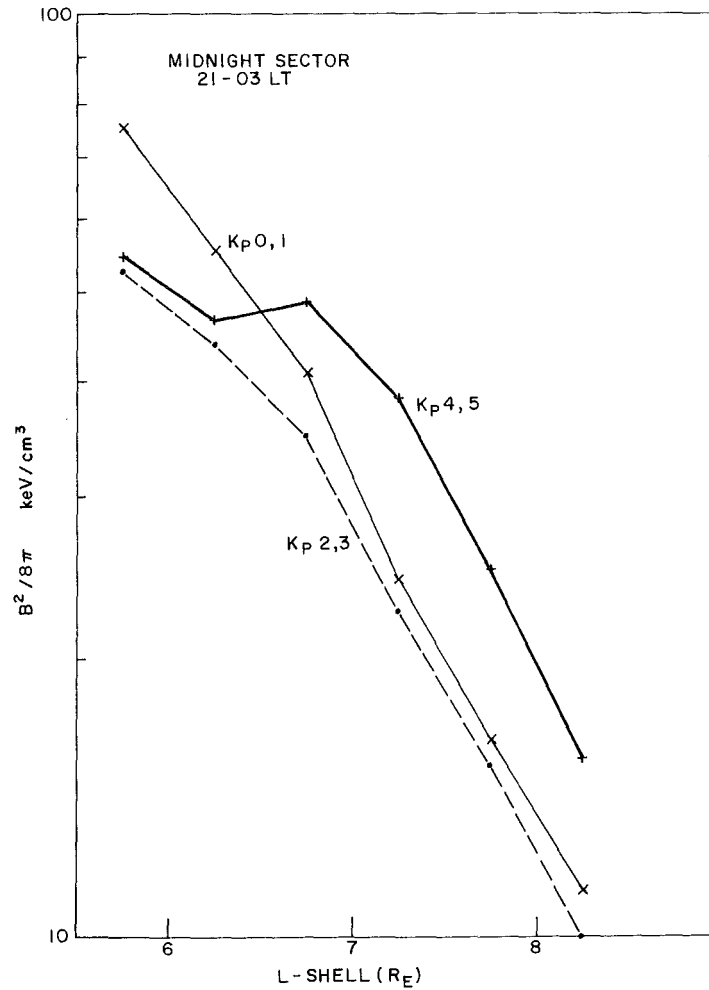


Figure 48. Average Magnetic Field Energy Densities Between 2100-0300 LT vs L-shell for K_P Ranges (x) 0 to 1+, (o) 2- to 3+, and (+) 4- to 5+

magnetic field energy density in keV/cm^3 as a function of L-shell for the noon and midnight sectors, respectively. Each line is representative of a KP range. In the noon sector the energy density falls off monotonically with L from about 70 to $85 \text{ keV}/\text{cm}^3$ at $L = 5.5$ to $6 R_E$ to 15 to $25 \text{ keV}/\text{cm}^3$ at $L = 7.5$ to $8.0 R_E$. At the highest L-values the slope decreases. Although the energy density is inversely related to magnetic activity at the lowest L-values, the variation with KP is not great. The energy density falls as L^{-5} for the KP range 0 to 1+, and more nearly L^{-4} for KP ranges 2- to 3+ and 4- to 5+.

In the midnight sector the energy densities at L values between 5.5 and $6.0 R_E$ are smaller than those in the noon sector for corresponding KP bins. The values range from 52 to $75 \text{ keV}/\text{cm}^3$. Instead of decreasing sharply with L as in the noon sector, there is a more gradual slope to about an L of $6.5 R_E$. In fact, for the KP range 4- to 5+ the energy density increases from 6 to $6.5 R_E$. Beyond $L = 6.5 R_E$ the energy density falls off as approximately L^{-6} for all KP values. The energy density over the entire L-range decreases as magnetic activity increases from the lowest KP range to $KP \geq 2-$ and $\leq 3+$. At $KP \geq 4-$ and $\leq 5+$ the magnetic energy density increases to values exceeding the lowest KP range for L-values beyond $6.5 R_E$. This complicated behavior is probably a result of both diamagnetic and ring current effects. At the highest L-values in the midnight sector the magnetic pressure falls to average values that are equal to or lower than the average particle pressures as given in Section 4. The values reach $15 \text{ keV}/\text{cm}^3$ and below.

6.5 Discussion

The magnetic and particle energy densities (pressures), when taken together, can be used to calculate one of the more important plasma parameters, the plasma beta (β). The plasma β is defined as:

$$\beta = \frac{\text{total energy density}}{\text{total magnetic field energy density}} = \frac{\epsilon_E + \epsilon_I}{B^2/8\pi} \quad (18)$$

where ϵ_E and ϵ_I equal the electron and ion particle energy density, respectively, and B equals the measured magnetic field. As discussed in Section 4.4.2.2, for isotropic plasmas the β defined here is 3/2 the β defined as the ratio of the particle to the magnetic pressure. Figure 49 shows the results of averaging one-spin (~ 58 -sec) values of the plasma β calculated from the SC5 and SC11 data bases over all L values, and plotting β as a function of LT. Separate lines are plotted for the three KP ranges 0 to 1+, 2- to 3+, and 4- to 5+. In the noon sector the average plasma β is between 0.3 and 0.5 and varies little with KP. In the

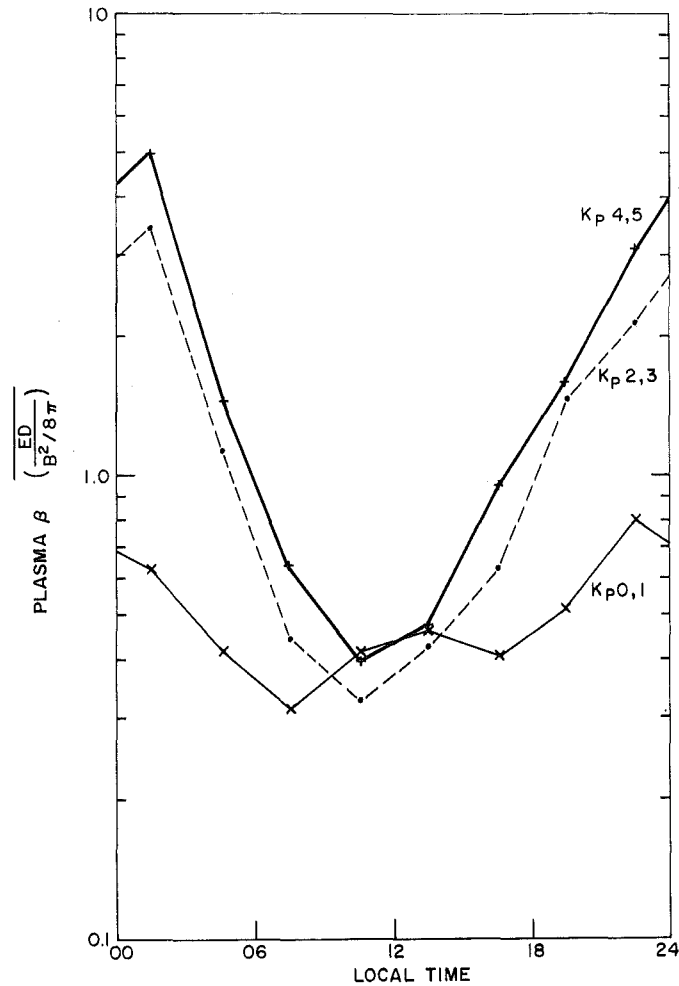


Figure 49. Average plasma β vs LT for KP Ranges (x) 0 to 1+, (o) 2- to 3+, (+) 4- to 5+

midnight sector the average β is less than one ($\beta = 0.6$ to 0.8) for KP levels 0 to 1+. It jumps to values greater than one ($\beta = 2$ to 5) for the KP ranges 2- to 3+ and 4- to 5+. In general, the standard deviations are on the order of the average value of β . Systematic increases in the average β occur with increased magnetic activity for all LTs, except in the noon sector.

Figure 50 shows variations in the average β as a function of L-shell in the noon (a) and midnight (b) sectors. Again, separate lines for each KP range are given. In the noon sector [Figure 50(a)] the variations with L and with KP are small. They range from 0.2 to 0.55. There is some indication that the peak value for β is reached between $L = 6$ and $7.5 R_E$ on the dayside. In the midnight

sector, β increases with both L and with KP . For L between 5.5 and $6 R_E$, the average β is less than one for all KP levels, and for $L = 8$ to $8.5 R_E$ greater than one for all KP levels. For values of $KP \geq 2-$ and $L > 8.0 R_E$, β is greater than 5.

The full dynamic range of β cannot be deduced from the average values and their standard deviations. For this reason, we show in Figure 51 scatter plot of β vs L for periods when KP was between 4- and 5+ in the nightside (1800 to 0600 LT) magnetosphere. We first note that values of β in excess of 100 can be achieved. Second, there appears to be an upper limit on β as a function of L that increases with L . Plots for other KP values (not shown) indicate that the upper bound increases with KP as well. Third, low values of β , less than one and even less than 10^{-1} , can also occur on the nightside. Scatter plots of β in the noon sector show that β rarely exceeds one.

In summary, a comparison of the magnetic energy density and the total particle energy density shows that on the dayside β varies little having values less than one. On the nightside β can vary over three orders of magnitude and increases on the whole with both L -shell and KP . The magnetic pressure itself varies in a complicated manner in the near-geosynchronous region reflecting the presence of local large-scale currents and diamagnetic effects.

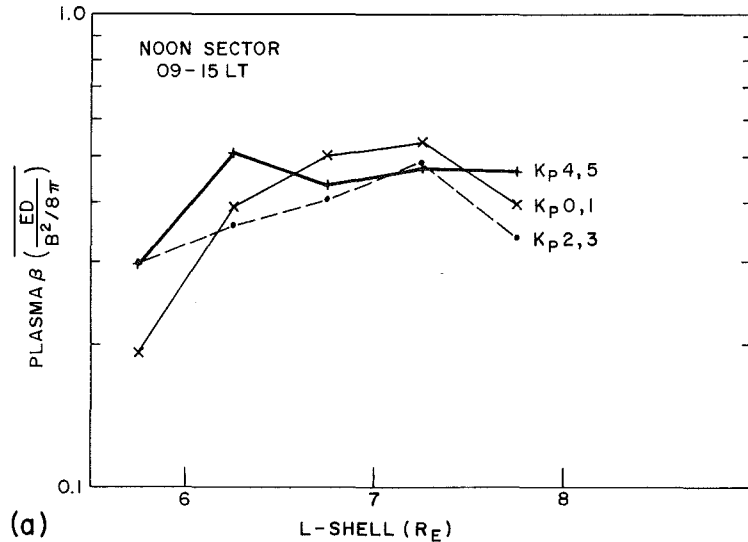


Figure 50. Average Plasma β vs L -shell for KP Ranges (x) 0 to 1+, (o) 2- to 3+, (+) 4- to 5+ in the (a) Noon and (b) Midnight Sectors

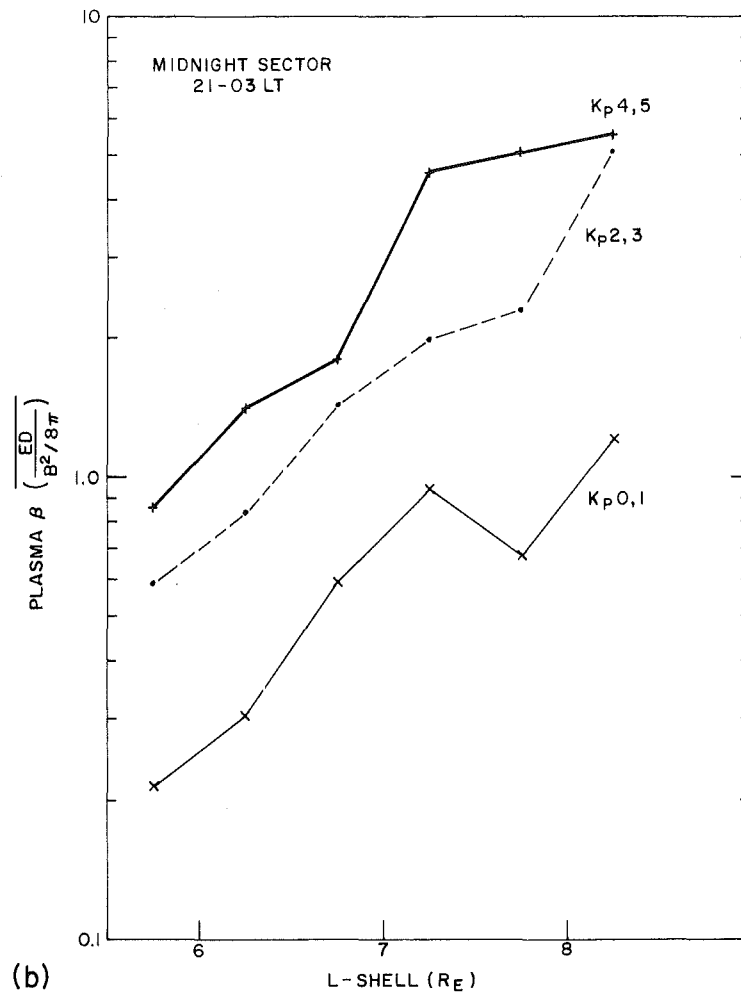


Figure 50. (Contd)

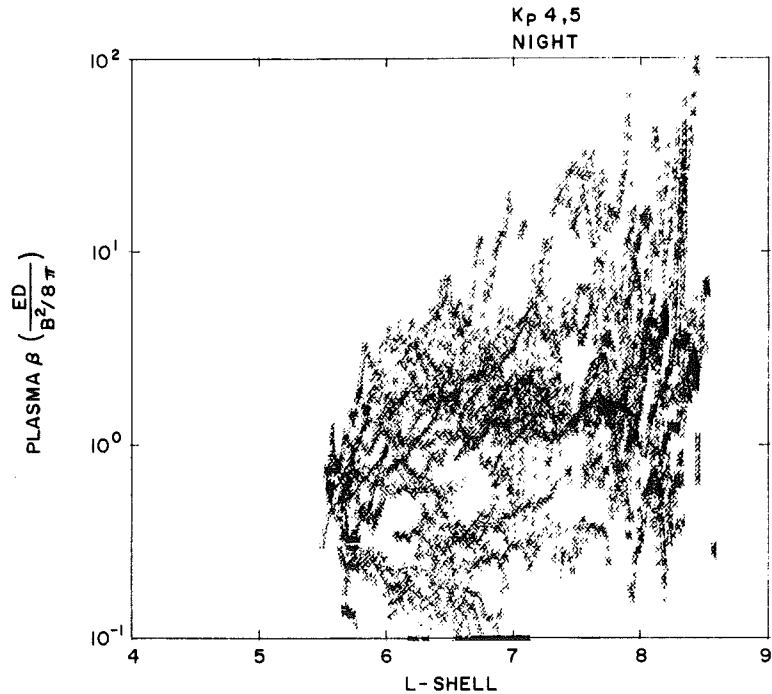


Figure 51. Scatter Plot of β vs L-shell for Periods Kp was $\geq 4-$ and $\leq 5+$ Between 1800 to 0600 LT

7. SC3 HIGH ENERGY ELECTRON RESULTS

The high-energy particle spectrometer known as SC3 on the SCATHA satellite was built and operated under the direction of Dr. J. B. Reagan of the Lockheed Palo Alto Research Laboratory. Some of the SC3 measurements, energetic electrons between 600 keV and 5 MeV, will be discussed in this section.

7.1 Introduction

Knowledge of electrons in the MeV region are of great importance to spacecraft designers and electronic engineers since these high energy electrons provide the major contribution to total radiation dose that is the predominant lifetime determining factor for electronic components of systems operating in the outer radiation belt region of space. To mitigate the degradation and damaging effects of these electrons, design engineers shield sensitive components up to a level where secondary effects begin to dominate. The level of shielding is determined by the expected high energy electron fluence and the desired mission lifetime. Since shielding increases weight, and additional weight reduces capability, it is critical that the high energy electron spectrum is well-defined and well-modeled.

Fluxes of high-energy particles magnetically trapped in the outer radiation belt are in steady-state limited to an upper level above which instabilities created by wave particle interactions create pitch angle scattering of particles into the loss cone. However, during large magnetic storms it is possible for particle fluxes to exceed those for steady-state conditions. Therefore, since the behavior of sensitive electronic devices on space systems depends on dose rate as well as total dose, it is necessary to try to determine an upper flux level as well as an average flux level for the high-energy electrons.

A statistical analysis of the electron fluxes over four energy ranges (634 to 1026, 1026 to 1419, 1419 to 2603, and 2603 to 4970 keV) was performed. The results of the analysis together with short discussions on the instrumentation and data base are given here.

7.2 Instrumentation

The SC3 spectrometer and operation modes are described in detail in Stevens and Vampola¹ and Reagan et al.³⁵ Only a quick overview of experimental details relating to measurements of high-energy electrons will be presented here. The SC3 instrument is a solid-state spectrometer consisting of a long, narrow collimator that defines the 3° field-of-view, a solid-state detector stack of silicon detectors to stop the high-energy electrons and measure their total energy loss, an active anticoincidence collimator operating on high-energy particles that penetrate the detector stack, a plastic scintillator detector viewed by a photomultiplier tube to sense and reject energetic particles and Bremsstrahlung that penetrate the shielding walls, and associated control electronics. The sensors were energy calibrated prior to launch with several radioactive sources, and a weak source was flown on the instrument to monitor any changes in calibrations. The instrument has a 3° (FWHM) pitch angle resolution and a directional geometric factor of $\sim 3 \times 10^{-3} \text{ cm}^2 \text{ sr}$.

On orbit the instrument was programmable to operate in eight different modes, plus a hardwired mode. One of the programmable modes (ELEC2) plus the hardwire mode (BACKUP) collected electron data. However, only the ELEC2 mode data were used here for electrons over the energy range of interest. Characteristics of the SC3 spectrometer in this mode are given in Table 31 taken from Reagan et al.³⁵ The dwell time in each mode was programmable at 8, 16, 32, or 64 sec. This represents approximately 1/8 to 1 full spin period. Of the 12 energy channels only channels 2 through 12 are used here. Data covering the lowest energy channel range is included in the SC5 section.

35. Reagan, J.B., Nightingale, R.W., Gaines, E.E., Imhof, W.L., and Stassinopoulus, E.G. (1981) Outer zone energetic electron spectral measurements, J. Spacecraft Rockets 18:83-88.

Table 31. SC3 ELEC2 Mode Characteristics

Channel	Energy MeV	ΔE MeV	$(G\epsilon\Delta E)^{-1}$ (cm-sr-MeV) ⁻¹
1	0.26-0.63	0.37	1.74×10^3
2	0.63-1.03	0.40	1.05×10^3
3	1.03-1.42	0.39	1.08×10^3
4	1.42-1.81	0.39	1.14×10^3
5	1.81-2.21	0.40	1.22×10^3
6	2.21-2.60	0.39	1.26×10^3
7	2.60-3.00	0.40	1.38×10^3
8	3.00-3.39	0.39	1.48×10^3
9	3.39-3.79	0.40	1.80×10^3
10	3.79-4.18	0.39	2.14×10^3
11	4.18-4.58	0.40	3.25×10^3
12	4.58-4.97	0.39	3.68×10^3

7.3 Data Base

Data were received on computer tapes from Lockheed as 64-sec averages of differential electron fluxes in electrons/cm²-sec-sr-keV within energy ranges of 634 to 1026, 1026 to 1419, 1419 to 2603, and 2603 to 4970 keV. The data base consisted of 74 days of data from day 42, 1979 through day 47, 1980. The days that make up the data base are listed in Table 32. Plots of data from two of the days, day 94 and day 149, 1979 are given in Figures 52 and 53 as examples of days of low and high fluxes, respectively.

The 64-sec averages were calculated for whatever pitch angles the data were collected over and therefore some pitch angle scatter appears in the data set. Because the data were to be used in statistical studies, the data had to be edited to remove spurious values and values when counting levels were felt to be less than background noise levels for the instrument. The flux level where this was determined to occur was somewhere between 10⁻¹ and 10⁻² electrons/cm²-sec-sr-keV. Values at or below 10⁻² were always noise and values at 10⁻¹ were sometimes considered to be noise. Values between 10⁻² and 10⁻¹ were edited by individual day. For example, all data for the 2603 to 4970 keV energy range for day 94 shown in Figure 52 were discarded. The resulting data base was binned in 3-h LT bins, in 0.5 L-shell bins and in KP bins with ranges of 0 to 1+; 2- to 3+; 4- to 5+; and ≥6-. The number of 64-sec flux averages used in the analysis for each bin for each of the four energy channels are given in Tables 33 through 36. The total

Table 32. SC3 Data Base Days

Yr	Day	Yr	Day	Yr	Day
1979	42	1979	142	1979	279
	43		144		280
	44		145		281
	45		146		282
	46		149		301
	47		156		317
	52		157		319
	53		158		328
	78		160		329
	80		166		341
	87		172		351
	88		180		359
	93		188		361
	94		200		363
	95		206	1980	4
	103		225		12
	108		226		18
	110		232		27
	111		241		28
	114		261		36
	115		262		37
	120		264		42
	121		271		46
	127		272		47
	138		278		

number of points available range from 50657 (about 37.5 full days) for the lowest energy channel to 3435 (about 2.5 full days) for the highest energy channel. Because of the low number of data points in the 2603 to 4970 keV channel, the data were not included in the general statistical analysis presented below, except to give an upper flux level observed at low L-shells.

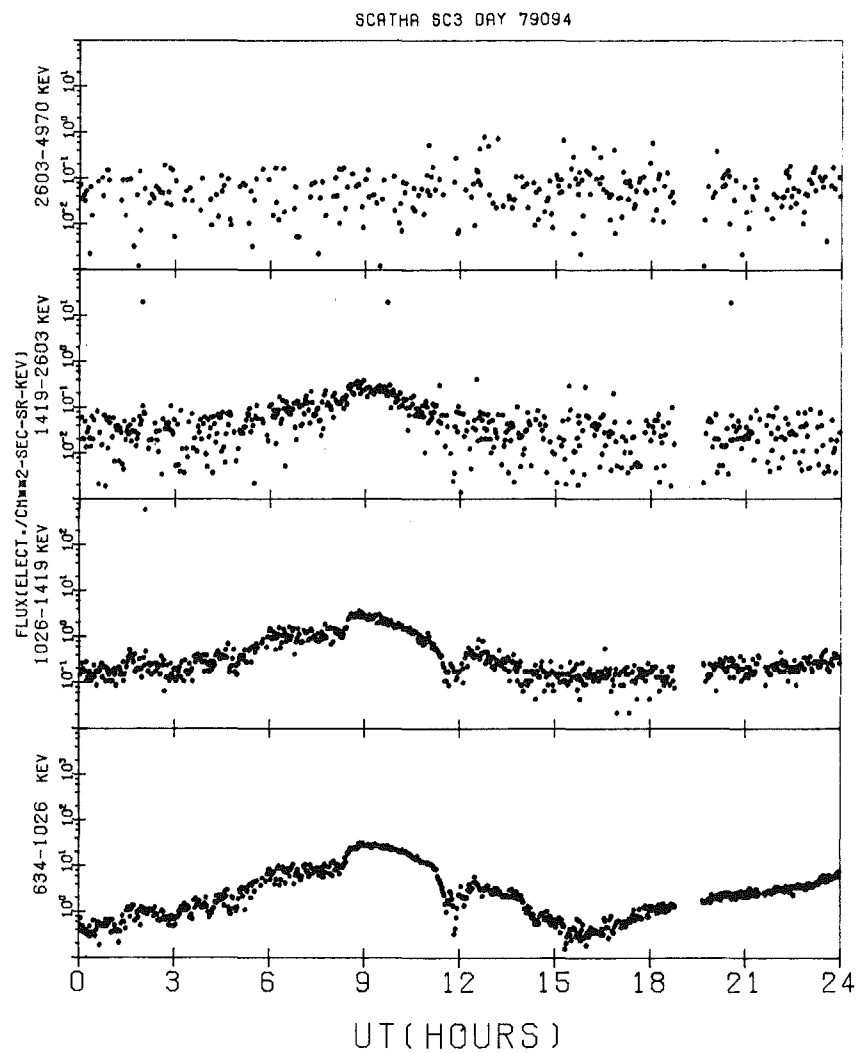


Figure 52. High-energy Electron Fluxes vs LT for Day 94, 1979
(an Example of a Day With Low Flux Levels)

SCATHA SC3 DAY 79149

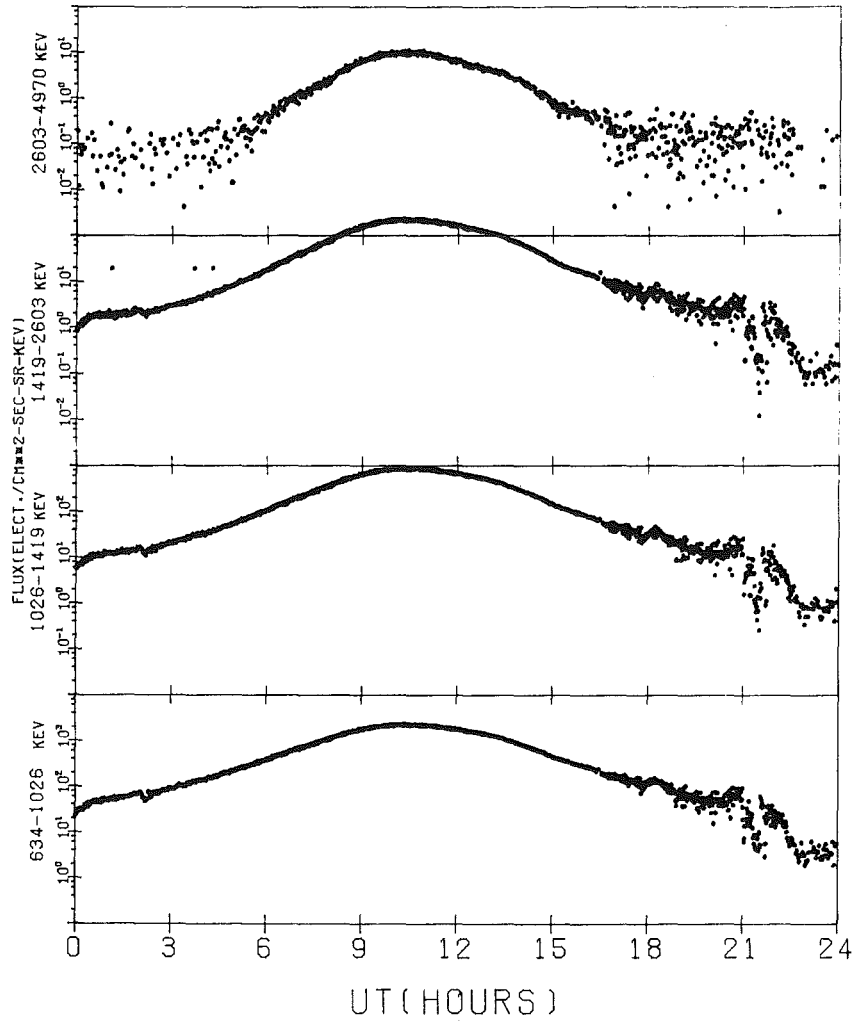


Figure 53. High Energy Electron Fluxes vs UT for Day 149, 1979
(an Example of a Day With High Flux Levels)

Table 33. SC3 634 to 1026 keV Data Set

L-shell (R_E)									
KP 0, 1	5.0-5.5	5.5-6.0	6.0-6.5	6.5-7.0	7.0-7.5	7.5-8.0	8.0-8.5	8.5-9.0	Total
LT									
00-03	0	326	231	131	68	76	327	132	1291
03-06	0	215	186	361	368	363	234	46	1773
06-09	17	240	254	327	672	758	0	0	2268
09-12	73	318	200	308	551	265	0	0	1715
12-15	139	269	216	337	589	19	0	0	1569
15-18	107	186	432	211	158	150	0	0	1244
18-21	2	388	117	145	281	88	38	0	1059
21-24	0	284	184	200	67	176	252	109	1272
24-h total	338	2226	1820	2020	2754	1895	851	287	12191
KP 2, 3									
00-03	0	165	200	138	210	505	990	209	2417
03-06	0	252	151	237	357	448	440	11	1896
06-09	11	393	254	233	569	547	13	0	2020
09-12	213	614	542	573	554	284	0	0	2785
12-15	461	705	397	677	631	95	0	0	2966
15-18	329	621	477	256	387	816	35	0	2921
18-21	4	778	407	311	246	330	590	72	2738
21-24	0	440	148	310	238	347	472	132	2087
24-h total	1023	3968	2576	2735	3192	3372	2540	424	19830
KP 4, 5									
00-03	0	234	293	225	179	138	509	138	1716
03-06	0	385	172	318	324	436	479	0	2114
06-09	0	366	177	181	738	695	11	0	2168
09-12	11	248	407	275	415	247	0	0	1603
12-15	132	313	212	258	415	0	0	0	1330
15-18	38	549	144	88	276	340	3	0	1438
18-21	0	410	325	278	248	161	441	79	1942
21-24	0	393	125	250	404	517	373	111	2173
24-h total	181	2898	1855	1873	2999	2534	1816	328	14484
KP >6-									
00-03	0	1	61	179	154	167	386	13	961
03-06	0	82	44	41	103	120	210	0	600
06-09	29	85	0	24	80	124	0	0	342
09-12	0	118	181	74	42	0	0	0	415
12-15	18	88	39	134	85	0	0	0	364
15-18	50	27	74	59	94	80	0	0	384
18-21	0	179	68	0	0	73	71	0	391
21-24	0	58	34	96	117	187	203	0	695
24-h total	97	638	501	607	675	751	870	13	4152

Table 34. SC3 1026 to 1419 keV Data Set

L-shell (R_E)									
KP 0,1	5.0-5.5	5.5-6.0	6.0-6.5	6.5-7.0	7.0-7.5	7.5-8.0	8.0-8.5	8.5-9.0	Total
<u>LT</u>									
00-03	0	326	231	131	68	76	322	122	1276
03-06	0	215	186	360	368	361	226	46	1762
06-09	17	240	254	327	672	759	0	0	2269
09-12	73	318	200	309	548	263	0	0	1711
12-15	139	269	216	337	589	19	0	0	1569
15-18	107	186	432	211	158	150	0	0	1244
18-21	2	388	117	145	283	88	39	0	1062
21-24	0	284	184	200	67	178	248	109	1270
24-h total	338	2226	1820	2020	2753	1894	835	277	12163
<u>KP 2,3</u>									
00-03	0	165	200	138	210	505	935	200	2353
03-06	0	252	151	237	357	447	436	11	1891
06-09	11	393	254	233	569	545	13	0	2018
09-12	218	614	542	574	554	284	0	0	2786
12-15	461	705	397	677	631	95	0	0	2966
15-18	329	621	477	256	387	816	35	0	2921
18-21	4	777	407	311	246	323	584	72	2724
21-24	0	440	148	310	238	347	471	132	2086
24-h total	102	3967	2576	2736	3192	3362	2474	415	19745
<u>KP 4,5</u>									
00-03	0	234	292	226	179	137	507	138	1713
03-06	0	385	172	318	324	435	478	0	2112
06-09	0	386	177	181	738	689	11	0	2162
09-12	11	248	408	275	415	246	0	0	1603
12-15	132	313	212	258	415	0	0	0	1330
15-18	38	549	144	88	276	340	3	0	1438
18-21	0	410	325	278	248	161	441	78	1941
21-24	0	394	124	250	405	513	372	110	2168
24-h total	181	2899	1854	1874	3000	2521	1812	326	14467
<u>KP >6-</u>									
00-03	0	1	61	180	154	166	385	13	960
03-06	0	82	44	41	103	120	210	0	600
06-09	29	85	0	24	80	124	0	0	342
09-12	0	118	179	69	42	0	0	0	408
12-15	18	88	39	133	85	0	0	0	363
15-18	50	27	74	59	94	79	0	0	383
18-21	0	179	68	0	0	73	70	0	390
21-24	0	58	34	96	117	187	203	0	695
24-h total	97	638	499	602	675	749	868	13	4141

Table 35. SC3 1419 to 2603 keV Data Set

L-shell (R_E)									
KP 0,1	5.0-5.5	5.5-6.0	6.0-6.5	6.5-7.0	7.0-7.5	7.5-8.0	8.0-8.5	8.5-9.0	Total
<u>LT</u>									
00-03	0	326	231	131	68	76	262	95	1189
03-06	0	215	185	360	363	317	202	40	1682
06-09	17	240	254	320	655	707	0	0	2193
09-12	73	318	200	308	502	261	0	0	1662
12-15	139	269	216	334	550	19	0	0	1527
15-18	107	186	432	211	147	150	0	0	1233
18-21	2	388	117	144	270	74	34	0	1029
21-24	0	284	184	197	60	161	222	72	1180
24-h total	338	2226	1819	2005	2615	1765	720	207	11695
<u>KP 2,3</u>									
00-03	0	164	199	136	198	458	823	148	2126
03-06	0	252	151	231	339	409	390	9	1781
06-09	11	393	254	230	537	446	11	0	1882
09-12	218	615	540	573	504	225	0	0	2675
12-15	461	705	393	662	545	90	0	0	2856
15-18	329	621	477	254	354	733	35	0	2803
18-21	4	778	407	304	218	279	469	61	2520
21-24	0	440	148	309	229	301	364	93	1883
24-h total	1023	3968	2569	2699	2923	2941	2092	311	18526
<u>KP 4,5</u>									
00-03	0	234	290	206	163	121	470	117	1601
03-06	0	383	163	301	286	336	395	0	1864
06-09	0	366	177	177	642	583	11	0	1956
09-12	11	248	408	273	325	178	0	0	1443
12-15	132	311	212	232	344	0	0	0	1231
15-18	38	548	142	88	235	212	3	0	1266
18-21	0	410	320	253	200	118	324	58	1683
21-24	0	394	121	236	382	435	316	82	1966
24-h total	181	2894	1833	1766	2577	1983	1519	257	13010
<u>KP >6-</u>									
00-03	0	1	60	164	114	102	337	13	791
03-06	0	82	44	37	87	98	147	0	495
06-09	29	85	0	22	68	112	0	0	316
09-12	0	118	164	62	27	0	0	0	371
12-15	18	88	38	90	63	0	0	0	297
15-18	50	27	56	47	65	52	0	0	298
18-21	0	174	67	0	0	53	54	0	348
21-24	0	58	34	90	91	161	156	0	590
24-h total	97	633	463	512	516	578	694	13	3506

Table 36. SC3 2603 to 4970 keV Data Set

L-shell (R_E)									
KP 0,1	5.0-5.5	5.5-6.0	6.0-6.5	6.5-7.0	7.0-7.5	7.5-8.0	8.0-8.5	8.5-9.0	Total
LT									
00-03	0	0	0	0	0	0	0	0	0
03-06	0	35	0	0	0	0	0	0	35
06-09	0	88	80	18	0	0	0	0	186
09-12	25	135	11	0	0	0	0	0	171
12-15	49	45	0	0	0	0	0	0	94
15-18	0	28	51	0	0	0	0	0	79
18-21	0	52	6	0	0	0	0	0	7
21-24	0	7	0	0	0	0	0	0	74
24-h total	74	390	148	18	0	0	0	0	130
KP 2,3									
00-03	0	8	27	0	0	0	0	0	35
03-06	0	47	0	0	0	0	0	0	47
06-09	0	173	0	0	0	0	0	0	173
09-12	92	232	27	0	0	0	0	0	351
12-15	221	252	23	0	0	0	0	0	496
15-18	28	429	56	0	0	0	0	0	513
18-21	0	97	91	39	3	0	0	0	230
21-24	0	50	3	22	0	0	0	0	75
24-h total	341	1288	227	61	3	0	0	0	1920
KP 4,5									
00-03	0	0	0	0	0	0	0	0	0
03-06	0	28	0	0	0	0	0	0	28
06-09	0	0	0	0	0	0	0	0	0
09-12	0	45	42	0	0	0	0	0	87
12-15	106	143	22	0	0	0	0	0	271
15-18	38	240	4	0	0	0	0	0	282
18-21	0	92	27	0	0	0	0	0	119
21-24	0	42	0	0	0	0	0	0	42
24-h total	144	590	95	0	0	0	0	0	829
KP >6-									
00-03	0	0	0	0	0	0	0	0	0
03-06	0	0	0	0	0	0	0	0	0
06-09	0	0	0	0	0	0	0	0	0
09-12	0	0	0	0	0	0	0	0	0
12-15	7	0	0	0	0	0	0	0	7
15-18	48	1	0	0	0	0	0	0	49
18-21	0	0	0	0	0	0	0	0	0
21-24	0	0	0	0	0	0	0	0	0
24-h total	55	1	0	0	0	0	0	0	56

7.4 Data Analysis

After establishing an edited data base, the data were first scatter plotted as flux vs L-shell, flux vs KP, flux vs magnetic latitude, and flux vs LT for each of the four energy ranges. The plots of the fluxes for each of the four energy ranges vs L-shell are shown in Figures 54 to 56. The +'s and dashed lines will be explained later and should be disregarded for now. In all four of the figures a marked downward trend in flux with increasing L can be seen. This L-shell dependence so dominates the fluxes that no KP, magnetic latitude, or LT variations could be seen in their scatter plots. To confirm this, flux averages (of the 64-sec average values) in bins of 0.5L, 3-h LT, and KP ranges 0 to 1+; 2- to 3+; 4- to 5+; and ≥ 6 - were calculated. The results of the averaging showed that compared to the L-shell changes, KP and LT changes (if any) were small. Since KP gave the smallest variations, the data base was again averaged over bins but this time in 0.5L, 3-h LT and all KP. The eight 3-h LT bins averages were then averaged to get a total L average for each energy range. The resulting averages are given in Table 37 and plotted on Figures 54 to 56 as +'s. As mentioned earlier no averaging of the 2603 to 4970 keV data was done because of the cutoff level of the instrument.

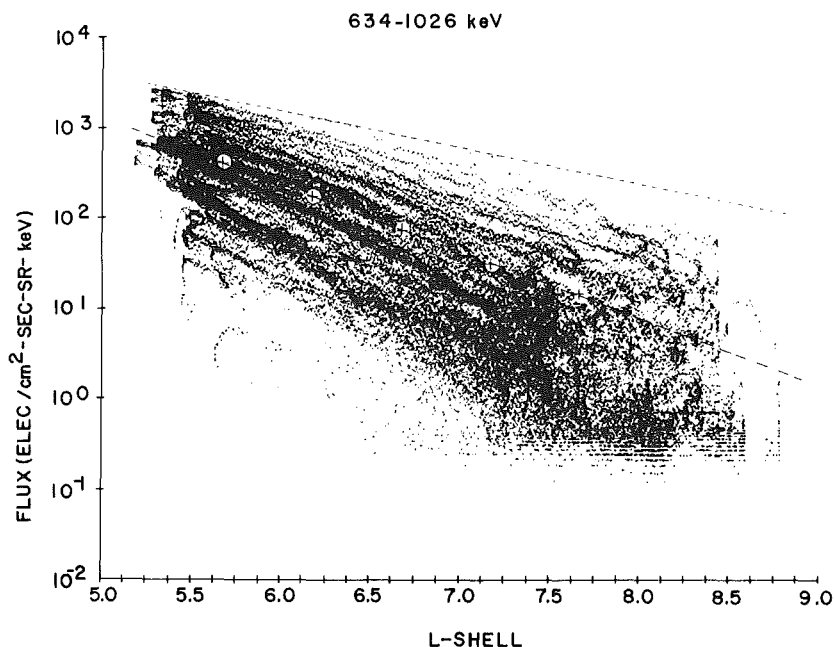


Figure 54. Scatter Plot of the Log of the 634 to 1026 keV Flux Values vs L-shell for the SC3 Data Set. Included are the mean values (+'s) in 0.5 L-shell bins, the mean linear fit (lower dashed line), and the upper envelope straight line projection (upper dashed line)

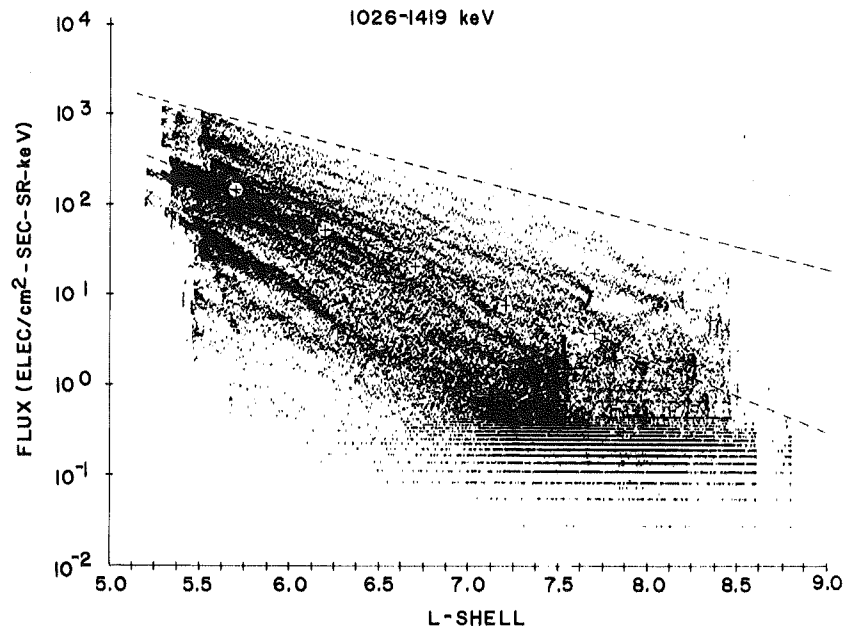


Figure 55. Scatter Plot of the Log of the 1026 to 1419 keV Flux Values vs L-shell for the SC3 Data Set. Included are the mean values (+'s) in 0.5 L-shell bins, the mean linear fit (lower dashed line), and the upper envelope straight line projection (upper dashed line)

Table 37. Average High Energy Electron Fluxes

E (keV)	L-Shell (R_E)				
	5.75	6.25	6.75	7.25	7.75
634-1026	379*	159	68.1	28.5	12.9
1026-1419	108	40.1	15.6	6.05	2.73
1419-2603	18.7	6.05	2.20	0.846	0.449

* All values are in electrons/cm²-sec-sr-keV.

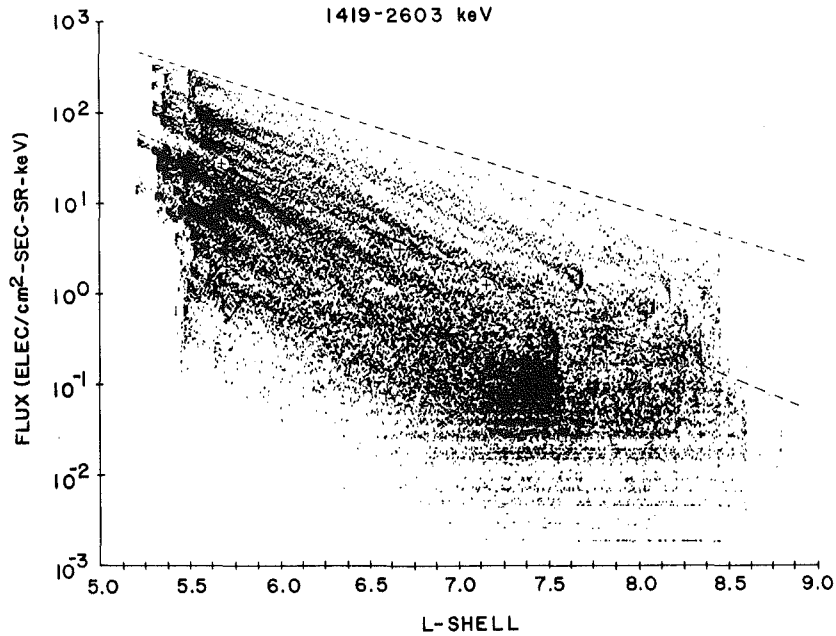


Figure 56. Scatter Plot of the Log of the 1419 to 2603 keV Flux Values vs L-shell for the SC3 Data Set. Included are the mean values (+'s) in 0.5 L-shell bins, the mean linear fit (lower dashed line), and the upper envelope straight line projection (upper dashed line)

The \log_{10} of the average fluxes given in Table 37 were then least squares fit against \bar{L} for each of the three energy ranges to determine the relationship between flux (J) and L. The results are:

$$E = 634 \text{ to } 1026 \text{ keV} \quad \log_{10} J = 6.8 - 0.74L \quad (19)$$

$$E = 1026 \text{ to } 1419 \text{ keV} \quad \log_{10} J = 6.6 - 0.80 L \quad (20)$$

$$E = 1419 \text{ to } 2603 \text{ keV} \quad \log_{10} J = 5.9 - 0.82L \quad (21)$$

The line fits of these equations are plotted on Figures 54 through 56 as the lower dashed lines. The correlation coefficients for all three fits exceeded 0.99. A second dashed line was then drawn as an upper envelope for all four of the scatter plots and the equations of the straight lines determined by measuring two points on the lines. The results are:

$$E = 634 \text{ to } 1026 \text{ keV} \quad \log_{10} J = 5.6 - 0.42L \quad (22)$$

$$E = 1026 \text{ to } 1419 \text{ keV} \quad \log_{10} J = 5.6 - 0.49L \quad (23)$$

$$E = 1419 \text{ to } 2603 \text{ keV} \quad \log_{10} J = 5.7 - 0.61L \quad (24)$$

$$E = 2603 \text{ to } 4970 \text{ keV} \quad \log_{10} J = 5.4 - 0.80L \quad (25)$$

Vampola et al³⁶ among others has shown that a power law relationship of the form

$$J = AE^k, \quad (26)$$

where J = high-energy electron flux in electrons/cm²-sec-sr-keV, and E = energy in MeV exists for a given L . A least squares power law fit to the flux values for each L in Table 37 using average energies of 0.83, 1.2225, and 2.011 MeV gives energy spectra coefficients A and k listed in Table 38. The points and resulting fits are shown in Figure 58 as x's and dashed lines, respectively. Again all the correlation coefficients for the fits exceeded 0.99.

Table 38. SC3 Average Energy Spectra Coefficients

L	A	k
5.75	206	-3.41
6.25	81.4	-3.70
6.75	33.4	-3.88
7.25	13.5	-3.97
7.75	6.18	-3.78

Another way to look at the data is in cumulative distributions which show the percent of time the flux falls below a given level. Figures 59 through 61 give the cumulative distributions in four L ranges for the high-energy electron fluxes in the three energy ranges 634 to 1026, 1026 to 1419, and 1419 to 2603 keV, respectively. The bin sizes are 10^p to 2.5×10^p , 2.5×10^p to 5.0×10^p , 5.0×10^p to 7.5×10^p , and 7.5×10^p to $1.0 \times 10^{p+1}$, where p equals the power of 10.

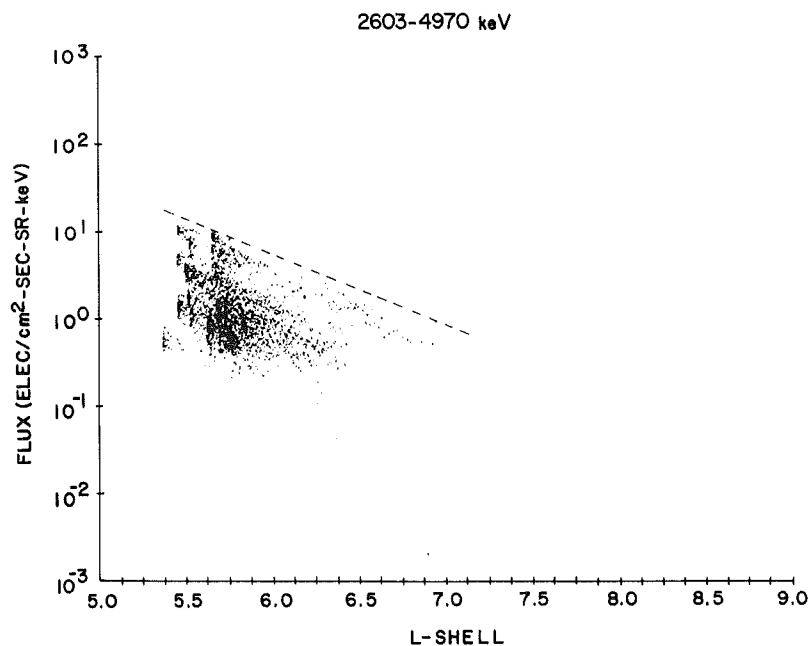


Figure 57. Scatter Plot of the Log of the 2603 to 4970 keV Flux Values vs L-shell for the SC3 Data Set. Included is the upper envelope straight line projection (upper dashed line)

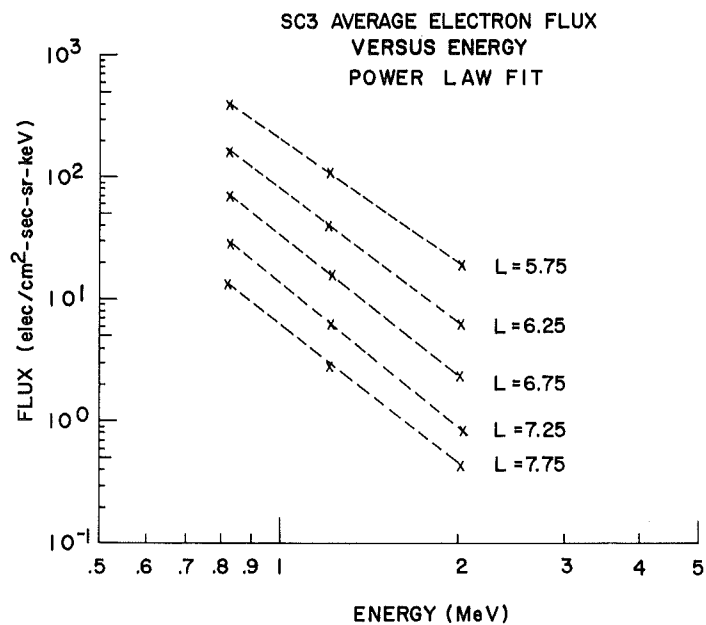


Figure 58. Power Law Fits of Average SC3 Electron Fluxes at L-shells From 5.75 -7.75 R_E

**SC3 HIGH ENERGY ELECTRON
CUMULATIVE DISTRIBUTIONS
(634-1026 keV)**

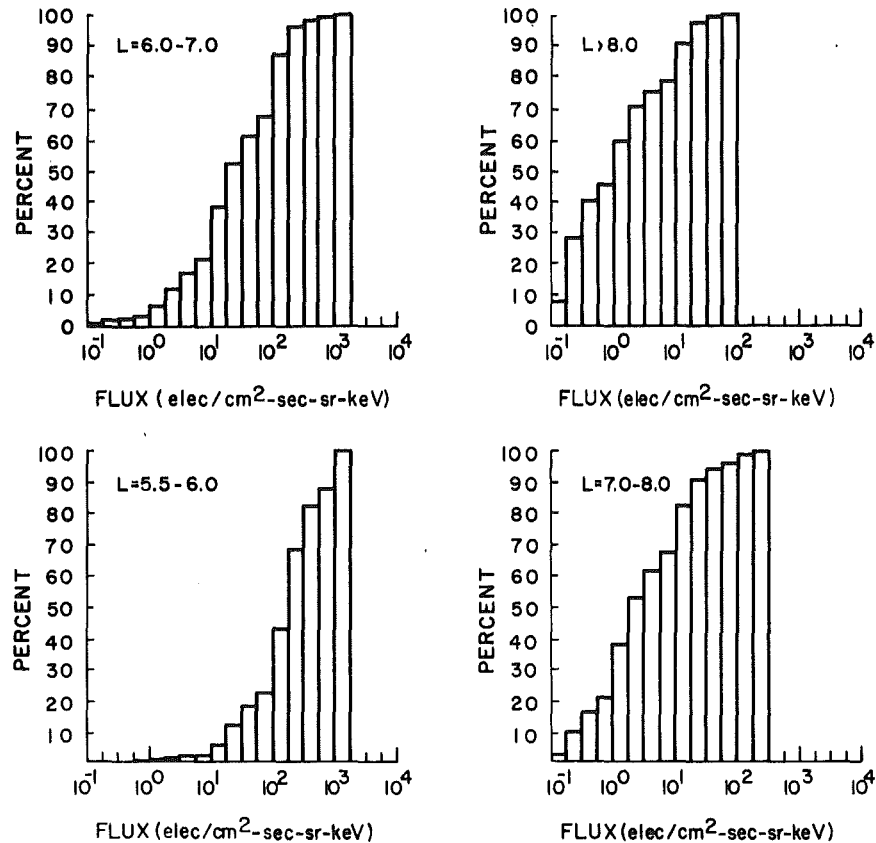


Figure 59. SC3 High-energy Electron Flux Cumulative Distributions for 0.5 L-shell Ranges for Energies 634 to 1026 keV

7.5 Discussion

From the scatter plots (Figures 54 through 56) it can be seen that high-energy electron flux values near-geosynchronous altitude can vary over several orders of magnitude over the period of a year. Although average models of high-energy electrons can be constructed, they do not accurately reflect the rate at which the particles interact with electronic components on spacecraft, and therefore may be misleading in predicting degradation due to accelerated dose rates. In the area of total fluence, average models can give representative numbers, but self-healing (annealing) of certain electronic devices can only be considered if cumulative distributions such as those shown in Figures 58 through 61 are also included in the calculations.

SC3 HIGH ENERGY ELECTRON
CUMULATIVE DISTRIBUTIONS
(1026-1419 keV)

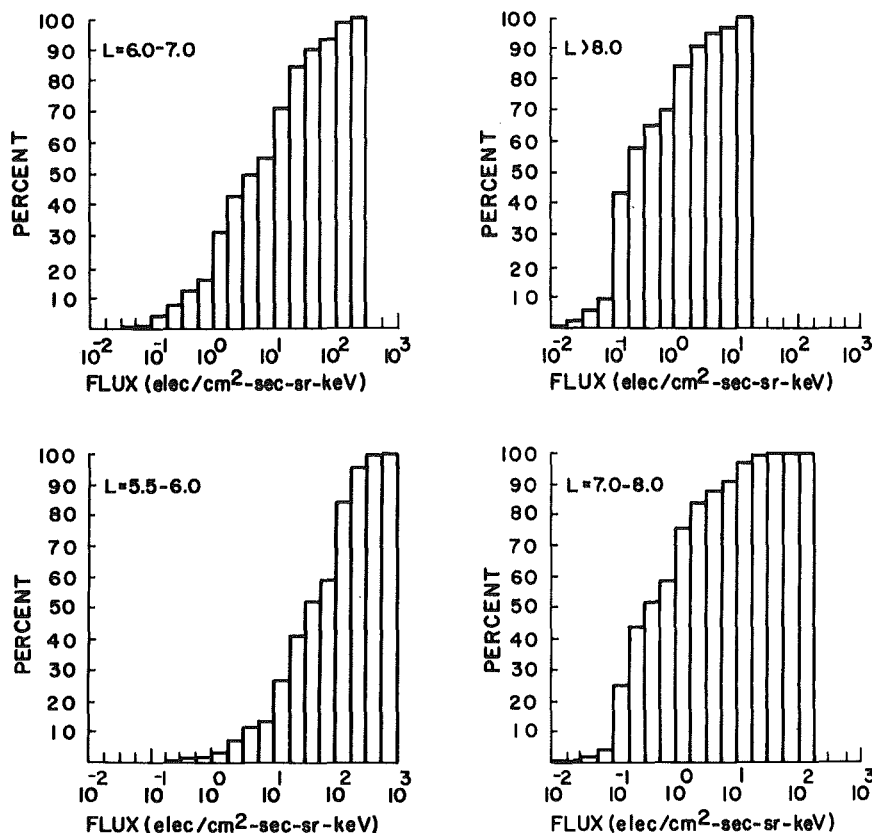


Figure 60. SC3 High-energy Electron Flux Cumulative Distributions for 0.5 L-shell Ranges for Energies 1026 to 1419 keV

Comparisons of results from this data set with others such as the OV1-19 results of Vampola et al³⁶ and the AE-4 Model of Singley and Vette³⁷ is not straightforward. First, no attempt was made in this data set to determine omnidirectional fluxes. Second, since the purpose of SCATHA was to investigate spacecraft charging, this data set contains a higher than average percentage of storm days. Third, solar cycle and time within the solar cycle have to be

36. Vampola, A.L., Blake, J.B., and Paulikas, G.A (1977) A New Study of the Outer Zone Electron Environment: A Hazard to CMOS, SAMSO-TR-77-127, 26 pp.

37. Singley, G.W., and Vette, J.I. (1972) The AE-4 Model of the Outer Radiation Zone Electron Environment, NSSDC 72-06.

SC3 HIGH ENERGY ELECTRON
CUMULATIVE DISTRIBUTIONS
(1419-2603 KeV)

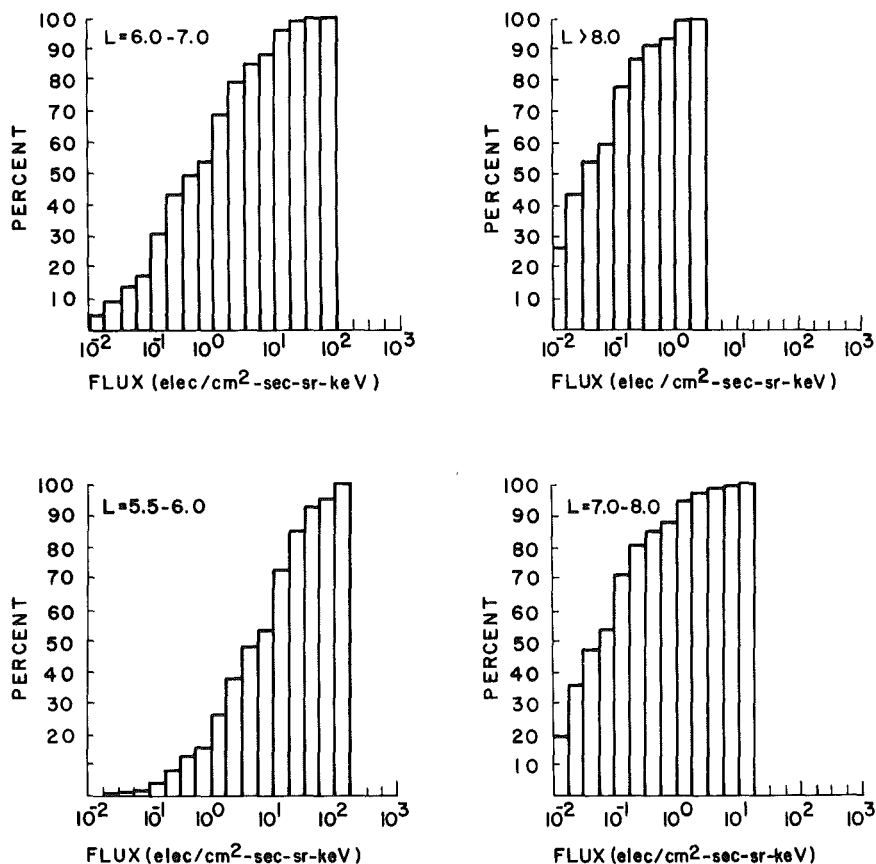


Figure 61. SC3 High-energy Electron Flux Cumulative Distributions for 0.5 L-shell Ranges for Energies 1419 to 2603 keV

considered. Given all the various parameters needed to be considered to try and equate different data sets, only qualitative differences will be discussed.

Figure 5 of Reagan et al³⁵ showed relatively good agreement between the AE-4 Model and SC-3 data between 500 keV and 4 MeV for the period from 31 January to 2 February 1979. Over the range from 500 keV to 2.5 MeV average fluxes from this study are consistently lower than the AE-4 model over the entire L-range from 5.75 to 7.75 R_E. The high fluxes, however, are always higher than the model and sometimes by more than an order of magnitude. Gaines et al³⁸ used

38. Gaines, E.E., Nightingale, R.W., Imhof, W.L., and Reagan, J.B. (1981) Enhanced radiation doses to high-altitude spacecraft during June 1980, IEEE Trans. Nucl. Sci. NS-28:4502.

SC3 high-energy electron fluxes during a very high energetic electron flux period from 9 to 14 June 1980, to calculate dose levels and compare them to dose levels from the AE-4 Model as a function of energy and shield penetration. They concluded that "short term effects such as charging and subsequent discharge in dielectrics from the accumulations stopped in the material in a period of the order of a day are more likely than total dose damage over the few days duration of high flux levels." Therefore, designers of space systems that will use sensitive electronic devices in the near-geosynchronous regions of space should carefully consider effects due to the higher flux levels that can be calculated from Eqs. (22) through (25).

8. SUMMARY

Since spacecraft charging was first discovered to have deleterious effects on space vehicles operating in the near-Earth space regime, there has been a need to define the environmental parameters, particle populations, etc., necessary to adequately design and test space systems in order to mitigate charging effects. To develop a statistical specification of the geosynchronous plasma environment prior to the launch of SCATHA, Garrett et al^{39, 40} used ATS-5 and ATS-6 data to define an average plasma environment between 30 eV and 100 keV. With the launch of SCATHA, efforts were made to update and expand previous studies of the plasma environment. Since spacecraft design engineers needed an upper limit or "worst case" environment to define test levels, initial studies concentrated on high-level charging periods. These earlier studies resulted in two reports by Mullen et al^{41, 18} which identified the particle populations critical to spacecraft charging, presented results of a high-level charging statistical study, and gave measured distribution functions of the electron and ion populations during "worst case" charging events. The two reports, one of which is summarized in Appendix D, provide supplemental information to the atlas.

The middle energy ion and electron analyses presented in Section 4 show LT, L-shell, and KP dependence of various energy particle fluxes, moments of the

-
39. Garrett, H.B., Schwank, D.C., and DeForest, S.E. (1981a) A statistical analysis of the low-energy geosynchronous plasma environment - I. Electrons, Planet Space Sci. 29:1021.
 40. Garrett, H.B., Schwank, D.C., and DeForest, S.E. (1981b) A statistical analysis of the low-energy geosynchronous plasma environment - II. Ions, Planet Space Sci. 29:1045.
 41. Mullen, E.G., Gussenhoven, M.S., and Garrett, H.B. (1981) A "Worst Case" Spacecraft Environment as Observed by SCATHA on 24 April 1979, AFGL-TR-81-0231, AD A108680.

distribution function, and particle anisotropies in magnetic pitch angle. The SC5 average total electron moments when compared to the results of Garrett et al³⁹ agree remarkably well both in variation and in absolute level. The SC5 average total ion moments, however, when compared to the results of Garrett et al⁴⁰ have consistently higher absolute values for the higher moments. A possible explanation for this is the increased energy range (400 as compared to 100 keV) of the SC5 detector. There are quantitative differences in calculating high and low densities by the moment technique, as done here, and by assuming two Maxwellians, as done by Garrett et al, but each show similar relative variations with LT, L-shell, and KP. We, again, stress the fact that the two-Maxwellian representation does not adequately represent the distribution functions during high level charging periods, and using the moments to derive n_1 , n_2 , T_1 , and T_2 can provide misleading results (Mullen et al⁴¹).

The SC8 analysis of ion composition, given in Section 5, shows that the values of $n(O^+)$, $n(H^+)$, and $n(O^+)/n(H^+)$ have significant average variations with LT, L-shell, and KP. The hydrogen and oxygen average densities behave differently with L-shell, and the oxygen density exceeds the hydrogen density on the average for KP levels ≥ 6 -. Anomalous behavior in $n(O^+)$ was found for low KP and low L values. Results of the study done here agree well with the GEOS 2 results for Young et al²⁹ where the studies overlap. In addition to the statistical studies, the SC8 ion composition data were used to correct the SC5 ion measurements in Appendix B.

The SC11 magnetometer data presented in Section 6 shows that the Olson-Pfitzer magnetic field model is well-suited for use at SCATHA altitude under quiet magnetic conditions. It was also shown that the model gives a good baseline for studying variations during active periods. The plasma β was calculated from the SC5 total energy density ($\epsilon_I + \epsilon_E$) and the magnetic field pressure ($B^2/8\pi$) and statistically analyzed. The plasma β depends on LT, L-shell, and KP and ranges over more than three orders of magnitude from values less than 0.1 to greater than 100.

The SC3 high-energy electron analyses given in Section 7 show the high variability in the outer radiation belt particles. Power law fits to the fluxes for given L-ranges were derived that model the average fluxes but do not describe the several orders of magnitude variability seen in the data. Cumulative distributions of flux were calculated to show the percentage of time high flux levels can be expected. Models of the variations of average flux and the upper limit on the flux as a function of L-shell are given. These can be used for high-energy electron dose rate calculations.

Appendix C gives the results of a study of the 40-keV trapping region conducted by J. Feynman of Boston College. The results are of interest in that a composite

coordinate system between SM and GSM coordinates was found to order particle dropout regions near-geosynchronous orbit. This coordinate system may eventually be found to better order many data sets in this region of space.

In conclusion, the atlas contains numerous tables and figures of analyzed data that well represent the plasma environment near-geosynchronous orbit. The data have been presented in table form so they can be easily used by modelers, test engineers, etc. The somewhat exhaustive descriptions of the data sets were included to allow each user to determine any limitations for his particular use of the data. The results provide the necessary environmental data to support spacecraft charging test standards.

References

1. Stevens, J.R., and Vampola, A.L., Eds. (1978) Description of the Space Test Program P78-2 Spacecraft and Payloads, SAMSO TR-78-24, 59 pp.
2. DeForest, S.E. (1972) Spacecraft charging at synchronous orbit, J. Geophys. Res. 77:651.
3. Chappell, C.R. (1972) Recent satellite measurements of the morphology and dynamics of the plasmasphere, Rev. Geophys. Space Phys. 10:951.
4. Lennartsson, W., and Reasoner, D.L. (1978) Low-energy plasma observations at synchronous orbit, J. Geophys. Res. 83:2145.
5. Schulz, M. (1980) Energetic particle populations and cosmic-ray entry, J. Geomag. Geoelec. 32:507.
6. Schulz, M. (1982) Earth's radiation belts, Rev. Geophys. Space Phys. 20:613.
7. Frank, L.A. (1971) Relationship of the plasma sheet, ring current, trapping boundary, and plasma pause near the magnetic equator and local midnight, J. Geophys. Res. 76:2265.
8. Olsen, R.C. (1981) Equatorially trapped plasma populations, J. Geophys. Res. 86:11235.
9. Aggson, T. (1980) Private communication.
10. Quinn, J.M., and Johnson, R.G. (1982) Composition measurements of warm equatorially trapped ions near geosynchronous orbit, Geophys. Res. Lett. 9:777-780.
11. Ejiri, M. (1978) Trajectory traces of charged particles in the magnetosphere, J. Geophys. Res. 83:4798.
12. McIlwain, C.E. (1972) Plasma convection in the vicinity of the geosynchronous orbit, in Earth's Magnetospheric Processes, B.M. McCormac, Ed., D. Reidel, Hingham, Mass., p. 268.
13. Volland, H.A. (1973) A semiempirical model of large-scale magnetospheric electric fields, J. Geophys. Res. 78:171.

14. Stern, D. P. (1975) The motion of a proton in the equatorial magnetosphere, J. Geophys. Res. 80:595.
15. Hanser, F. A., Hardy, D. A., and Sellers, B. (1979) Calibration of the Rapid Scan Particle Detector Mounted in the SCATHA Satellite, AFGL-TR-79-0167, AD A082382.
16. Mullen, E. G., Garrett, H. B., Hardy, D. A., and Whipple, E. C. (1980) P78-2 SCATHA Preliminary Data Atlas, AFGL-TR-80-0241, AD A094122.
17. Kaye, S. M., Lin, C. S., Parks, G. K., and Winckler, J. R. (1978) Adiabatic modulation of equatorial pitch angle anisotropy, J. Geophys. Res. 83:2675.
18. West, H. I., Jr. (1979) The signatures of the various regions of the outer magnetosphere in the pitch angle distributions of energetic particles, in Quantitative Modeling of Magnetospheric Processes, W. P. Olson, Ed., American Geophysical Union, Washington, D. C., p. 150.
19. Mullen, E. G., and Gussenhoven, M. S. (1982) High Level Spacecraft Charging Environments Near Geosynchronous Orbit, AFGL-TR-82-0063, AD A118791.
20. Laframboise, J. G., Godard, R., and Kamitsuma, M. (1982) Multiple floating potentials, "threshold-temperature" effects and "barrier" effects in high-voltage charging of exposed surfaces on spacecraft, in Proceedings International Symposium on Spacecraft Materials in Space Environment, Toulouse, France, 8-11 June 1982 (to be published).
21. Shelley, E. G. (1979) Heavy ions in the magnetosphere, Space Sci. Rev. 23:465.
22. Johnson, R. G. (1979) Energetic ion composition in the earth's magnetosphere, Rev. Geophys. Space Phys. 17:696.
23. Geiss, J., Balsiger, H., Eberhardt, P., Walker, H. P., Weber, L., and Young, D. T. (1978) Dynamics of magnetospheric ion composition as observed by the GEOS mass spectrometer, Space Sci. Rev. 22:537.
24. Peterson, W. K., Sharp, R. D., Shelley, E. G., Johnson, R. G. (1981) Energetic ion composition of the plasma sheet, J. Geophys. Res. 86:761.
25. Lennartsson, W., Sharp, R. D., Shelley, E. G., Johnson, R. G., and Balsiger, H. (1981) Ion composition and energy distribution during 10 magnetic storms, J. Geophys. Res. 86:4628.
26. Sharp, R. D., Carr, D. L., Peterson, W. K., and Shelley, E. G. (1981) Ion streams in the magnetotail, J. Geophys. Res. 86:4639.
27. Kaye, S. M., Johnson, R. G., Sharp, R. D., and Shelley, E. G. (1981a) Observations of transient H^+ and O^+ bursts in the equatorial magnetosphere, J. Geophys. Res. 86:1335.
28. Moore, T. E., Arnoldy, R. L., Feynman, J., and Hardy, D. A. (1981) Propagating substorm injection fronts, J. Geophys. Res. 86:6713.
29. Young, D. T., Balsiger, H., and Geiss, J. (1982) Correlations of magnetospheric ion composition with geomagnetic and solar activity, J. Geophys. Res. 87:9077.
30. Gussenhoven, M. S., Hardy, D. A., and Burke, W. J. (1981) DMSP/F2 electron observations of equatorward auroral boundaries and their relationship to magnetospheric electric fields, J. Geophys. Res. 86:768.
31. Balsiger, H., Eberhardt, P., Geiss, J., and Young, D. T. (1980) Magnetic storm injection of 0.9- to 16- keV/e solar and terrestrial ions into the high-altitude magnetosphere, J. Geophys. Res. 85:1645.

32. Kaye, S.M., Shelley, E.G., Sharp, R.D., and Johnson, R.G. (1981b) Ion composition of zipper events, J. Geophys. Res. 86:3383.
33. Fennell, J.F., Croley, Jr., D.R., and Kaye, S.M. (1981) Low-energy ion pitch-angle distributions in the outer magnetosphere: Ion zipper events, J. Geophys. Res. 86:3375.
34. Olson, W.P., and Pfitzer, K.A. (1974) A quantitative model of the magnetospheric magnetic field, J. Geophys. Res. 79:3739.
35. Reagan, J.B., Nightingale, R.W., Gaines, E.E., Imhof, W.L., and Stassinopoulos, E.G. (1981) Outer zone energetic electron spectral measurements, J. Spacecraft Rockets 18:83-88.
36. Vampola, A.L., Blake, J.B., and Paulikas, G.A. (1977) A New Study of the Outer Zone Electron Environment: A Hazard to CMOS, SAMSO-TR-77-127, 26 pp.
37. Singley, G.W., and Vette, J.I. (1972) The AE-4 Model of the Outer Radiation Zone Electron Environment, NSSDC 72-06.
38. Gaines, E.E., Nightingale, R.W., Imhof, W.L., and Reagan, J.B. (1981) Enhanced radiation doses to high-altitude spacecraft during June 1980, IEEE Trans. Nucl. Sci. NS-28:4502.
39. Garrett, H.B., Schwank, D.C., and DeForest, S.E. (1981a) A statistical analysis of the low-energy geosynchronous plasma environment - I. Electrons, Planet Space Sci. 29:1021.
40. Garrett, H.B., Schwank, D.C., and DeForest, S.E. (1981b) A statistical analysis of the low-energy geosynchronous plasma environment - II. Ions, Planet Space Sci. 29:1045.
41. Mullen, E.G., Gussenhoven, M.S., and Garrett, H.B. (1981) A "Worst Case" Spacecraft Environment as Observed by SCATHA on 24 April 1979, AFGL-TR-81-0231, AD A108680.

Appendix A

SCATHA Experimenters

<u>Instrument</u>	<u>Experimenter</u>	<u>Address</u>
SC1 VLF Wave Analyzer	Dr. H. C. Koons	Aerospace Corp. Space Sciences Lab. P.O. Box 92957 Los Angeles, CA 90009
SC1 Satellite Surface Potential Monitors	Dr. P. F. Mizera	Aerospace Corp. Space Sciences Lab. P.O. Box 92957 Los Angeles, CA 90009
SC2 Particle Detectors	Dr. J. F. Fennell	Aerospace Corp. Space Sciences Lab. P.O. Box 92957 Los Angeles, CA 90009
SC3 High Energy Particle Spectrometer	Dr. J. B. Reagan	Lockheed Missiles & Space Company Dept 5212, Bldg 255 3251 Hanover St. Palo Alto, CA 94304
SC5 Rapid Scan Particle Detector	Dr. D. A. Hardy	AFGL/PHG Hanscom AFB, MA 01731
SC7 Light Ion Mass Spectrometer	Dr. D. D. Reasoner	NASA Marshall Space Flight Center Science Laboratory Huntsville, AL 35812

<u>Instrument</u>	<u>Experimenter</u>	<u>Address</u>
SC8 Energetic Ion Composition Spectrometer	Dr. R. G. Johnson	Lockheed Missiles & Space Company Dept 5212, Bldg 255 3251 Hanover St. Palo Alto, CA 94304
SC9 Charged Particle Detectors	Dr. E. C. Whipple, Jr.	Physics Dept. Univ. of Calif. at San Diego LaJolla, CA 92093
SC10 Electric Field Detector	Dr. T. L. Aggson	NASA/Goddard Space Flight Center Greenbelt, MD 20771
SC11 Magnetometer	Dr. B. G. Ledley	NASA/Goddard Space Flight Center Greenbelt, MD 20771
Transient Pulse Monitor	Dr. R. C. Adamo	SRI 333 Ravenwood Ave. Menlo Park, CA 94025

Appendix B

Correction of SC5 Ion Data Using SC8 Ion Composition Measurements

To avoid possible erroneous interpretation of SC5 ion data due to the nondiscrimination of particle species in the measurements, correction factors derived from the SC8 ion composition data were determined. For the calculations of the correction factors the following assumptions are made: (1) There are only two species abundant enough to be considered, H^+ and O^+ and (2) The efficiency of the SC5 detector is the same for H^+ and O^+ .

In applying the corrections we additionally assume that the results of averaging the SC8 data base can be applied to the results of averaging the SC5 data base. The corrections cannot be applied on a day-to-day basis because there is not a one-to-one correspondence in the two data bases. Furthermore, we will apply a smoothing technique to the SC8 correction factors, so as not to destroy the regularity in the averages of the much larger SC5 data base.

The moments for the ion distribution were first calculated from the SC5 count rates assuming only H^+ (see Section 4.3). From the count rate C_T , which is a function of energy, (E), and pitch angle (Ψ), the distribution functions, $f(E, \Psi)$, are calculated using only the mass of hydrogen (m_p). The functions are constructed from the energy dependent geometric factors as follows:

$$j(E, \Psi) = \frac{C_T(E)}{G(E)} \quad (B1)$$

and

$$f(E, \Psi) = \frac{m_p^2}{2E} \cdot \frac{C_T(E)}{G(E)} \quad . \quad (B2)$$

The four moments of the distribution function are calculated for each full spin of the satellite by summing over the energy steps of the detector and the pitch angle intervals. (For details of these calculations see Section 4.3.) Thus,

$$n_{SC5} = \frac{(m_p)^{1/2}}{\sqrt{2}} \sum \frac{C_T(E, \alpha) \Delta E \Delta \Psi}{E^{1/2} G(E)} \quad (B3)$$

$$NF_{SC5} = \frac{1}{4\pi} \sum \frac{C_T(E, \alpha) \Delta E \Delta \Psi}{G(E)} \quad (B4)$$

$$\epsilon_{SC5} = \frac{(m_p)^{1/2}}{\sqrt{2}} \sum \frac{C_T(E, \alpha) E^{1/2} \Delta E \Delta \Psi}{G(E)} \quad (B5)$$

$$EF_{SC5} = \frac{1}{4\pi} \sum \frac{C_T(E, \alpha) \Delta E \Delta \Psi}{G(E)} \quad . \quad (B6)$$

Here n , NF , ϵ , EF are the number density, number flux, energy density, and energy flux, respectively. From Eqs. (B4) through (B6) it is clear that the mass of the ion enters only into the equations for the number density and the energy density.

If it were possible to distinguish between the counts due to O^+ (C_O) and those due to H^+ (C_H), separate calculations of the contributions to the number and energy density could be made using the appropriate masses m_O and m_p . For example,

$$n_{O, H} = \frac{(m_{O, H})^{1/2}}{\sqrt{2}} \sum \frac{C_{O, H}(E, \alpha) \Delta E \Delta \Psi}{E^{1/2} G(E)} \quad . \quad (B7)$$

In Eq. (B7) we implicitly use the second assumption. If we also assume that the total count rate C_T is comprised only of C_O and C_H , we have

$$C_T = C_O + C_H \quad . \quad (B8)$$

Similarly, the total ion number density and energy density will be the sum of the O^+ and H^+ densities

$$n_I = n_O + n_H \quad , \quad (B9)$$

and

$$\epsilon_I = \epsilon_O + \epsilon_H \quad . \quad (B10)$$

Since we may write $C_H = C_T - C_O$, the actual hydrogen density can be determined from C_T and C_O by:

$$\begin{aligned} n_H &= \frac{(m_p)^{1/2}}{\sqrt{2}} \sum \frac{C_T \Delta E \Delta \Psi}{E^{1/2} G(E)} - \frac{(m_p)^{1/2}}{\sqrt{2}} \sum \frac{C_O \Delta E \Delta \Psi}{E^{1/2} G(E)} \\ &= n_{SC5} - \frac{(m_p)^{1/2}}{\sqrt{2}} \sum \frac{C_O \Delta E \Delta \Psi}{E^{1/2} G(E)} \quad . \end{aligned} \quad (B11)$$

Combining Eqs. (B7), (B9), and (B11), we have

$$n_I = n_{SC5} + \frac{m_O^{1/2} - m_p^{1/2}}{m_O^{1/2}} \cdot n_O \quad . \quad (B12)$$

Since n_O is a fraction of n_I , we can write $n_O = a n_I$. It is then a simple matter to show that

$$n_I = \frac{n_{SC5}}{1 - a \left(\frac{m_p^{1/2}}{m_O^{1/2}} \right)} \quad . \quad (B13)$$

If instead we use the O^+/H^+ density ratio (b) that equals $a/(1 - a)$ and take $(m_O/m_p)^{1/2} = 4$, we get

$$n_I = \frac{4(1 + b)}{4 + b} \quad . \quad (B14)$$

The correction factor (δ) is then defined as

$$\delta = \frac{4 \left(1 + \frac{n_O}{n_H} \right)}{4 + \frac{n_O}{n_H}} . \quad (B15)$$

The same correction factor applies to n and ϵ . There are no correction factors for NF and EF.

Table B1 gives the correction factors in the following bins: L-shell 5-6, 6-7, 7-8, 8-8.5 R_E ; KP 0, 1; 2, 3; 4, 5; ≥ 6 -; and 3-hr LT bins. These correction factors are calculated directly from the O^+/H^+ density ratios given in Table 26, and using Eq. (B15). They apply for the energy range of the SC8 detector; 0.1 to 32 keV. The correction factors are to be applied to the statistical averages of the spin-integrated moments obtained from the SC5 detector. In order not to heavily bias the SC5 data set with possible spurious points from the SC8 data set, we have produced a more smoothly varying set of correction factors by interpolating through missing points, and averaging two LT bins together. This produces, a noon, dusk, midnight, and dawn correction factor for each L-shell and KP bin. Only two significant figures are retained in the correction factors. Since in most cases the averages were rounded down, the factors and their variations are on the conservative side. The three major variations discussed in presenting the SC8 data have been retained, perhaps even enhanced. They are (1) an increase of δ with increasing activity, (2) a decrease of δ in the midnight (and dusk) sector with decreasing L, and (3) an increase of δ in the dayside. (The variation of δ with L in the dayside is unclear.) Table B2 gives the modified correction factors.

The LT hourly averages of the SC5 low energy (0.05 to 20 keV) ion number densities and energy densities were multiplied by the modified correction factor (δ), to give the corrected number and energy densities. For comparison to the SC8 total number density, $n(H^+) + n(O^+)$, measured over the energy range 0.1 to 32 keV, the corrected SC5 averages were further averaged (by bin) over the corresponding 3-h LT bins of the SC8 averaged data base. Figure B1 is a scatter plot of the corrected SC5 data vs the SC8 data. Different symbols are used for the various KP bins. The scatter increases with increasing density (and, correspondingly, increasing KP). The very large scatter in points with $KP \geq 6$ results from biases in the limited statistical sample for this activity level. There is no apparent aliasing of one data set higher or lower than the other. On the whole the data sets agree within a factor of two. (If the $KP \geq 6$ points are excluded, the agreement is much better.) Linear regressions run for the whole

Table B1. Unsmoothed Correction Factors (δ)

KP 0, 1	LT	L-shell (R_E)			
		5-6	6-7	7-8	8-9
KP 0, 1	00-03	--	1.84	1.18	1.06
	03-06	1.47	1.29	1.16	1.09
	06-09	1.38	1.24	1.15	1.10
	09-12	1.40	1.49	1.42	--
	12-15	1.43	1.61	--	--
	15-18	1.81	1.42	1.31	--
	18-21	1.71	1.37	1.13	1.12
	21-24	2.30	1.28	1.11	1.07
KP 2, 3	00-03	--	1.30	1.19	1.09
	03-06	1.32	1.16	1.22	1.27
	06-09	1.36	1.30	1.38	1.57
	09-12	1.39	1.55	1.60	--
	12-15	1.58	1.76	1.95	--
	15-18	1.52	1.29	1.24	--
	18-21	1.49	1.29	1.16	1.12
	21-24	1.32	1.25	1.18	1.08
KP 4, 5	00-03	1.66	1.44	1.40	1.23
	03-06	1.40	1.40	1.50	1.47
	06-09	1.42	1.46	1.56	--
	09-12	1.32	1.63	1.32	--
	12-15	1.92	1.52	1.47	--
	15-18	1.82	1.32	1.31	--
	18-21	1.74	1.29	1.22	1.58
	21-24	1.58	1.63	1.18	1.15
KP ≥ 6 -	00-03	--	1.89	1.68	1.20
	03-06	2.22	2.10	1.61	1.95
	06-09	1.88	2.21	1.61	--
	09-12	2.19	2.13	--	--
	12-15	2.39	2.33	--	--
	15-18	1.33	2.38	1.39	--
	18-21	1.95	1.89	2.05	1.52
	21-24	--	1.82	2.01	1.35

Table B2. Modified Correction Factors (δ)

KP 0, 1	LT	L-shell (R_E)			
		5-6	6-7	7-8	8-9
KP 0, 1	21-03	2.0	1.5	1.2	1.1
	03-09	1.5	1.3	1.2	1.1
	09-15	1.4	1.6	1.4	1.1
	15-21	1.7	1.4	1.2	1.1
KP 2, 3	21-03	1.3	1.3	1.2	1.1
	03-09	1.3	1.3	1.3	1.4
	09-15	1.5	1.7	1.8	-
	15-21	1.5	1.3	1.2	1.1
KP 4, 5	21-03	1.6	1.5	1.3	1.2
	03-09	1.4	1.4	1.5	1.5
	09-15	1.6	1.5	1.4	-
	15-21	1.7	1.3	1.2	1.5
KP ≥ 6 -	21-03	2.0	1.8	1.8	1.3
	03-09	2.1	2.1	1.6	1.8
	09-15	2.3	2.2	1.7	-
	15-21	1.6	2.1	1.7	1.4

data set (solid line), and for KP 0-5+ (dashed line) fits are also shown in Figure B1. The correlation coefficients of the data sets went from 0.73 for KP 0-5+, to 0.68 for all KPs.

The effects of applying the correction factors to the SC5 data and a comparison to the SC8 data are shown in Figure B2 in a LT, L-shell format for the data base bins KP 2,3. This KP-range level was chosen because it contained one of the largest data bases. The scale used for the density is in rather crude steps of 0.5 cm^{-3} . Figure B2(a) is the low energy SC5 ion density assuming the composition to be purely H^+ . Increased density from plasma sheet injections is evident from 2300 to 0600 LT. Figure B2(b) shows the SC5 ion density after the correction for O^+ is made. Perhaps the most obvious effect is the dayside enhancement of the density, which does not appear in the uncorrected density. There is also more structure and spatial extent in the nightside enhancements. The SC8 total ion density is shown in Figure B2(c). A comparison of the corrected SC5 ion density to the SC8 ion density shows the SC5 densities to be more smoothly varying than the SC8 densities, which is to be expected from the relative number of samples in the two data bases. The corrections clearly show that O^+ must be carefully considered when interpreting ion data near-geosynchronous altitudes.

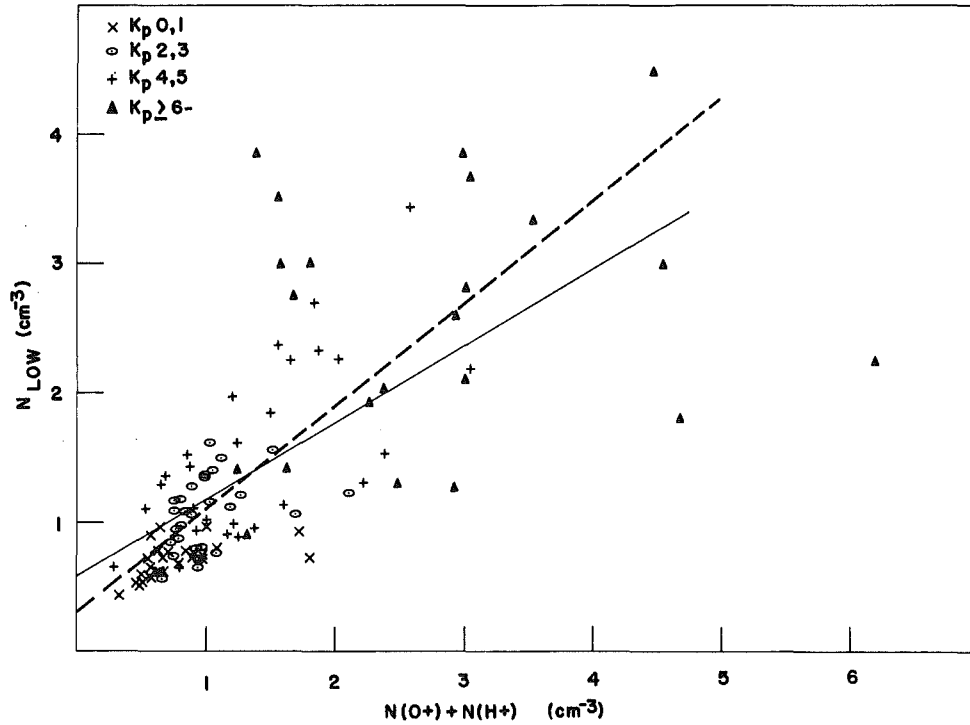


Figure B1. Three-hour LT Averages of the Corrected SC5 Low-Energy (0.05-20 keV) Ion Density vs the Sum of the SC8 O⁺ Plus H⁺ Densities. The symbols vary according to KP level. The lines are the linear fits to the data with (solid line) and without (dashed line) the $KP \geq 6$ - data

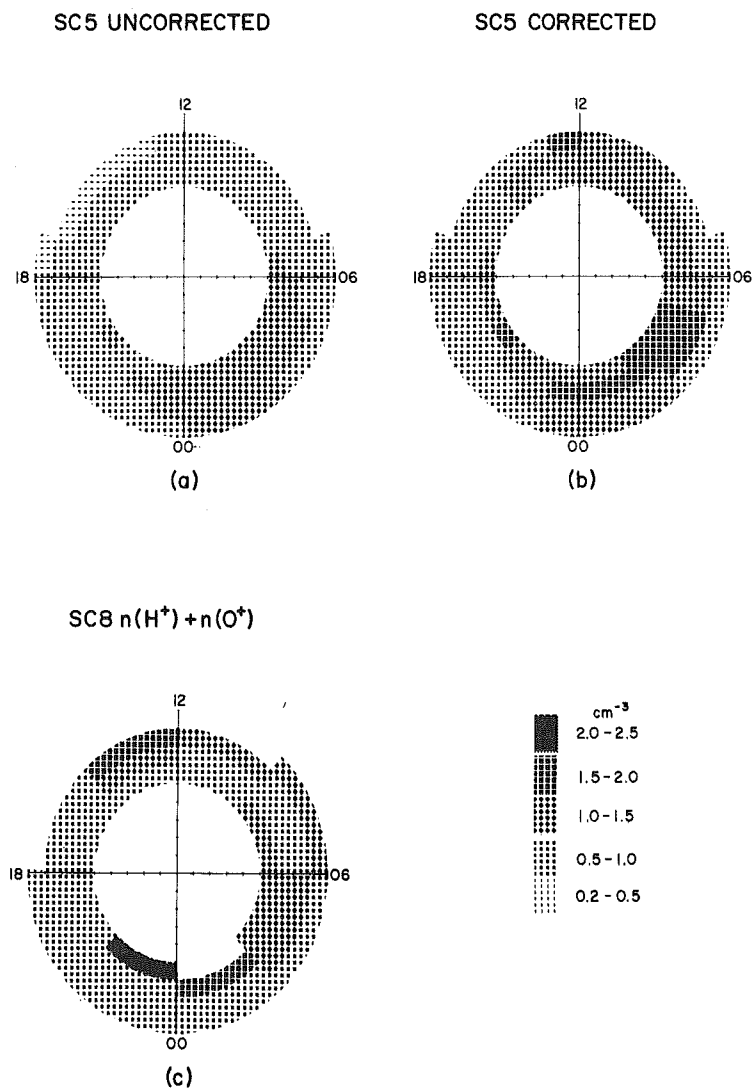


Figure B2. Polar Plots of Ion Number Densities in LT and L-shell for KP Levels $\geq 2-$ and $\leq 3+$. (a) SC5 ion densities assuming 100 percent H^+ , (b) SC5 ion densities corrected by SC8 O^+/H^+ density ratios, and (c) SC8 total ion density

Appendix C

The 40-keV Electron Durable Trapping Region

J. Feynman
Dept. of Physics
Boston College
Chestnut Hill, MA 02176

[This appendix was condensed from an as yet unpublished manuscript of the same title.]

The position of the near-geosynchronous region of durable trapping of 40-keV electrons on the nightside is found for varying magnetic activity levels using SC5 electron particle counts from the SCATHA satellite. The high-latitude boundaries of the 40-keV trapping region at geosynchronous has previously been observed by studying sudden appearances and disappearances of electrons and ions with energies greater than approximately 50 keV (Lezniak and Winckler,^{C1} Bogott and Mozer,^{C2} and Walker et al^{C3}). However, to date no study has been reported that describes the position in the magnetosphere where the boundary is likely to be

-
- C1. Lezniak, T.W., and Winckler, J.R. (1970) Experimental study of magnetospheric motions and the acceleration of energetic electrons during substorms, J. Geophys. Res. 75:7075.
- C2. Bogott, F.H., and Mozer, F.S. (1973) Nightside energetic particle decreases at the synchronous orbit, J. Geophys. Res. 78:8119.
- C3. Walker, R.J., Erickson, K.N., Swanson, R.L., and Winckler, J.R. (1976) Substorm-associated particle boundary motion at synchronous orbit, J. Geophys. Res. 81:5541.

found. Because of the extended range of coverage of the SCATHA satellite, we can examine the position of the 40-keV electron trapping region as a function of both magnetic activity and radial distance from the earth. Here we examine the trapping region and define a coordinate system that can be used to order the boundaries as measured by the SC5 data set.

Near geosynchronous orbit sudden disappearances of ion and electron fluxes are called dropout events. Bogott and Mozer^{C2} explained the disappearances as being due to a satellite exiting the region of high energy trapped particles because of the reconfiguration of the magnetic field toward a more taillike field during sub-storm buildup. The subsequent reappearance of the plasma is then due to the relaxation of the nightside magnetosphere during the expansion phase of substorms. The relative importance of geomagnetic activity level and of satellite position in predicting dropouts near geosynchronous orbit using SCATHA data has been discussed by Feynman et al.^{C4} Here we extend the results of that report by examining a larger data base and ordering the data set better.

Dropouts and returns of particle fluxes near perpendicular to the magnetic field due to satellite passage through the high-latitude trapping region are characterized from the SC5 count rate data by near simultaneous gradients in both ions and electrons. Figure C1 gives three examples of dropouts. The count rates for ~100-keV electrons and ~125-keV ions are shown as a function of UT and LT for three intervals. The top panel shows a dropout near 2245 LT on day 87, 1979. A second smaller dropout occurred near 0320 LT, which recovered near 0400 LT. The center panel shows the typically quiet-time featureless behavior of the nightside particles at the same energy levels for day 212, 1979. The bottom panel gives an example from day 198, 1979 when both the flux decrease and increase were rapid. The count rates of lower energy particles (<10 keV) may not change at all over the same period.

All SC5 data taken between day 75, 1979 and day 74, 1980 were used in the statistical study to follow. Only 13 days of data were missing from the entire year. Dropouts were initially determined by scanning the ~100-keV electron count rates for decreases and/or increases of over an order of magnitude in count rate. The event was then identified as a dropout if the increase or decrease occurred at the same time for all higher electron energies and for all ion high energies, and if the count rate in the ~40-keV electron channel was ten counts or less. Dropouts as defined by this criteria occurred on 103 days.

C4. Feynman, J., Saflekos, N.A., Garrett, H.B., Hardy, D.A., and Mullen, E.G. (1981) Disappearance and reappearance of particles of energies >50 keV as seen by P78-2 (SCATHA) at near geosynchronous orbit, in Spacecraft Charging Technology 1980, NASA Conference Publication 2182, AFGL-TR-81-0270, AD A114426, p. 755.

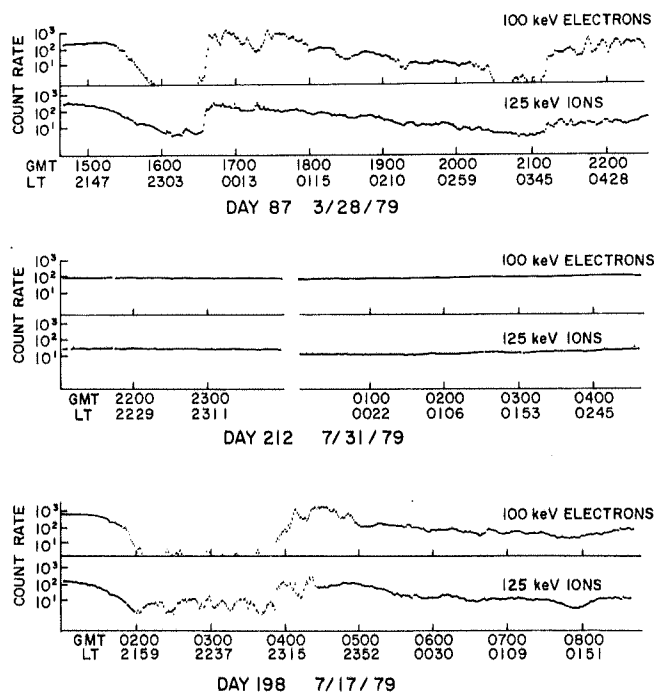


Figure C1. Examples of Dropouts in the SC5 Electron and Ion Particle Counts. The top and bottom plots show dropouts, and the middle plots show a quiet day for comparison

In order to study the position dependence of dropouts independent from geomagnetic activity level, the two effects had to first be separated. Figures C2 and C3 show the positions at which dropouts were seen to occur for KP ranges $\leq 4+$ and $\geq 5-$, respectively. Dropout periods are indicated by solid lines. The top panel in each figure shows where the dropouts occurred in R_E as a function of local time. With one exception all the dropouts occurred between 1700 and 0700 LT. In general, dropouts were rare for distances $< 6 R_E$ and became quite common beyond $7 R_E$. Although it is not evident in these figures, dropouts occur at lower R_E s during magnetically disturbed periods. The bottom two panels were attempts to order the data in solar magnetic (SM) and geocentric solar magnetospheric (GSM) coordinate systems, neither of which worked too well.

Since SM coordinates better order data in the inner magnetosphere and GSM coordinates better order data in the geomagnetic tail, it was felt that a combination of the two systems might better order data in the near-geosynchronous regime that is strongly influenced by both the Earth's main field and the direction into which the tail is swept by the the solar wind. The difference between SM and GSM

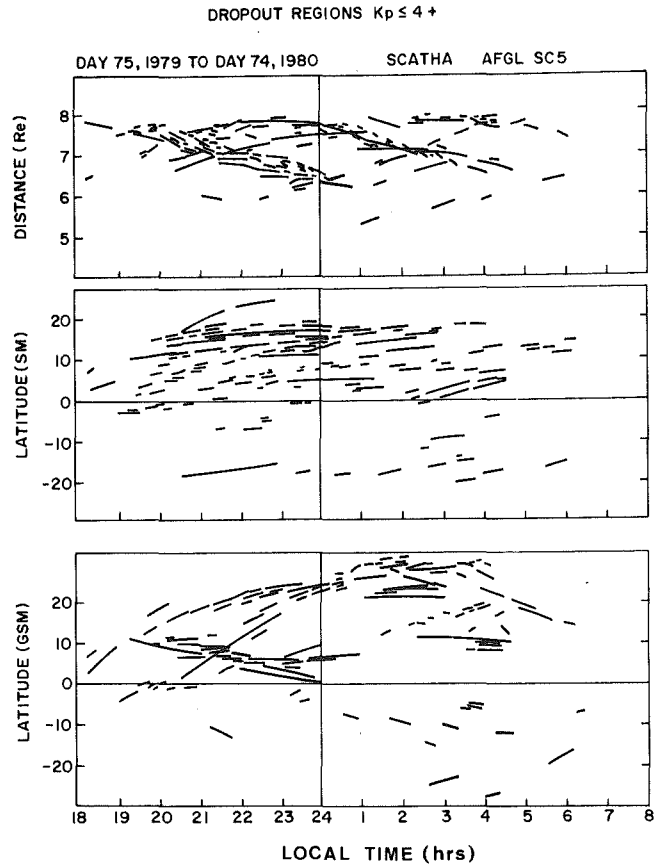


Figure C2. Positions of Dropouts of 40-keV Electron Fluxes in Radial Distance, R_E (Top Plot), Solar Magnetic Latitude (Middle Plot), and Geocentric Solar Magnetospheric Latitude (Bottom Plot) vs LT for Periods Between Day 75, 1979 and Day 74, 1980 When the K_p Level was $\leq 4+$

coordinates is in the definition of the direction of the z-axis. In SM coordinates the z-axis is parallel to the direction of the Earth's magnetic pole, and in GSM coordinates the z-axis is in a plane perpendicular to the Earth-sun line. Fortunately the two systems differ only by a rotation about their y-axis. From this we can define a new coordinate system to be called composite coordinates (CC), which differ from GSM and SM only in that the angle of rotation about the y-axis in the transformation is less than that required to go from one of the standard systems to the other. For this study the rotation used was half that between the two standard systems, thus putting equal importance on the earth's field and solar wind effects on the tail field. In this system there is no change in either LT or R_E .

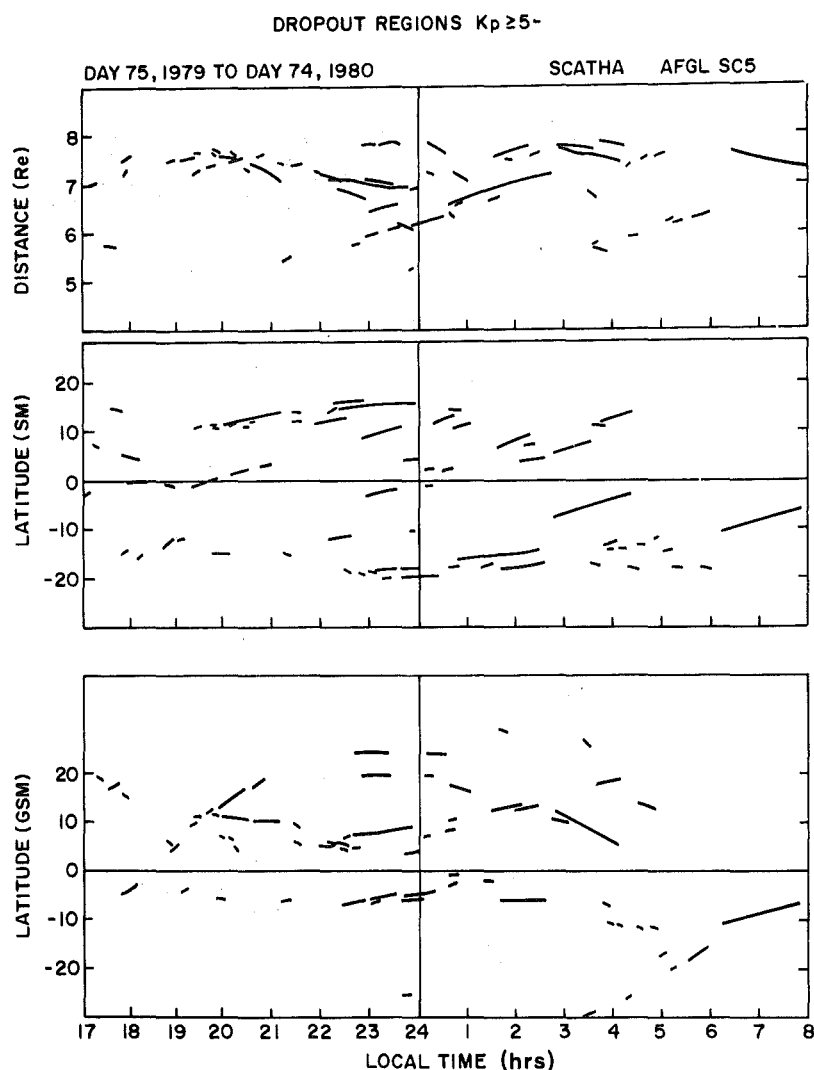


Figure C3. Positions of Dropouts of 40-keV Electron Fluxes in Radial Distance, R_E (Top Plot), Solar Magnetic Latitude (Middle Plot), and Geocentric Solar Magnetospheric Latitude (Bottom Plot) vs LT for Periods Between Day 75, 1979 and Day 74, 1980 When the K_p Level was ≥ 5 -

Figure C4 gives the positions of the dropouts during the highest levels of geomagnetic activity ($K_p \geq 6$ -). Data on 38 dropouts from 14 days when K_p was ≥ 6 - are plotted. The top panel gives the position of the dropouts in composite coordinate magnetic latitude vs LT in hours. The two dropouts in the morning sector later than 0600 UT were from periods of sparse data and are somewhat suspect. The dropouts commonly occur near 10° magnetic latitude, but can occur at lower

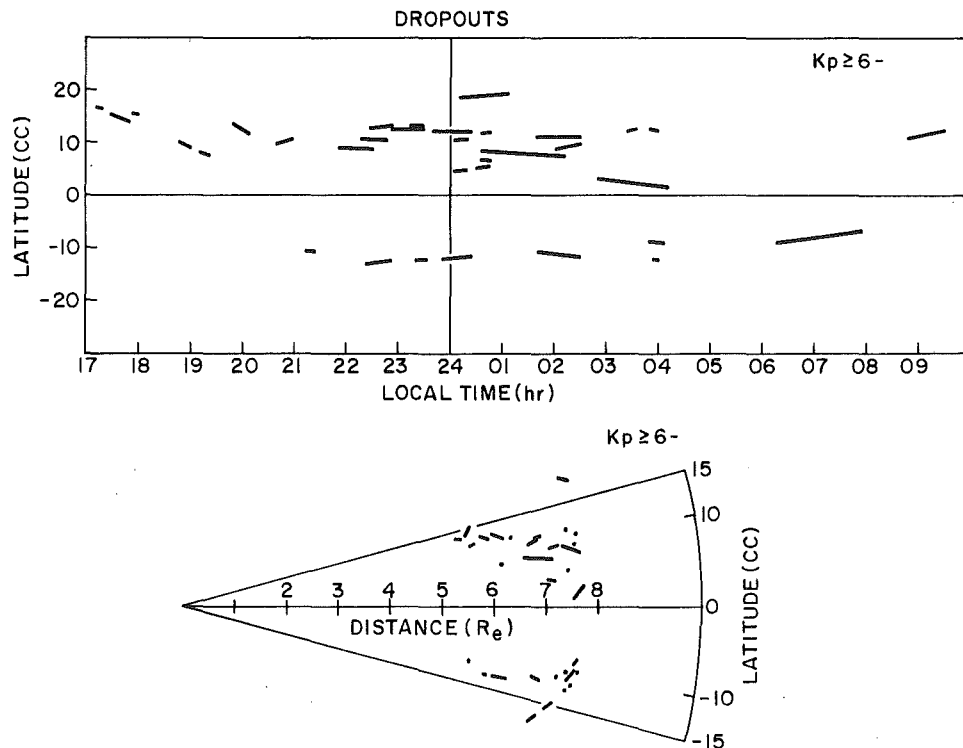


Figure C4. The Top Plot Shows the LT of Dropouts in Composite Coordinate Latitude During Magnetic Storm Periods When $KP \geq 6-$. The bottom plot shows the same dropouts as a function of radial distance and composite coordinate latitude

latitudes. It is only when the dropouts are plotted in CC latitude vs R_E as in the bottom panel of Figure C4 that a clear pattern emerges. Here a region from which dropouts are excluded is apparent. It is centered on the equatorial plane, is about 10° in half-width at $6 R_E$ and becomes thinner with increasing distance from the earth. Starting at an R_E of about 7, dropouts can be seen near any magnetic latitude in CC sampled by SCATHA for this highest activity level. For KP levels $\leq 4+$ dropouts were not normally seen to occur within $\pm 10^\circ$ latitude of the equator in composite coordinates. These data are in agreement with the concept of the trapping region thinning and moving Earthward during periods of high magnetic activity.

Since the actual magnetosphere is never static, a description of the position and extent of the idealized trapping region can not be derived from the SCATHA observations. However, since an idealized trapping region is almost never observed, the trapping region as measured by SC5 for the SCATHA order has been

described. In summary, it was found that a composite coordinate magnetic field system was needed to order the dropout data. In this composite coordinate system there was a region of the magnetosphere for KP levels $\leq 4+$ inside of which 40-keV electron fluxes were almost always seen. The region centered on 0° latitude in CC and was about 10° or $1.2 R_E$ wide and extended over the entire radial distance sampled by SCATHA. Outside this region 40-keV electrons were sometimes absent and sometimes present. Dropout locations for KP levels $\geq 6-$ (which identify periods of magnetic storms) were found to decrease in magnetic latitude (CC) with an increase in R_E up to $\sim 7 R_E$ beyond which they could be found near any magnetic latitude sampled.

Appendix D

High-level Spacecraft Charging Environments

Mullen and Gussenhoven^{D1} have identified and characterized the environments and locations near geosynchronous orbit where high-level spacecraft frame charging takes place. Although we do not desire to reproduce that study here, we do wish to include the major results, since they provide a measured upper limit of certain data parameters discussed in the atlas. Spacecraft charging in this appendix refers only to plasma-to-vehicle frame potential difference (ϕ_f) unless otherwise specifically stated.

Three periods of sunlight charging when the ϕ_f exceeded -300 V were used in the study. The SCATHA time and position for the three periods are given in Table D1. Sunlight charging in excess of -300 V would equate to several kilovolts in eclipse.

We have found that at times of substantial sunlight charging (>100 V) the SCATHA satellite encounters high fluxes of electrons with energies greater than 20 keV, in the absence of a cold ion population. Although good measurements of the high energy plasma characteristics are obtained on SCATHA, a detailed understanding of how current balance is achieved is hampered by lack of: (1) measurement of the cold plasma population, (2) high resolution measurements of particles along the magnetic field, (3) an understanding of the extent to which the cold

D1. Mullen, E.G., and Gussenhoven, M.S. (1982) High Level Spacecraft Charging Environments Near Geosynchronous Orbit, AFGL-TR-82-0063, AA A118791.

Table D1. SCATHA Time and Position for "Worst Case" Charging Events

Day (1979)	Peak Sunlight Charging Level	LT	L-shell	KP	R _E	MLT
114	-340 V	2314	7.1	3+	6.6	2311
241	-740 V	0428	5.8	7-	5.7	0435
363	-580 V	2243	5.7	5	5.4	2230

population is trapped in the vicinity of the satellite and possibly reflected back to the satellite, and (4) the dependence of backscattered and secondary electrons on the primary spectrum.

The contribution that can be made from the particle measurements on SCATHA is the specification of the distribution of the high energy population during charging. In this appendix the actual distribution functions for peak levels of charging on days 114, 241, and 363 are presented. A method of fitting the distributions is determined that best maintains the essential characteristics of the high energy plasma during charging.

Figures D1a, D1b, and D1c show electron distributions from days 114, 241, and 363, respectively. The distribution functions are for measurements made perpendicular to the magnetic field. We use these distribution functions with the assumption of isotropy to represent the plasma. A measure of the anisotropy of the plasma can be taken from Figures 18 through 20 of Mullen and Gussenhoven.^{D1} Using the perpendicular distribution function with the assumption of isotropy will normally lead to an overestimation of plasma parameters for charging periods. However the assumption of isotropy is a particularly good one for day 241. In Figures D1a through D1c the distributions shown by dashed lines are from the nearest precharging period available. The following observations can be made concerning the distributions. First, the three sets of distribution functions are remarkably similar. The precharging distributions for both ions and electrons have a distinct "knee" at ~10 keV for electrons and ~100 keV for ions. On either side of the knee the variation of the distribution with energy behaves as a power law (linear on a log-log plot). Second, the peak charging distributions vary from the precharging distributions in the same way on all three days, with an increase on the high side of the knee and a depletion on the low side. And, third, the lowest energy channels (less than the satellite potential) do not show consistent variations. On day 114 the ion fluxes less than 1 keV were below detectability precharging,

and showed no enhancement during charging. On day 363 the same precharging ion flux levels fell below detectability during charging. On day 241 the satellite potential apparently enhances the low energy ion flux to the vehicle. The lowest-energy electron fluxes are depressed on two of the days during charging, 241 and 363, and unaffected on the third, 114. These different low-energy particle behaviors indicate either variations in the low energy ambient plasma, or various forms of low energy access to the satellite perpendicular to the magnetic field, or a combination of the two.

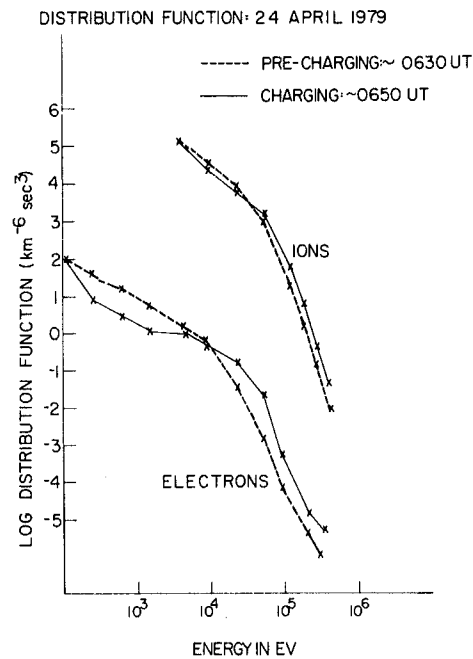


Figure D1a. Distribution Functions of Ions and Electrons Measured Perpendicular to the Magnetic Field Prior to Charging (Dashed Line) and During the Peak Charging Levels (Solid Lines) on Day 114, 1979

DISTRIBUTION FUNCTION: 29 AUGUST 1979 (241)

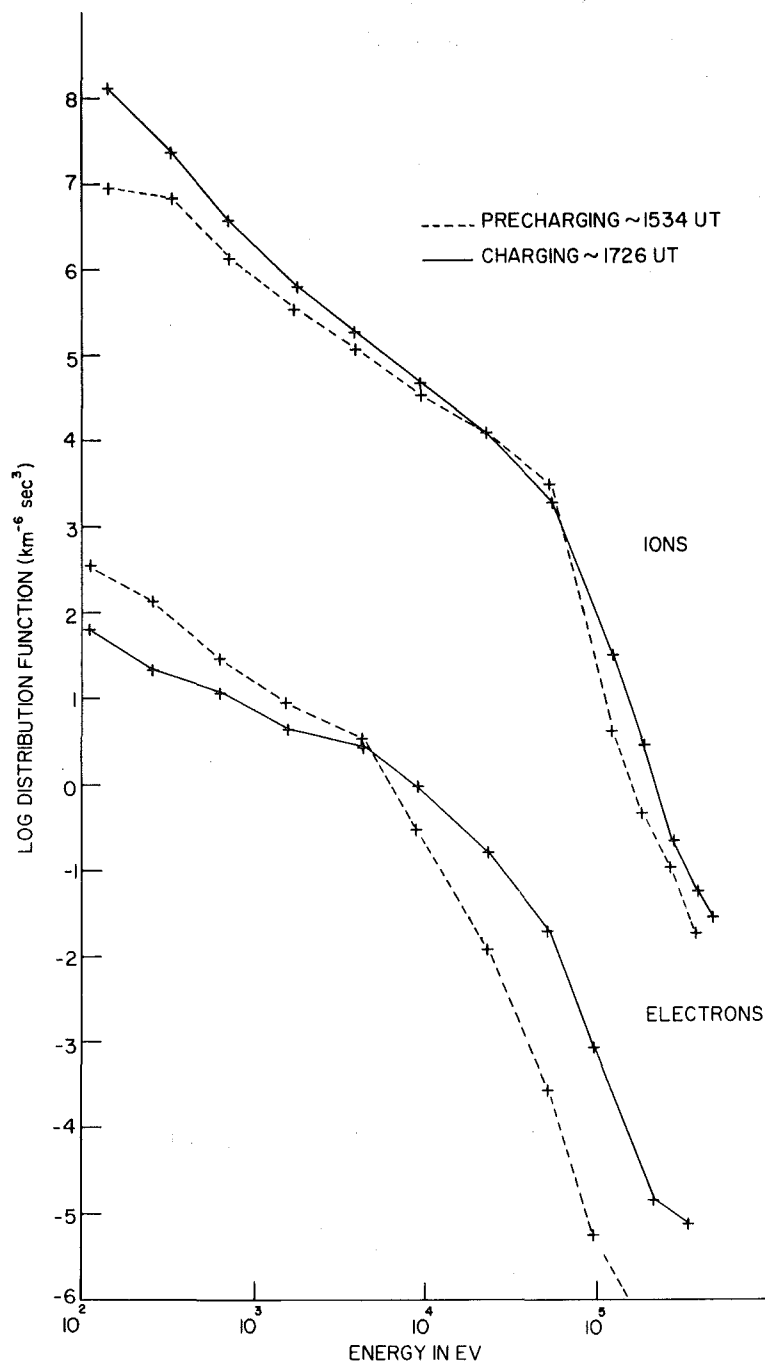


Figure D1b. Distribution Functions of Ions and Electrons Measured Perpendicular to the Magnetic Field Prior to Charging (Dashed Line) and During the Peak Charging Levels (Solid Lines) on Day 241, 1979

DISTRIBUTION FUNCTION 29 DECEMBER 1979 (363)

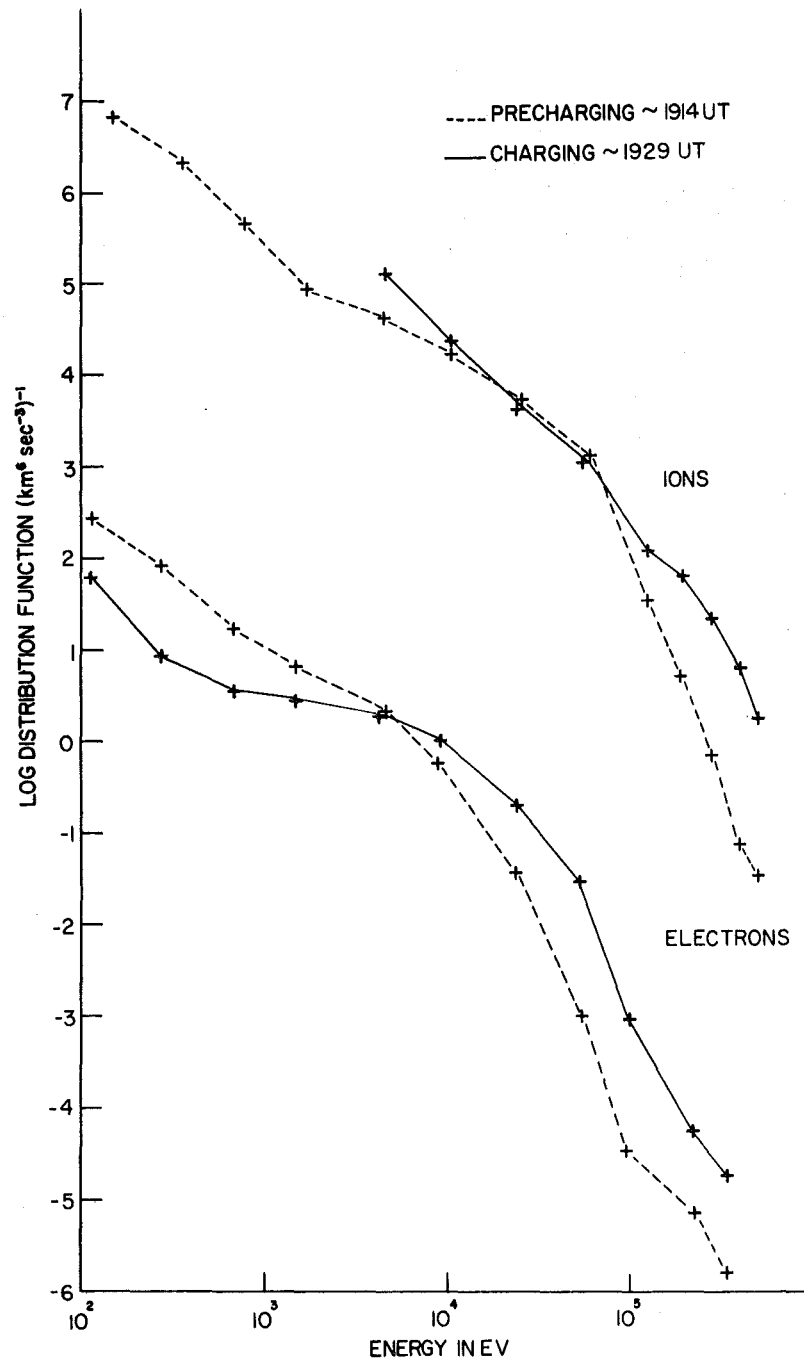


Figure D1c. Distribution Functions of Ions and Electrons Measured Perpendicular to the Magnetic Field Prior to Charging (Dashed Line) and During the Peak Charging Levels (Solid Lines) on Day 363, 1979

Results of the statistical study and the "worst case" studies are summarized:

(1) In the near-geosynchronous region of space, significant levels of space-craft charging can occur

- (a) between 1900 and 0900 LT,
- (b) at any distance between $R_E = 5.3$ and 7.8 ,
- (c) at any magnetic latitude between $\pm 19^\circ$,
- (d) at any L-shell value between 5.5 and 8.6 , and
- (e) for any period the magnetic activity index K_p is $2+$ or greater.

Charging can extend outside this region anywhere electron fluxes at energies between ~ 30 and 70 keV exceed 6×10^2 elec/cm²-sec-sr-eV in a plasma-sheet-type low-energy particle environment.

(2) A "worst case" environment can best be described by the first four moments of the distribution function both over the total population from 0 to 400 keV and over the range from 20 to 400 keV, where charge level is determined. The set of "worst case" moments integrated over pitch angle are:

- (a) total-number density: ions 3.0 ,
electrons 3.0 cm^{-3} ,
- (b) high-number density: ions 0.8 ,
electrons 0.6 cm^{-3} ,
- (c) total-number flux: ions 4×10^8 ,
electrons $1.3 \times 10^{10} \text{ cm}^{-2} \text{ s}^{-1}$,
- (d) high-number flux: ions 2×10^8 ,
electrons $4.9 \times 10^9 \text{ cm}^{-2} \text{ s}^{-1}$,
- (e) total-energy density: ions 3.7×10^4 ,
electrons $2.4 \times 10^4 \text{ eV cm}^{-3}$,
- (f) high-energy density: ions 2.8×10^4 ,
electrons $1.4 \times 10^4 \text{ eV cm}^{-3}$,
- (g) total-energy flux: ions 9.4×10^{12} ,
electrons $1.9 \times 10^{14} \text{ eV cm}^{-2} \text{ s}^{-1}$,
- (h) high-energy flux: ions 8.3×10^{12} ,
electrons $1.5 \times 10^{14} \text{ eV cm}^{-2} \text{ s}^{-1}$.

The total densities for ions and electrons are balanced in a way to maximize charging. High refers to the 20 to 400 -keV range.

(3) If two-Maxwellian fit parameters are required, the following fits will give a maximum realistic charging spectrum parallel and perpendicular to the magnetic field

- (a) $n_1 \parallel$: ions 1.1 electrons 1.0 cm^{-3} ,
- (b) $n_2 \parallel$: ions 1.7 electrons 1.4 cm^{-3} ,
- (c) $T_1 \parallel$: ions 0.4 electrons 0.6 keV ,
- (d) $T_2 \parallel$: ions 24.7 electrons 25.1 keV ,

- (e) $n_{1\perp}$: ions 0.9 electrons 0.8 cm^{-3} ,
- (f) $n_{2\perp}$: ions 1.6 electrons 1.9 cm^{-3} ,
- (g) $T_{1\perp}$: ions 0.3 electrons 0.6 keV,
- (h) $T_{2\perp}$: ions 25.6 electrons 26.1 keV.

These spectra are quite isotropic although times of large anisotropies were seen during charging. If desired, more anisotropy can be simulated by decreasing the parallel density components.